






Chemical Abundances of the Bioessential Elements C, O and S, and the Refractory Elements Fe and Ni, in Solar-type Exoplanet-hosting Stars from HARPS North and South

ELLEN COSTA-ALMEIDA ¹, LUAN GHEZZI ^{2,1}, KATIA CUNHA ^{3,1}, VERNE V. SMITH ⁴ AND
JONATHAN J. FORTNEY ⁵

¹*Observatório Nacional, Rua General José Cristino, 77, 20921-400 São Cristóvão, Rio de Janeiro, RJ, Brazil*

²*Universidade Federal do Rio de Janeiro, Observatório do Valongo, Ladeira do Pedro Antônio, 43, Rio de Janeiro, RJ 20080-090, Brazil*

³*Steward Observatory, University of Arizona, 933 North Cherry Avenue, Tucson, AZ 85721, USA*

⁴*Noirlab, 950 North Cherry Avenue, Tucson, AZ 85721, USA*

⁵*Department of Astronomy and Astrophysics, University of California, Santa Cruz, CA 95064, USA*

ABSTRACT

We determined atmospheric and evolutionary parameters, along with chemical abundances of C, O, S, Fe, and Ni for 290 solar-type exoplanet hosting stars using high-resolution HARPS-North and HARPS-South spectra, and radii for 373 exoplanets using literature transit depths. We find that stars hosting giant exoplanets ($R_{\text{pl}} > 4 R_{\oplus}$) show enhanced $[X/H]$ abundances compared to small exoplanet hosts for all elements analyzed. When considering only exoplanets with $P_{\text{orb}} \leq 30$ days, there is a statistically significant anti-correlation between host star $[\text{Fe}/\text{H}]$ and P_{orb} . However, $[\text{Fe}/\text{H}]$ does not continue to decline as the orbital period increases, but rather rises again for exoplanets with larger orbital periods. Stars hosting only small exoplanets or hosting at least one sub-Saturn show significant differences between the populations of hot and warm exoplanets for all elements. In contrast, stars hosting at least one Jupiter-sized planet show no abundance differences. The host star C/O ratios obtained vary from 0.17 to 0.95, with giant exoplanet hosts exhibiting the lowest median C/O ratios ($0.43_{-0.03}^{+0.02}$), while the 3 – 4 R_{\oplus} sub-Neptune hosts in our sample exhibit the highest median C/O ratios ($0.55_{-0.01}^{+0.05}$). Our sample has 199 exoplanets with estimated masses and we find correlations between host star $[\text{O}/\text{H}]$ and $[\text{S}/\text{H}]$ and $\log(M_{\text{pl}}/M_{\oplus})$. When segregating the sample into hot and warm exoplanet hosts, these trends are only found for warm exoplanets. Dividing the sample between low- (91 exoplanets) and high- $[\alpha/\text{Fe}]$ (20 exoplanets) stars, there are trends between host star $[\text{O}/\text{H}]$, $[\text{S}/\text{H}]$, $[\text{Fe}/\text{H}]$ and $[\text{Ni}/\text{H}]$ and $\log(M_{\text{pl}}/M_{\oplus})$ only for the low- $[\alpha/\text{Fe}]$ sample.

Keywords: Fundamental parameters of stars (555); Stellar abundances (1577); Spectroscopy (1558); Exoplanets (498)

1. INTRODUCTION

Since the discovery of 51 Pegasi b, the first exoplanet orbiting a Sun-like star (Mayor & Queloz 1995), significant progress has been made through a variety of techniques and instruments used to detect exoplanets. Consequently, we have now surpassed the milestone of 6000 detected exoplanets (NASA Exoplanet Archive¹). These discoveries, along with the associated detailed characterizations of both exoplanets and their host stars, have enabled more comprehensive investigations into planetary formation, evolution, and habitability.

Initially suggested by Gonzalez (1997) and Santos et al. (2000) and further investigated by, e.g., Fischer & Valenti (2005), the planet-metallicity² correlation has revealed that the presence of short-period giant exoplanets is favored around metal-rich stars (e.g., Mortier et al. 2013; Ghezzi et al. 2018). This correlation, to this day, remains the

Corresponding author: Ellen Costa-Almeida
ellenalmeida@on.br

¹ <https://exoplanetarchive.ipac.caltech.edu/>

² Metallicity ($[\text{Fe}/\text{H}]$) is commonly used as a general indicator of the overall abundance of metals in the star though it is based on the iron abundance. $[\text{Fe}/\text{H}] = \log_{10}(N_{\text{Fe}}/N_{\text{H}})_{\star} - \log_{10}(N_{\text{Fe}}/N_{\text{H}})_{\odot}$.

strongest connection between exoplanets and their host stars, directly impacting our view on planet formation by providing support for the core accretion mechanism (e.g., Pollack et al. 1996; Ida & Lin 2004). However, it is still unknown to what extent this trend, which weakens with decreasing exoplanetary size (Teske 2024), is valid for smaller and terrestrial exoplanets (e.g., Buchhave et al. 2014; Wang & Fischer 2015; Petigura et al. 2018b; Adibekyan 2019; Wilson et al. 2022; Wanderley et al. 2025). In particular, Petigura et al. (2018b) found that the occurrence of warm Super-Earths ($10 < P_{\text{orb}} \leq 100$ days and $1 \leq R_{\text{pl}} < 1.7 R_{\oplus}$) remains nearly constant across metallicities ranging from -0.4 to +0.4 dex, with an occurrence rate of 20 warm Super-Earths per 100 stars. For warm Sub-Neptunes ($1.7 \leq R_{\text{pl}} < 4 R_{\oplus}$), this number doubles to 40 per 100 stars. However, for hot super-Earths ($P_{\text{orb}} \leq 10$ days), they found an exoplanet occurrence of 4% for stars with [Fe/H] between -0.4 dex and -0.2 dex, growing to 10% for more metal-rich stars, with [Fe/H] between +0.2 dex and +0.4 dex. Also, for hot sub-Neptunes, the occurrence rates increase from 1% to 8%, respectively, when the same metallicity intervals are considered. This was also observed by Mulders et al. (2016), who found that the occurrence rate of hot small exoplanets ($R_{\text{pl}} < 4 R_{\oplus}$) around host stars with super-solar metallicities is three times higher compared to host stars with subsolar metallicities.

With the increasing number of stellar abundance studies due to the availability of high-quality spectra, especially from the large spectroscopic surveys, we can now analyze the planet-metallicity correlation in more detail, particularly for smaller exoplanets detected by the Kepler and TESS missions. Wilson et al. (2022), using abundance data from the Apache Point Observatory Galactic Evolution Experiment (APOGEE, Majewski et al. 2017), explored the star-planet connection for 10 elements (C, Mg, Al, Si, S, K, Ca, Mn, Fe, and Ni). They confirmed the results from Petigura et al. (2018b) regarding exoplanet occurrence rate with Fe and found that hot exoplanet occurrence rates increase by $\sim 20\%$ for Super-Earths and $\sim 60\%$ for Sub-Neptunes with an enhancement of 0.1 dex for all studied elements. However, for warm exoplanet occurrence rates, these correlations were found to be weaker. Ghezzi et al. (2026) determined abundances of 13 refractory elements (Na, Mg, Al, Si, Ca, Sc, Ti, V, Cr, Mn, Co, Ni and Cu) for 561 exoplanet-hosting stars of the California-Kepler Survey (Petigura et al. 2017) using high-resolution Keck/HIRES spectra and found that [X/H] abundances for Al, Si, Ca, Fe, Co, and Ni are statistically higher for systems with only hot planets relative to systems with only warm exoplanets. They also found that stars with only large exoplanets have significantly larger [X/H] abundances for Al, Si, Sc, Ti, Cr, Fe, and Co relative to stars with only small exoplanets.

Concerning previous abundance results for the bioessential elements C, O, and S in samples of exoplanet hosts, Costa Silva et al. (2020) determined sulfur abundances for 719 FGK stars of the HARPS-GTO sample and reported no differences in the sulfur distributions between stars with and without detected exoplanets for metallicities [Fe/H] > -0.3 dex. They also found that lower-mass exoplanets (super-Earths and Neptune-size) are more likely to orbit stars with higher [S/Fe]³. Delgado Mena et al. (2021), analyzing stars from the same HARPS sample with [Fe/H] $\gtrsim -0.2$ dex, found no significant differences in the distribution of [C/Fe] for populations of stars hosting exoplanets above and below $30 M_{\oplus}$. The earlier study by Brugamyer et al. (2011) found no significant probability that the exoplanet detection rate depends on the oxygen abundance of the host star ($\sim 45\%$).

Elemental abundance ratios can provide important information with respect to the distribution of chemical species in protoplanetary disks, serving as probes of the relative location of planet formation (e.g., Thiabaud et al. 2015a, 2015b). C/O⁴ was the first elemental ratio proposed to trace giant planet formation (e.g., Seager et al. 2005; Öberg et al. 2011), as the availability of C and O in the protoplanetary disk governs where the planet accretes most of its mass (e.g., Thiabaud et al. 2015b). Probing stellar C/O ratios of a sample of 16 hot Jupiters, Teske et al. (2014) found no significant trends for the host star C/O ratio as a function of exoplanet equilibrium temperature and radius. Suárez-Andrés et al. (2018) investigated C/O versus exoplanet mass in a sample of 99 solar-type planet-hosting stars of the HARPS-GTO sample and found that 86% of the stars hosting high-mass exoplanets ($M_{\text{pl}} > 30 M_{\oplus}$) presented C/O ratios between 0.4 – 0.8, while 14% had C/O below 0.4, obtaining average C/O ratios of 0.46 ± 0.11 and 0.50 ± 0.10 for stars hosting low- and high-mass exoplanets, respectively. Also, Sharma et al. (2024) determined C, N, O, Mg, Si and Fe abundances for a sample of 149 F-, G- and K-dwarfs and giant planet-hosting stars using high-resolution VUES (Vilnius University Echelle Spectrograph) spectra and found no relationship for stellar [C/Fe], [O/Fe] and C/O with exoplanetary mass.

There is still a significant number of stars, especially planet-hosting ones, that have no abundance determinations for a variety of elements besides Fe. For instance, $\sim 24\%$ of the stars in the Hypatia catalog⁵ (Hinkel et al. 2014) do not have

³ [X/Fe] = [X/H] - [Fe/H]

⁴ C/O = $10^{A(\text{C}) - A(\text{O})}$, where A(X) is the absolute abundance of X, i.e., A(X) = $\log(N_X)$.

⁵ hypatiacatalog.com

results for carbon abundances, while $\sim 25\%$ and $\sim 57\%$ do not have O and S abundances, respectively. Moreover, those stars for which these abundance results are available may be accompanied by large uncertainties. Since these elements are important not only for planet formation, but also for exoplanet habitability, one of the fundamental contributions that can be made in this topic is increasing the availability of homogeneous abundances and, furthermore, improving their precision – especially for elements that are biologically and geologically essential for life on Earth, since they can provide valuable insights into internal composition and, consequently, planetary habitability (e.g., [Hinkel & Unterborn 2018](#)). Habitability is, nowadays, a robust area that permeates various fields of knowledge and incorporates models of planetary formation and composition (e.g., [Thiabaud et al. 2015a, 2015b](#)), climate models (e.g., [Shields 2019](#)), ecology models (e.g., [Méndez et al. 2021](#)), geological cycles, and plate tectonics (e.g., [Ehlmann et al. 2016](#)), among others. Due to these advances, the concept of habitability itself has broadened, considering not only the presence of liquid water on the surface of the planet, but also the availability of elements essential for life on Earth (CHNOPS) over a long timescale, in order for life to thrive and survive (e.g., [Krijt et al. 2023](#)).

In this work, using publicly available high-resolution HARPS-South and HARPS-North spectra, we contribute to the increase of homogeneous chemical abundance results for the bioessential elements C, O and S, as well as the refractory elements Fe and Ni, in solar-type planet-hosting stars. Ensuring a homogeneous determination of stellar atmospheric parameters (T_{eff} , $\log g$, $[\text{Fe}/\text{H}]$), evolutionary parameters (R_* , M_* and age), and chemical abundances is essential for minimizing systematic uncertainties and discrepancies introduced by varying analysis methods. A uniform approach helps preserve the reliability of comparisons and any detected correlations. Efforts such as the one presented in this work, of homogeneously characterizing planet-hosting stars using high-resolution spectra, are increasingly important as we search for star-planet connections and chemical abundances are now being obtained for exoplanet atmospheres. For example, observations from the James Webb Space Telescope are already exploring a new diversity of molecules in the atmosphere of giant exoplanets that could not be observed with the Hubble Space Telescope, such as the detection of SO_2 in the atmosphere of exoplanets (e.g., [Alderson et al. 2023](#); [Gressier et al. 2025](#)). In this context, here we will investigate the star-planet connection by probing the relationships between detailed chemical abundances of host stars and exoplanet properties such as radius, orbital period, mass, and equilibrium temperature. The results from such efforts may contribute to future refinement of planet formation theories, exploring deeply how the distribution of molecules evolve through the protoplanetary disk and how similar is the final composition of exoplanets in comparison to their host stars.

This paper is organized as follows. The stellar and exoplanetary samples are described in Section 2. Stellar parameters and chemical abundances are determined in Section 3 and 4, respectively, and the exoplanetary radii in Section 5. In Section 6, we discuss the chemical evolution of our sample of exoplanet hosts. In Section 7, we discuss the star-planet connection. Lastly, our concluding remarks are presented in Section 8.

2. SAMPLE AND DATA

We selected confirmed host stars from the NASA Exoplanet Archive ([NASA Exoplanet Archive 2025⁶](#), [Akeson et al. 2013](#)) according to the following criteria: $5000 \text{ K} \leq T_{\text{eff}} \leq 6500 \text{ K}$ and $\log g \geq 4.0$ dex, and with exoplanets having transit depth determinations. Among the 1399 initially selected stars, we obtained good quality high-resolution spectra for 308 stars. This sample is composed mostly of F- and G-dwarfs with some K-type stars and subgiants. The coordinates and the identification of the spectra used are presented in Appendix A.

The data used for this work consist of publicly available high resolution HARPS-South ([Mayor et al. 2003](#)) and HARPS-North ([Cosentino et al. 2012](#)) spectra from ESO Science Archive Facility⁷ and the Italian Center for Astronomical Archive (IA2)⁸, respectively. The HARPS (High Accuracy Radial velocity Planet Searcher, [Mayor et al. 2003](#)) spectrographs are twins, have a resolution of $R \sim 115,000$ and cover the wavelength range $3780 - 6910 \text{ \AA}$. The southern spectrograph is at the ESO 3.6 m telescope, in La Silla, Chile, and the northern spectrograph is at the 3.6 m Telescopio Nazionale Galileo (TNG), in La Palma, Canary Islands, Spain. The spectra obtained were already reduced with their instrument pipelines. We corrected them for radial velocity using PyRAF⁹ `fxcor` task with the Ceres 2009-02-08 solar spectrum¹⁰ as a template between $6040 - 6200 \text{ \AA}$. We combined the spectra of each star to improve SNR using PyRAF

⁶ Accessed on 2025-09-12 at 08:55, returning 38778 rows. This dataset or service is made available by the NASA Exoplanet Science Institute at IPAC, which is operated by the California Institute of Technology under contract with the National Aeronautics and Space Administration.

⁷ https://archive.eso.org/wdb/wdb/adp/phase3_spectral/form

⁸ <http://archives.ia2.inaf.it/tng/>

⁹ PyRAF is a command language for Tody1986 based on the Python scripting language. It was developed at the Space Telescope Science Institute (STScI).

¹⁰ HARPS Solar Spectra Collection (<https://www.eso.org/sci/facilities/lasilla/instruments/harps/inst/monitoring/sun.html>)

Star	G (mag)	G _{BP-RP} (mag)	π (mas)	V (mag)	A _V (mag)	DR
55 Cnc	5.7144±0.0028	1.0135±0.0048	79.4274±0.0777	5.9169±0.0460	0.4184	2
BD+20 594	10.8665±0.0028	0.8733±0.0047	5.6384±0.0143	11.0361±0.0303	0.2418	E3
CoRoT-1	13.4454±0.0028	0.7692±0.0049	1.3000±0.0167	13.5825±0.0303	0.3345	E3
CoRoT-4	13.5490±0.0028	0.7600±0.0049	1.3623±0.0157	13.6835±0.0303	0.1365	E3

T_{eff} (K)	$\log g$	[Fe/H]	v_{mic} (km s ⁻¹)	Age (Gyr)	R _* (R _⊙)	M _* (M _⊙)
5283±49	4.44±0.13	0.40±0.03	0.730±0.080	10.638±0.930	1.091±0.013	0.946±0.015
5690±13	4.34±0.04	-0.16±0.01	0.979±0.030	11.085±0.517	1.134±0.006	0.913±0.023
6337±30	4.42±0.06	-0.05±0.02	1.463±0.070	2.325±0.408	1.263±0.016	1.191±0.024
6295±38	4.62±0.09	0.11±0.02	1.426±0.070	0.288±0.147	1.123±0.009	1.205±0.026

A(C)	A(O)	A(S)	A(Ni)	SNR 5052	SNR 5380	SNR 6300	SNR 6743-6758	SNR
8.80±0.07	8.86±0.25	7.47±0.05	6.70±0.04	539	621	522	476	486
8.41±0.03	8.71±0.03	7.06±0.06	6.06±0.02	168	170	197	201	150
8.34±0.04	-	7.17±0.06	6.10±0.04	94	98	79	114	87
8.46±0.05	-	7.18±0.04	6.27±0.03	82	85	82	99	75

Table 1. Sample of exoplanet-hosting stars. Column 1 shows the stellar identification. Columns 2 – 4 show Gaia’s G magnitude, G_{BP-RP} color and parallax, respectively. Column 5 shows calculated V magnitude. Columns 6 and 7 shows StarHorse’s extinction and which Gaia Data Release is the A_V based on. Columns 8 – 11 show the atmospheric parameters. Columns 12 – 14 show age, radius and mass, respectively. Columns 15 – 18 show the absolute abundances of C, O, S and Ni, respectively. Columns 19 – 22 show the SNR of the spectral orders that contain the C I line at 5052 Å, C I line at 5380 Å, [O I] line at 6300 Å and all S I lines between 6743 – 6758 Å. Column 23 shows the total SNR of the combined spectra.

NOTE—This table is published in its entirety in the machine-readable format. A portion is shown here for guidance regarding its form and content.

`scombine` task. For the final combined spectra, the median SNR is 145 with ~33% having SNR < 100, ~28% having 100 ≤ SNR < 200, ~14% having 200 ≤ SNR < 300 and ~25% having SNR ≥ 300. The final SNR and the number of spectra combined are listed in Table 1. The SNR value used for each individual spectrum is the one available in the header of the fits file and the final SNR of the combined spectrum is calculated as $\text{SNR}_{\text{combined}} = \sqrt{\sum_i \text{SNR}_i^2}$.

3. STELLAR PARAMETERS

3.1. Atmospheric Parameters

We determined the effective temperatures (T_{eff}), surface gravities ($\log g$), microturbulence velocities (v_{mic}) and metallicities ([Fe/H]), along with their uncertainties, using the methodology described in Ghezzi et al. (2018; Martinez et al. 2019; 2021) (hereafter, G18 and G21, respectively), which employs a classical spectroscopic method based on the excitation and ionization equilibria of Fe I and Fe II lines in an automated Python pipeline. Briefly, it uses: (i) a line list containing atomic parameters for 158 Fe I and 18 Fe II lines between 5023 – 6862 Å (see Table C.2 of G18); (ii) equivalent widths (EWs) of the iron lines; (iii) Kurucz ATLAS9 ODFNEW 1-D plane parallel model atmospheres (Castelli & Kurucz 2003); (iv) driver `abfind` of the Local Thermodynamic Equilibrium (LTE) line analysis code MOOG¹¹ (Snedden 1973), version FEB2017. The equivalent widths were measured using the ARES v2 code¹² (Sousa et al. 2007, 2015) adopting the parameters $\text{smoothder} = 4$, $\text{space} = 2.0 \text{ m}\text{\AA}$, $\text{lineresol} = 0.1 \text{ m}\text{\AA}$, $\text{miniline} = 5$ and rejt as the SNR value of the spectrum.

The final atmospheric parameters for 308 stars and are listed in Table 1. The median values for the uncertainties of the 308 stars are 22 K for T_{eff} , 0.02 dex for [Fe/H], 0.06 dex for $\log g$ and 0.040 km s⁻¹ for v_{mic} . Finally, as

¹¹ <http://www.as.utexas.edu/chris/moog.html>

¹² <https://github.com/sousasag/ARES>

a consistency check, we determined solar atmospheric parameters using the Ceres 2009-02-08 solar spectrum (see Section 2) and found $T_{\text{eff}} = 5759 \pm 18$ K, $[\text{Fe}/\text{H}] = 0.00 \pm 0.01$ dex where $A(\text{Fe})_{\odot} = 7.50$ dex (Asplund et al. 2009), $\log g = 4.43 \pm 0.05$ dex and $v_{\text{mic}} = 0.936 \pm 0.030$ km s $^{-1}$. Therefore, they are in excellent agreement with canonical solar values. We note that 18 stars were outside of our selection criteria of $5000 \text{ K} \leq T_{\text{eff}} \leq 6500 \text{ K}$ and $\log g \geq 4.0$ dex. Finally, we show the Kiel diagram of the 290 stars in Figure 1.

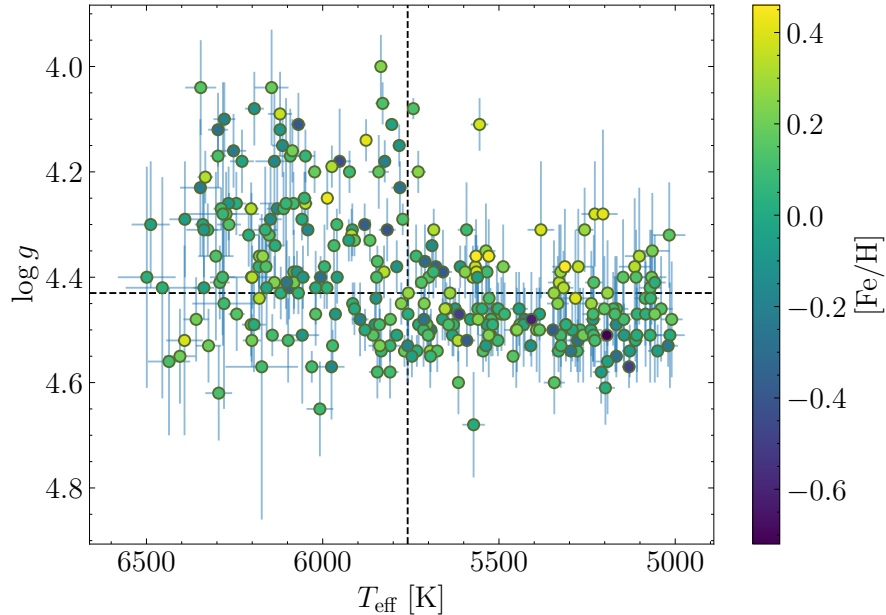


Figure 1. Kiel diagram for 290 stars with $5000 \text{ K} \leq T_{\text{eff}} \leq 6500 \text{ K}$ and $\log g \geq 4.0$ dex analyzed in this work. The dashed black lines present the solar values obtained for the Ceres 2009-02-08 solar spectrum, $T_{\text{eff}} = 5759 \pm 18$ K, $\log g = 4.43 \pm 0.05$ dex and $[\text{Fe}/\text{H}] = 0.00 \pm 0.01$ dex.

3.2. Evolutionary Parameters

We determined stellar ages, radii, masses and surface gravities using the isochrone method with PARAM code v1.3¹³ (da Silva et al. 2006), which consists in comparing the positions of stars with theoretical isochrones in a color-magnitude diagram. The code performs a Bayesian estimation of stellar evolutionary parameters using a grid of PARSEC isochrones (Bressan et al. 2012), stellar observables as input parameters (T_{eff} , $[\text{Fe}/\text{H}]$, parallax and V magnitude) and the default Bayesian priors, which are lognormal IMFs from Chabrier (2001), constant stellar formation rate (SFR) and an age interval between 0.1 – 12 Gyr. The effective temperatures and metallicities were spectroscopically determined in this work (see Section 3.1). The parallaxes, G magnitudes and $G_{\text{BP}} - G_{\text{RP}}$ colors were obtained from Gaia DR2 (Gaia Collaboration et al. 2018) and DR3 data (Gaia Collaboration et al. 2021). In order to calculate the V magnitudes, we used the photometric relationships from Gaia DR2 Documentation Release 1.2¹⁴ and Gaia DR3 Documentation Release 1.3¹⁵ between Gaia and Johnson-Cousins system. For Gaia DR2 (see Chapter 5.3.7, Table 5.8),

$$G-V = -0.017600 - 0.006860(G_{\text{BP}} - G_{\text{RP}}) - 0.173200(G_{\text{BP}} - G_{\text{RP}})^2, \quad (1)$$

with a calibration uncertainty of 0.045858 mag associated with the photometric relationship. Thus, the final uncertainty for V is calculated in the form

$$\sigma_V = \sqrt{(\sigma_G)^2 + ((0.006860 + 0.346400(G_{\text{BP}} - G_{\text{RP}}))\sigma_{G_{\text{BP}}-G_{\text{RP}}})^2 + 0.045858^2}. \quad (2)$$

For Gaia DR3 (Chapter 5.5.1, Table 5.9),

$$G-V = -0.02704 + 0.01424(G_{\text{BP}} - G_{\text{RP}}) - 0.2156(G_{\text{BP}} - G_{\text{RP}})^2 + 0.01426(G_{\text{BP}} - G_{\text{RP}})^3, \quad (3)$$

¹³ PARAM web interface is maintained by Léo Girardi at the Observatorio Astronomico di Padova (https://stev.oapd.inaf.it/cgi-bin/param_1.3).

¹⁴ <https://gea.esac.esa.int/archive/documentation/GDR2/>

¹⁵ <https://gea.esac.esa.int/archive/documentation/GDR3/>

with a calibration uncertainty of 0.03017 mag associated with the photometric relationship. Thus, the final uncertainty for V is calculated in the form

$$\sigma_V = \sqrt{(\sigma_G)^2 + (-0.01424 + 0.4312(G_{BP} - G_{RP}) - 0.04278(G_{BP} - G_{RP})^2)\sigma_{G_{BP}-G_{RP}})^2 + 0.03017^2}. \quad (4)$$

We corrected the V magnitudes for extinction using A_V values calculated with the `StarHorse` code (Queiroz et al. 2018), which is an isochrone-fitting code that compares observed quantities to stellar evolutionary models to derive distances, extinctions, ages, masses, effective temperatures, metallicities and surface gravities for field stars. The code has updated versions for better performance with Gaia EDR3 data (Anders et al. 2022), using extinction maps of Green et al. (2019) and Drimmel et al. (2003), and Gaia DR2 data (Anders et al. 2019), using its own StarHorse-derived extinction map. For 11 stars, we used DR2 data for magnitudes, parallaxes and A_V since no A_V correction was available in StarHorse EDR3. For 1 star, TOI-238, there is no parallax available in Gaia. Finally, for 2 stars, Kepler-449 and Kepler-477, no A_V was available in StarHorse DR2/EDR3 so we did not determine their evolutionary parameters.

We obtained evolutionary parameters for 300 stars (see Figure 2). We note that, for five stars, PARAM did not converge (K2-173, K2-180, Kepler-444, Kepler-990 and TOI-561). The evolutionary parameters determined for the stars, as well as their G and V magnitudes, G_{BP-RP} color, A_V and parallaxes, are listed in Table 1. The median values for the uncertainties are 0.64 Gyr for age, 1.3% for R_\star and 1.3% for M_\star .

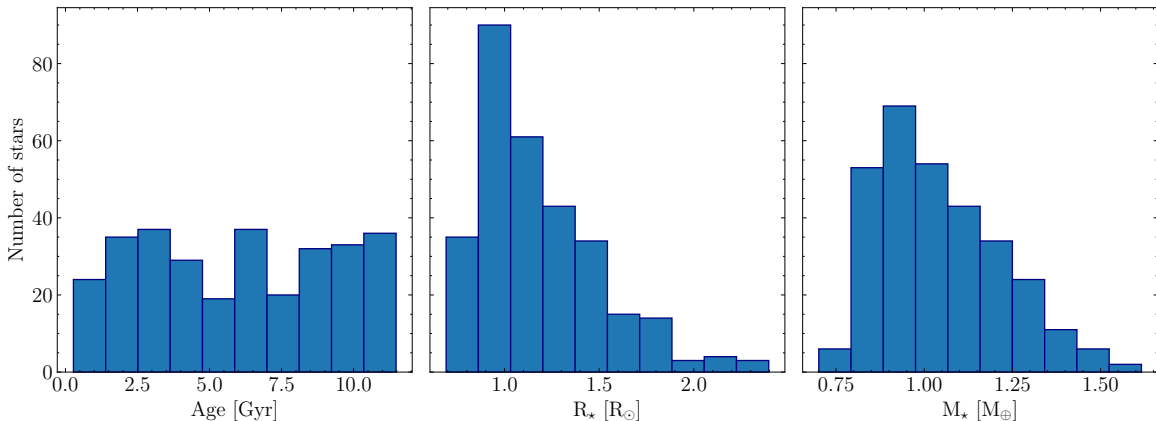


Figure 2. Evolutionary parameters determined for 300 stars using PARAM code v1.3 (da Silva et al. 2006).

Finally, the 18 stars outside of our selection criteria of $5000 \text{ K} \leq T_{\text{eff}} \leq 6500 \text{ K}$ and $\log g \geq 4.0$ dex have not been included in the following abundance analysis. Comparisons with other results from the literature for atmospheric parameters (Soubiran et al. 2022) and stellar radii (Stassun et al. 2017; Petigura et al. 2018a; Kruse et al. 2019; Loaiza-Tacuri et al. 2024) for stars in common with this study are presented in Appendix B.

4. CHEMICAL ABUNDANCES

The atomic parameters for the C I, Ni I, and S I lines were taken from the Vienna Atomic Line Database¹⁶ (VALD, Ryabchikova et al. 2015), with the exception of their $\log gf$ values for which we used solar $\log gf$ values – following the procedure described in Ghezzi et al. (2026). Although Ni is not a bioessential element, its inclusion was needed for the oxygen determination (see Section 4.2). For the region around the [O I] line, the atomic parameters of [O I] and nearby lines were also taken from VALD, but we used the $\log gf$ value from Allende Prieto et al. (2001) for [O I], and, for the two Ni I lines blended with the [O I], we used the weighted $\log gf$ values from Bensby et al. (2004), which are based on the laboratory measurements of Johansson et al. (2003). The line lists can be found in Table 2.

We measured the EWs of the C I, Ni I and S I lines using ARES v2 with the same parameters used for Fe I and Fe II lines (see Section 3), except for C I, for which we used $lineresol = 0.2 \text{ m\AA}$ as it yielded EWs more consistent with manual measurements. Also, for the C I and S I lines, the SNR adopted for the rej_t parameter is the SNR of

¹⁶ <http://vald.astro.uu.se/>

ID	λ_{central} (Å)	Ion	χ (eV)	$\log gf$	$\log \Gamma_w$ $(4\pi s N_H)^{-1}$
C I	5052.167	6.0	7.685	-1.318	0.000
C I	5380.337	6.0	7.685	-1.608	0.000
S I ⁸	6743.483	16.0	7.866	-1.555	-7.160
S I ⁸	6743.540	16.0	7.866	-1.104	-7.160
S I ⁸	6743.580	16.0	7.866	-1.004	-7.160
S I ⁸	6743.580	16.0	7.866	-1.354	0.000
S I ⁸	6743.640	16.0	7.866	-1.184	0.000
S I ⁸	6756.750	16.0	7.870	-1.915	-7.160
S I ⁸	6756.851	16.0	7.870	-2.005	0.000
S I ⁸	6756.960	16.0	7.870	-1.075	-7.160
S I ⁸	6757.150	16.0	7.870	-0.485	-7.160
Ni I	5010.938	28.0	3.635	-0.918	-7.225

Table 2. List of atomic parameters of the C, S and Ni lines. The S I lines are highlighted with their multiplet numbering from Moore (1945). The columns list, respectively, the line identification, central wavelength, ionization stage following the format used by MOOG (0 means neutral), excitation potential, $\log gf$ and the logarithm of the van der Waals damping constant.

NOTE—This table is published in its entirety in the machine-readable format. A portion is shown here for guidance regarding its form and content.

the echelle order that includes each spectral line¹⁷. For the Ni I lines, we adopted the median SNR of the spectrum – as it was the case for the Fe I and Fe II lines (see Section 3.1). Finally, for some stars, C I or/and S I EWs provided unrealistic abundances. In such cases, they were measured using the `splot` task from PyRAF. If this did not resolve the issue, the lines were removed.

4.1. Carbon, Nickel and Sulfur

Carbon, whose dominant isotope is ¹²C, is formed by stars primarily during hydrostatic helium burning via the triple- α process. The stars that contribute most to carbon enrichment are of low- and intermediate-mass ($0.8 M_{\odot} \leq M_{\star} \leq 8 M_{\odot}$, Matteucci 2016), as high-mass stars process a large part of their C through the ¹²C(α, γ)¹⁶O reaction. The main optical indicators used to determine C abundances in FGK stars are atomic lines of C I (e.g., 5052 Å, 5380 Å and 6580 Å) and the molecular band of CH around 4300 Å, but with only reasonable agreement between atomic and molecular abundances (e.g., Delgado Mena et al. 2021). The atomic lines listed above have high excitation potentials, around 8 eV, and become weak in cool stars. On the other hand, the CH band is strong and shapes the continuum around it. In this work, carbon abundances were determined based on 2 lines of C I, 5052 Å and 5380 Å, using the MOOG driver `abfind` (see Table 2).

Sulfur, with the dominant isotope ³²S comprising 95% of solar system S, is formed by high-mass stars during oxygen burning, which occurs in the final stages of evolution in massive stars (e.g., Limongi & Chieffi 2003). The main indicators used historically to determine S abundances are the multiplets of S I at 6046 Å, 6052 Å, 6743 Å, 6757 Å, 8694 Å, 9228 Å and 10456 Å (e.g., Caffau et al. 2005; Spite et al. 2011; Costa Silva et al. 2020) and the forbidden line [S I] at 10821 Å (e.g., Matrozis et al. 2013). Therefore, the determinations of sulfur abundances require more robust techniques due to blending with its own lines, in the case of multiplets, increasing the associated uncertainties. As a result, sulfur is an element that has historically been neglected in studies of α -element abundances, being overshadowed by Si and Ca (Caffau et al. 2005). Thus, sulfur abundances are not easily found in the literature, with notable works by Luck & Heiter (2005), for stars in the northern hemisphere, and Costa Silva et al. (2020), for stars in the southern hemisphere. In this work, sulfur abundances were determined based on 9 lines from multiplet 8 of S I¹⁸, between 6743 – 6758 Å, using the MOOG driver `blends` (see Table 2).

Nickel is formed mainly in the very final stage of the life of massive stars and during type Ia supernovae (e.g., Woosley & Weaver 1995; Limongi & Chieffi 2003). For massive stars, before core collapse, ⁵⁶Fe and ⁵⁶Ni are formed by

¹⁷ The wavelength coverage of each spectral order of HARPS is available at https://www.eso.org/sci/facilities/lasilla/instruments/harps/inst/spec_form.html and, for HARPS-N, at <https://www.tng.iac.es/instruments/harps/data/usermanv3.1.pdf>

¹⁸ Multiplet numbering from Moore (1945).

successive fusion of quasi-equilibrium reactions (α -particle capture) during explosive burning of silicon (Arnett 1996). During a supernova Ia explosion, explosive thermonuclear nucleosynthesis further enhances Fe and Ni production, particularly of ^{56}Ni that decays into iron, contributing to $\sim 2/3$ of total iron of the Galaxy (Mishurov & Tkachenko 2019). Also, due to their similar nucleosynthetic paths, the evolution of iron-peak elements (e.g., Ni, V, Cr, Mn, Co) tracks Fe. The dominant isotopes of iron and nickel are ^{56}Fe and ^{58}Ni . The main indicators used to determine Ni abundances are atomic lines of Ni I in the optical region (e.g., Adibekyan et al. 2012b; Ghezzi et al. 2026; Kirby et al. 2018). In this work, nickel abundances were determined based on 39 lines of Ni I (Ghezzi et al. 2026), between 5010 – 6843 Å, using the MOOG driver `abfind` (see Table 2). Finally, nickel abundances are determined as they are required for determining oxygen abundances (see Section 4.2).

4.2. Oxygen

Oxygen-16, the dominant O-isotope, is formed by high-mass stars during the hydrostatic burning of helium via $^{12}\text{C}(\alpha, \gamma)^{16}\text{O}$ and is ejected into the interstellar medium through supernova type II explosions. The main indicators used to determine O abundances in FGK stars are the O I line at 6158 Å (e.g., Bertran de Lis et al. 2015), the forbidden [O I] lines at 6300 Å and 6363 Å (e.g., Allende Prieto et al. 2001; Bertran de Lis et al. 2015), and the O I triplet at 7774 Å (e.g., Steffen et al. 2015; Amarsi et al. 2019; Bergemann et al. 2021). However, the 6158 Å and 6363 Å lines are not widely used due to their small equivalent widths, while the forbidden line at 6300 Å is strongly blended with 2 Ni I lines, and the triplet suffers from significant non-LTE deviations (e.g., Amarsi et al. 2019; Bergemann et al. 2021). Moreover, the lines at 6158 Å and 7774 Å have high excitation potentials, ~ 10.7 eV and ~ 9.2 eV, respectively, i.e., they become weak for cooler stars. Lastly, just like carbon, there can be discrepancies between the abundances based on different indicators (e.g., Allende Prieto et al. 2001; Bergemann et al. 2021). Even for the Sun, we find discrepancies between different methods and its measured oxygen abundance has changed considerably over the past 50 years: 8.92 dex by Lambert (1978); 8.66 ± 0.05 dex by Asplund et al. (2004); 8.76 ± 0.07 dex by Caffau et al. (2008); 8.69 ± 0.05 dex by Asplund et al. (2009); 8.80 ± 0.03 dex by Cubas Armas et al. (2020); 8.75 ± 0.03 dex by Bergemann et al. (2021); 8.69 ± 0.04 dex by Asplund et al. (2021).

Oxygen abundances here were determined based on the forbidden line [O I] at 6300.304 Å, using the MOOG driver `synth`, with *damping* parameter set to 1 and a Gaussian broadening for the line, i.e., *g* option. There are telluric features around the [O I] line, so in order to avoid possible contamination, we determined their position by using the telluric spectrum from Wallace et al. (2011) and Doppler shifting it according to every individual stellar spectrum’s barycentric Earth radial velocity (available in the header of the fits file) and radial velocity (determined in this work, see Section 2). We used only the spectra in which a region of 0.15 Å around the center of the [O I] line was clean of any telluric features. In Figure 3, we show an example of this procedure. For the star HD 220197, we see the superposition of the regions that represent the [O I] line (blue) and the telluric features (pink) in the upper three panels. Hence, these 3 spectra were not considered for our analysis. For the clean spectra, we manually removed the ones containing any sort of contamination, e.g., cosmic rays and/or deformations. Finally, the remaining spectra of each star were combined, to improve SNR, and normalized around the region including the [O I] line, between 6295 – 6305 Å, and also between 6235 – 6245 Å. This second region contains a Fe I line at 6240.646 Å that we use for the FWHM determination of the spectra (see below). From the 290 stars, 230 of them had clean spectra in the [O I] region.

Initial simple syntheses were performed using $g = 0.055$ Å based on the resolution of 115000 of HARPS’ twin spectrographs ($\text{FWHM}_{\text{inst}}$). Based on these synthetic spectra, we adjusted the central wavelength of the lines by shifting their wavelengths in 2 rounds: (i) within ± 0.10 Å with steps of 0.01 Å; (ii) $w \pm 0.01$ Å with steps of 0.001 Å, where w is the best match found for the first round. The best match between the observed and the synthetic spectra was calculated through the minimization of the reduced χ^2 (e.g., Ghezzi et al. 2009, 2010b, 2018),

$$\chi_r^2 = \frac{1}{(d-1)} \sum_{i=1}^n \frac{(O_i - S_i)^2}{\sigma^2}, \quad (5)$$

where d is the number of degrees of freedom and is defined as $d = n - p$, n being the number of points in the observed spectra and p the number of free parameters (in the wavelength adjustment, $p = 1$); O_i and S_i are, respectively, the normalized observed and synthetic fluxes at point i and σ is the uncertainty of the observed continuum, defined as $\sigma = (\text{SNR})^{-1}$. For the Fe I line, we considered the 6240.50 – 6240.78 Å range for the reduced χ^2 analysis and, for [O I], 6300.10 – 6300.50 Å.

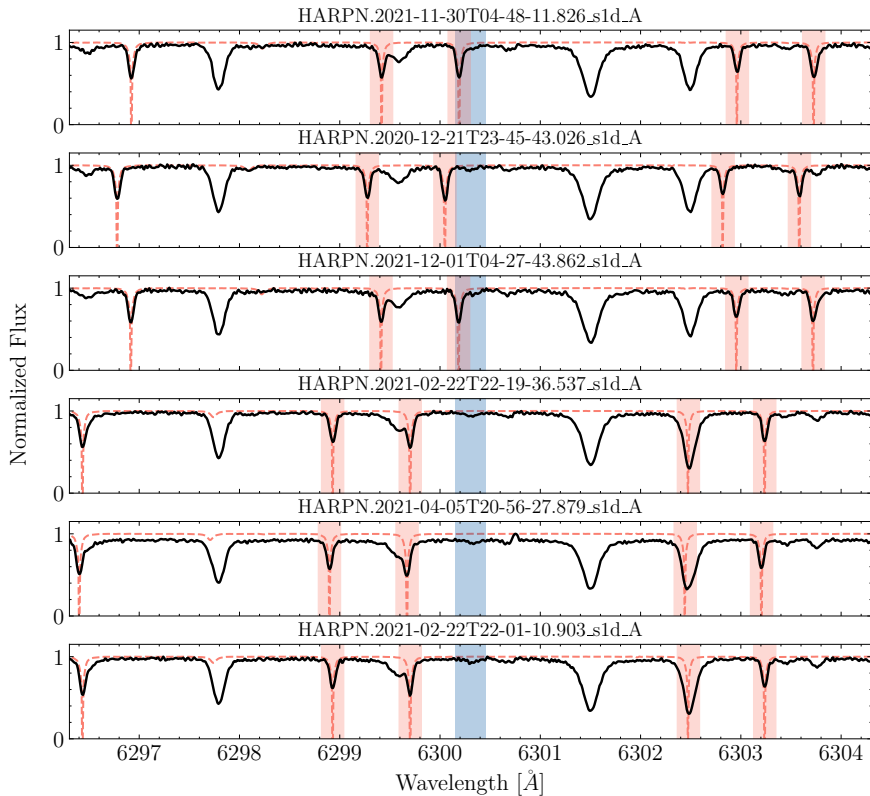


Figure 3. Telluric features around the oxygen forbidden line at 6300.304 \AA on the spectra of HD 220197. HD 220197 spectra are shown in black and the shifted telluric spectra in dashed pink. The blue filled regions represent the range of $\pm 0.15 \text{ \AA}$ around the [O I] line and the pink filled regions are the regions contaminated by the telluric features. The upper three panels show examples of contamination on the [O I] line, while the lower three have no contamination.

To adjust the local continuum around the Fe I line, a similar reduced χ^2 procedure was applied. In this case, we shifted the continuum within ± 0.050 of the original continuum with steps of 0.001 for only one round. For the [O I] line, due to its weakness and the presence of strong lines nearby (3 Si I lines at $\sim 6299.5 \text{ \AA}$ and 2 Fe I lines at $\sim 6301.6 \text{ \AA}$), noise was an issue. Thus, we smoothed the observed spectra using the moving average filter, which consists in expressing the data as a series of averages of different sections of itself, removing noisy fluctuations and retaining the true signal. For this, we applied a window size of 5. Finally, we adjusted the maximum of the smoothed local continuum to the maximum of the synthetic spectra between $6300.00 - 6300.55 \text{ \AA}$.

To determine the FWHM of the spectral lines, we used the Fe I line at 6240.646 \AA ¹⁹ because it is the closest moderately strong line ($\chi_e = 2.223 \text{ eV}$) that is isolated and has a clear local continuum. The FWHM adjustment was performed in 3 rounds, using $p = 1$: (i) FWHM varying within $0.05 - 0.25 \text{ \AA}$ with steps of 0.05 \AA ; (ii) FWHM varying within $s \pm 0.05 \text{ \AA}$ with steps of 0.01 \AA , where s is the best match found for the first round; (iii) FWHM varying within $s \pm 0.01 \text{ \AA}$ with steps of 0.001 \AA , where s is the best match found for the second round. In all of these rounds, we set the [Fe/H] as the abundance determined for the 6240 \AA Fe I line during the atmospheric parameters determination using the `abfind` driver.

The [O I] line is blended with 2 Ni I lines – up to 60% of the flux of the [O I] line may be attributed to the Ni I contribution (Bertran de Lis et al. 2015) – and weakly contaminated by a CN line, besides the telluric contamination mentioned above (e.g., Allende Prieto et al. 2001; Teske et al. 2013). Accordingly, we performed the oxygen abundance determination in 2 rounds, using $p = 2$: (i) $A(\text{O})$ varying within $\pm 0.50 \text{ dex}$ with steps of 0.10 dex and $A(\text{Ni})$ fixed to the value determined for the star (see Section 4.1); (ii) $A(\text{O})$ varying within $o \pm 0.10 \text{ dex}$ with steps of 0.01 dex , where o is the best match found for the first round, and $A(\text{Ni})$ fixed to the value determined for the star. We stress that these values mentioned above are the ones from the `abundances` parameter of MOOG, having the final absolute

¹⁹ Excitation potential = 2.223 eV, $\log gf = -3.337$ and logarithm of the van der Waals damping constant = $-7.661 (4\pi s N_{\text{H}})^{-1}$.

abundance for the element $A(O) = 8.69 + o + [Fe/H]$ dex, where o is the best match for the second round and 8.69 is the solar absolute abundance from [Asplund et al. \(2009\)](#) (hereafter, A09). All best fits were inspected visually and, if needed, corrected manually. In [Figure 4](#), we show an example of the best fit for TOI-1710.

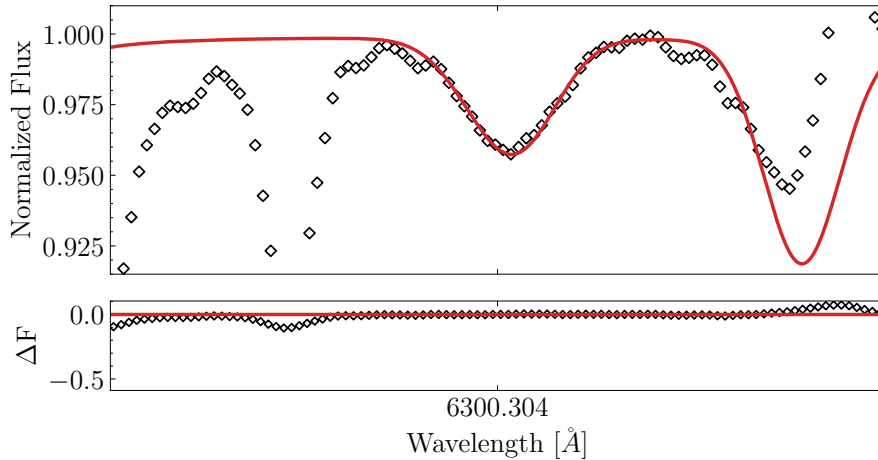


Figure 4. Example of the best fit for TOI-1710. The black diamonds represent the observed spectrum and the red line represent the synthetic spectrum. In the upper panel, we show the spectra and, in the lower panel, the residuals ($\Delta F = F_{\text{obs}} - F_{\text{synth}}$).

As a consistency check, we determined the abundances for the Ceres 2009-02-08 solar spectrum using the same methodology described above and found $A(C)_{\odot} = 8.42 \pm 0.06$ dex, $A(O)_{\odot} = 8.70 \pm 0.05$ dex, $A(S)_{\odot} = 7.15 \pm 0.02$ dex and $A(Ni)_{\odot} = 6.23 \pm 0.02$ dex in addition to $A(Fe)_{\odot} = 7.50 \pm 0.01$ dex. Comparing with values from A09, where $A(C)_{\odot} = 8.43 \pm 0.05$ dex, $A(O)_{\odot} = 8.69 \pm 0.05$ dex, $A(S)_{\odot} = 7.12 \pm 0.03$ dex, $A(Ni)_{\odot} = 6.22 \pm 0.04$ dex and $A(Fe)_{\odot} = 7.50 \pm 0.04$ dex, we find an excellent agreement. This is also true for the more recent values from [Asplund et al. \(2021\)](#) (hereafter, A21), where $A(C)_{\odot} = 8.46 \pm 0.04$ dex, $A(O)_{\odot} = 8.69 \pm 0.04$ dex, $A(S)_{\odot} = 7.12 \pm 0.03$ dex, $A(Ni)_{\odot} = 6.20 \pm 0.04$ dex and $A(Fe)_{\odot} = 7.46 \pm 0.04$ dex. Solar reference values from other authors can be found in [Section B.3](#).

4.3. Uncertainties

Given that the atmospheric parameters have uncertainties associated, we estimated the change in the determined abundances by varying each atmospheric parameter by its uncertainty (plus and minus) and assumed the higher abundance difference as the uncertainty associated with that specific parameter. Lastly, we calculated the final uncertainty through a sum of squares of the uncertainties related to the atmospheric parameters and to the standard deviation of the mean of the abundances calculated for each specific element,

$$\sigma_X = \sqrt{\sigma_{X, \text{Teff}}^2 + \sigma_{X, [Fe/H]}^2 + \sigma_{X, \text{logg}}^2 + \sigma_{X, \text{vmic}}^2 + \sigma_{\text{lines}}}. \quad (6)$$

We estimated the change in the oxygen abundance caused by the uncertainty associated with the Ni abundance ($\pm \sigma_{Ni}$) and we performed the same process described for the atmospheric parameters, but with Ni, and added $\sigma_{O, Ni}$ (uncertainty on O related to the variation of the Ni abundance) to the sum of squares.

The uncertainties of C, O, S and Ni have median values of 0.04 dex, 0.03 dex, 0.06 dex and 0.02 dex, respectively, having approximately 93%, 91%, 83% and 96% of the uncertainties below 0.10 dex. We note that the stars with high uncertainties can be split into 3 separate groups: i) $SNR < 85$; ii) $v_{\text{sin } i} > 10 \text{ km s}^{-1}$; iii) $[Fe/H] > 0.25$ dex. Finally, the determined abundances are listed in [Table 1](#). In total, we determined C, O, S and Ni abundances for 303, 230, 272 and 307 stars, respectively, for which 289, 225, 269 and 290 stars are from the sample with $5000 \text{ K} \leq T_{\text{eff}} \leq 6500 \text{ K}$ and $\log g \geq 4.0$ dex. Also, based on abundance data available on [VizieR²⁰](#) and [Hypatia](#) catalog, as of December 2025, we report, for the first time, carbon abundances for 75 stars, oxygen abundances for 63 stars, sulfur abundances for 115 stars and nickel abundances for 69 stars.

²⁰ VizieR catalogue access tool, operated at CDS, Strasbourg, France (<https://vizier.cds.unistra.fr>).

4.4. Trends of Abundances with the Effective Temperature

To investigate if there are any trends between the derived abundances and the effective temperature, we performed a linear regression²¹ between the absolute abundances of C, O, S and Ni with T_{eff} , and obtained R^2 values of 0.127, 0.112, 0.172 and 0.010 for C, O, S and Ni, respectively. For the angular coefficients, we obtained t -values of -6.461, 5.311, -7.439 and -1.720 and Pearson p -values of 0.000, 0.000, 0.000 and 0.086. Also, we performed Spearman tests, to investigate non-linear correlations, and obtained p -values of 0.000, 0.000, 0.000 and 0.042. In this work, we consider a statistically significant correlation if p -value < 0.001. Furthermore, in order to better account for possible fluctuations and to improve the robustness of the statistical analysis, we bootstrapped the samples 1000 times, performed the same tests and obtained median R^2 values of 0.127, 0.114, 0.171 and 0.011, median t -values of -6.464, 5.356, -7.429 and -1.745, median p -values of 0.000, 0.000, 0.000 and 0.080 and median Spearman p -values of 0.000, 0.000, 0.000 and 0.042 for C, O, S and Ni, respectively. In summary, there is a correlation between T_{eff} and C, O and S abundances mainly caused by the cooler stars.

To verify the location of a transition in T_{eff} where the Pearson and Spearman tests do not result in a statistically significant trend, we calculated the statistics for subsamples with a minimum T_{eff} varying from 5000 K to 5600 K in steps of 1 K. For C, O, and S, the T_{eff} in which Pearson and Spearman p -values > 0.001 and $|t\text{-value}| < 3$ are 5229 K, 5279 K and 5284 K. For Ni, the values are 0.087, 0.042 and -1.720 for Pearson and Spearman p -values and angular coefficient t -value, respectively, at 5000 K. We performed the same tests using bootstrap with steps of 50 K and found no trends for subsamples with T_{eff} above 5300 K, 5300 K and 5350 K for C, O, and S, respectively. In Figure 5, we show the distribution of $[X/H]$ with effective temperature and the OLS regressions of the complete (black lines) and temperature restricted (orange lines) samples. Below, we explore the T_{eff} limitations for each element.

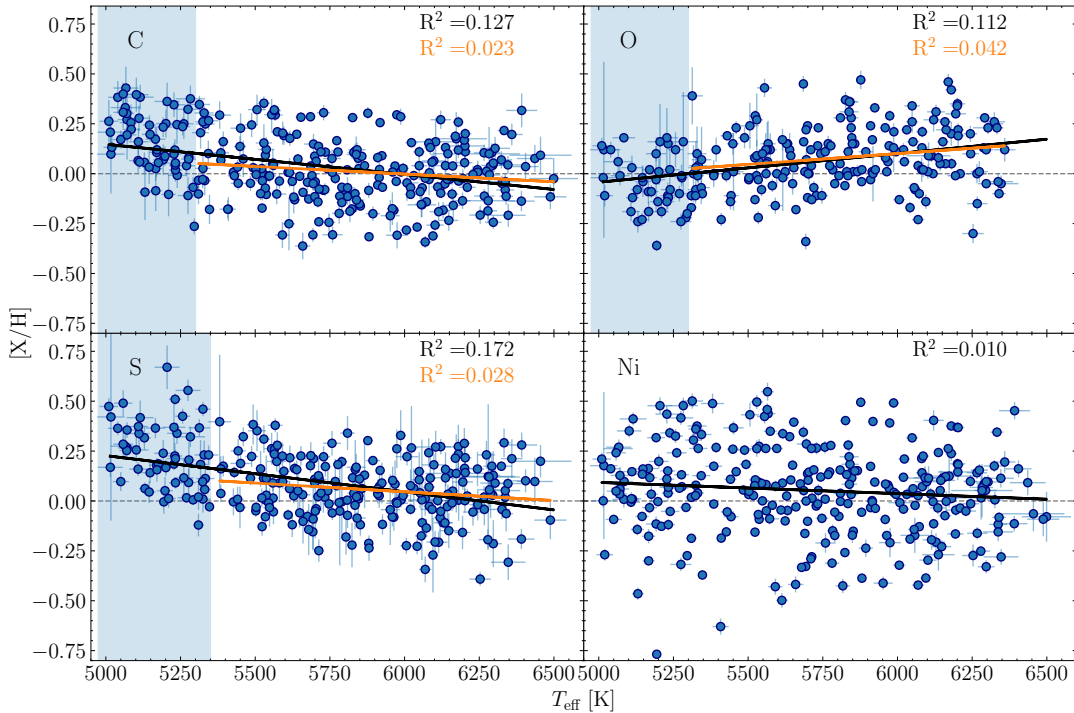


Figure 5. Distribution of $[X/H]$ with T_{eff} . The black line represents the linear fit for the whole sample. The orange line represents the linear fit for the stars outside the blue region. In the upper right corner, we show the R^2 statistics of each OLS regression. The gray dashed line represents $[X/H] = 0.00$ dex.

For the C I lines, close to the C I 5052 Å line there is a strong Fe I line at 5051.6 Å that develops pronounced wings as the effective temperature decreases – blending with the C I line (Luck & Heiter 2006). For the C I 5380 Å line,

²¹ The linear fits mentioned in this and the following sections were performed using the Ordinary Linear Regression (OLS) method from Python *statsmodels* package.

there is an increasing blending with an unknown feature as the effective temperature decreases (Luck & Heiter 2006). According to Luck & Heiter (2006), carbon abundances are unreliable below $T_{\text{eff}} \sim 5500$ K and 5250 K for the C I lines at 5380 Å and 5052 Å, respectively. In this work, we find a good agreement between the abundances of the two carbon lines for stars with $T_{\text{eff}} \geq 5300$ K. By performing a linear regression for the derived abundances for stars with $T_{\text{eff}} \geq 5300$ K, we obtain no trend with $R^2 = 0.023$ (median value for the distribution of the 1000 bootstrapped samples = 0.024), t -value = -2.327 (-2.400), Pearson p -value = 0.021 (0.017) and Spearman p -value = 0.054 (0.047). We also observed no trend between [C/H] and $\log g$, finding $R^2 = 0.006$ (0.006), t -value = -1.213 (-1.140), Pearson p -value = 0.227 (0.238) and Spearman p -value = 0.101 (0.112). Finally, we have 233 carbon determinations for stars with $T_{\text{eff}} \geq 5300$ K.

For the [O I] line at 6300 Å, we notice that below 5300 K the oxygen abundances start to decrease with decreasing T_{eff} . This behavior was also noted by Bertran de Lis et al. (2015) for stars with $T_{\text{eff}} \lesssim 5600$ K for the [O I] 6300 Å line and $T_{\text{eff}} \lesssim 5400$ K for the O I line at 6158 Å but, for the latter, the abundances increase with T_{eff} . By performing a linear regression for the derived abundances for stars with $T_{\text{eff}} \geq 5300$ K, we obtain no trend with $R^2 = 0.042$ (0.044), t -value = 2.828 (2.884), Pearson p -value = 0.005 (0.004) and Spearman p -value = 0.002 (0.002). We also observed no trend between [O/H] and $\log g$, finding $R^2 = 0.018$ (0.019), t -value = -1.820 (-1.863), Pearson p -value = 0.070 (0.064) and Spearman p -value = 0.037 (0.035). Finally, we have 183 oxygen determinations for stars with $T_{\text{eff}} \geq 5300$ K.

For the S I lines, we notice that for $T_{\text{eff}} < 5350$ K the sulfur abundances start to increase with decreasing T_{eff} . This happens because, as the effective temperature decreases, the blending of the S I lines with unknown lines becomes more substantial (e.g., Takeda et al. 2016; Takada-Hidai et al. 2002). Luck (2015) shows a strong trend between [S/Fe] and T_{eff} for stars with $T_{\text{eff}} \sim 5500$ K (see their Figure 6). By performing the linear regression for the derived abundances for stars with $T_{\text{eff}} \geq 5350$ K, we obtain no trend with $R^2 = 0.028$ (0.028), t -value = -2.441 (-2.442), Pearson p -value = 0.016 (0.015) and Spearman p -value = 0.074 (0.077). We also observed no trend between [S/H] and $\log g$, finding $R^2 = 0.019$ (0.020), t -value = 2.007 (2.053), Pearson p -value = 0.046 (0.041) and Spearman p -value = 0.196 (0.172). Finally, we have 212 sulfur determinations for stars with $T_{\text{eff}} \geq 5300$ K.

The Ni I lines do not have restrictions regarding T_{eff} for stars in our sample. Also, we find no trend between [Ni/H] and $\log g$, with $R^2 = 0.006$ (0.006), t -value = -1.300 (-1.306), Pearson p -value = 0.195 (0.88) and Spearman p -value = 0.024 (0.023).

Comparisons with other results from the literature for C (Hinkel et al. 2014; Brewer et al. 2016; Biazzo et al. 2022), O (Brewer et al. 2016; Biazzo et al. 2022), S (Perdigon et al. 2021; Biazzo et al. 2022) and Ni (Brewer et al. 2016; Biazzo et al. 2022) abundances for stars in common with this study are presented in Appendix B.

5. EXOPLANETARY RADII

We determined the radii for the exoplanets in our sample using the stellar radii derived in this study and transit depths from the literature. We found transit depth values for 373 exoplanets in the NASA Exoplanet Archive, totaling 285 host stars. We determined the exoplanetary radii using the inferred stellar radii and the transit depth (ΔF), which is the maximum fraction of stellar flux that is blocked during the transit of the exoplanet, by using the relation from Seager & Mallén-Ornelas (2003):

$$R_{\text{pl}} = 109.1979 \times \sqrt{\Delta F \times 10^{-6}} \times R_{\star}, \quad (7)$$

where R_{pl} is the exoplanetary radius in R_{\oplus} , ΔF is in ppm and R_{\star} is the stellar radius in R_{\odot} . The associated uncertainties were calculated through error propagation.

In our analysis, we only considered the ΔF values of confirmed exoplanets. We obtained the ΔF values from Bordé et al. (2010) (1 exoplanet), Deeg et al. (2010) (1 exoplanet), Mullally et al. (2015) (5 exoplanets), Addison et al. (2016) (1 exoplanet), Barros et al. (2016) (1 exoplanet), Pope et al. (2016) (2 exoplanets), Vanderburg et al. (2016) (5 exoplanets), Christiansen et al. (2017) (2 exoplanets), Stassun et al. (2017) (56 exoplanets), Bouffleur et al. (2018) (1 exoplanet), Livingston et al. (2018) (7 exoplanets), Thompson et al. (2018) (44 exoplanets), Yu et al. (2018) (2 exoplanets), Becker et al. (2019) (1 exoplanet), Kruse et al. (2019) (32 exoplanets), Vanderburg et al. (2019) (3 exoplanets), Bonfanti et al. (2021) (1 exoplanet), Azevedo Silva et al. (2022) (1 exoplanet) and Vivien et al. (2024) (3 exoplanets). For the rest of the 204 exoplanets, we used values ExoFOP²². The exoplanetary radii determined here

²² The Exoplanet Follow-up Observing Program website (https://exofop.ipac.caltech.edu/tess/view_toi.php) is designed to optimize resources and facilitate collaboration in follow-up studies of exoplanet candidates. ExoFOP serves as a repository for project- and community-gathered data by allowing upload and display of data and derived astrophysical parameters. ExoFOP contains stellar parameters from the TESS Input Catalog (TIC), which is served by the Mikulski Archive for Space Telescopes (MAST), and planet parameters from the NASA Exoplanet Archive.

Star	Exoplanet letter	ΔF	R_{pl} (R_{\oplus})	P_{orb} (days)	ΔF and P_{orb} reference
55 Cnc	e	0.03847±0.00042	2.33660±0.03063	0.73655±0.00000	ExoFOP
BD+20 594	b	0.04900±0.00250	2.74110±0.07231	41.68550±0.00300	2
CoRoT-1	b	1.31400±0.00104	15.80940±0.20037	1.50896±0.00001	ExoFOP
CoRoT-4	b	1.38123±0.04210	14.41210±0.24967	9.20165±0.00003	ExoFOP
CoRoT-5	b	1.52427±0.11997	16.50163±0.69285	4.03790±0.00001	ExoFOP

M_{pl} (M_{\oplus})	M_{pl} reference
7.99000±0.32000	1
22.24810±9.53490	2
327.35000±38.14000	3
228.83000±25.43000	4
148.42000±14.93700	5

Table 3. Exoplanetary parameters. Column 1 shows the host-star identification. Column 2 shows the exoplanet letter. Column 3 shows the transit depth (ΔF). Column 4 shows the calculated exoplanetary radii. Column 5 shows the exoplanet orbital period. Column 6 shows the reference for the transit depth and orbital period values of the exoplanet. Column 7 and 8 show the exoplanet mass and its reference.

NOTE—This table is published in its entirety in the machine-readable format. A portion is shown here for guidance regarding its form and content. References: [1] Bourrier et al. (2018), [2] Stassun et al. (2017), [3] Barge et al. (2008), [4] Moutou et al. (2008), [5] Rauer et al. (2009), Bordé et al. (2010), Deeg et al. (2010), Bonomo et al. (2017), Bouffeur et al. (2018), Livingston et al. (2018), Livingston et al. (2024), Kruse et al. (2019), Guenther et al. (2024), Bonomo et al. (2023), Nikolov et al. (2014), Torres et al. (2008), Buchhave et al. (2010), Brown et al. (2012), Chakrabarty & Sengupta (2019), Hartman et al. (2014), Brahm et al. (2016), Jordán et al. (2020), Christiansen et al. (2017), Sozzetti et al. (2021), Polanski et al. (2024), Rosário et al. (2024), Kane et al. (2023), Desidera et al. (2023), Murgas et al. (2022), Dransfield et al. (2022), Egger et al. (2024), Teske et al. (2020), Díaz et al. (2020), Ellis et al. (2021), Bonfanti et al. (2021), Osborn et al. (2021), Zhang et al. (2024), Delrez et al. (2021), Azevedo Silva et al. (2022), Nicholson et al. (2024), Bonfanti et al. (2023), Orell-Miquel et al. (2023), Espinoza et al. (2020), Murphy et al. (2025), Howard et al. (2025), Becker et al. (2019), Vanderburg et al. (2019), Bonfanti et al. (2025), Petigura et al. (2020), Vanderburg et al. (2016), Santerne et al. (2016), Johnson et al. (2016), Grziwa et al. (2016), Lillo-Box et al. (2020), Barragán et al. (2019), Vivien et al. (2024), Lopez et al. (2019), Thygesen et al. (2023), Barros et al. (2016), Pope et al. (2016), Brahm et al. (2018), Palle et al. (2019), Kosiarek et al. (2019), Yu et al. (2018), Eastman et al. (2016), Kuhn et al. (2016), Thompson et al. (2018), Shaw et al. (2025), Borsato et al. (2019), Mullally et al. (2015), Mills et al. (2019), Brinkman et al. (2025), Dalba et al. (2024), Dalba et al. (2021), Jenkins et al. (2020), Gill et al. (2020), Bryant et al. (2020), Smith et al. (2021), Battley et al. (2024), Schulte et al. (2025), Nielsen et al. (2020), Hobson et al. (2023), Hoyer et al. (2021), Hobson et al. (2024), Osborn et al. (2023), Krenn et al. (2024), Rodríguez et al. (2021), Georgieva et al. (2023), Alqasim et al. (2024), Fridlund et al. (2020), Hawthorn et al. (2023), Sha et al. (2021), Armstrong et al. (2023), Otegi et al. (2021), Lockley et al. (2025), Beard et al. (2024), Turtelboom et al. (2022), Tran et al. (2022), Heidari et al. (2025), Sha et al. (2023), Kabáth et al. (2022), Persson et al. (2022), Rice et al. (2023), Yee et al. (2022), Tala Pinto et al. (2025), Brahm et al. (2023), Gill et al. (2024), Šubjak et al. (2025), Frame et al. (2023), Jones et al. (2024), Psaridi et al. (2023), Mantovan et al. (2024b), Hacker et al. (2024), Nabbie et al. (2024), Chaturvedi et al. (2025), Rodríguez Martínez et al. (2025), Castro-González et al. (2024), Ulmer-Moll et al. (2022), Mantovan et al. (2024a), Grieves et al. (2022), Ulmer-Moll et al. (2023), Manni et al. (2025), Eberhardt et al. (2025), Maciejewski et al. (2014), Addison et al. (2019), Gillon et al. (2009), McGruder et al. (2023), Cortés-Zuleta et al. (2020), Anderson et al. (2015), Bouchy et al. (2010), Triaud et al. (2011), Mancini et al. (2016), Mancini et al. (2018), Southworth et al. (2016), Ciceri et al. (2016), Nascimbeni et al. (2023), Hébrard et al. (2013), Southworth et al. (2015), Anderson et al. (2014), Ehrenreich et al. (2020), Noguer et al. (2024), Triaud et al. (2017), Maciejewski et al. (2023), Addison et al. (2016), Hellier et al. (2015), Gillon et al. (2014), Anderson et al. (2017), Wright et al. (2023), Turner et al. (2016), Seidel et al. (2020), Maxted et al. (2016), Hellier et al. (2017), Doyle et al. (2023), Almenara et al. (2022), Hellier et al. (2019), Nielsen et al. (2019), Yee et al. (2025), Crouzet et al. (2012) and Smith (2015).

are listed in Table 3, as well as their orbital period (P_{orb}) and mass (M_{pl}) taken from the NASA Exoplanet Archive. The median uncertainties for the exoplanetary parameters are 2% for ΔF and R_{pl} , 0.0003% for P_{orb} and 12% for M_{pl} .

Comparisons with other results from the literature for exoplanetary radii (Stassun et al. 2017; Petigura et al. 2018a; Kruse et al. 2019; Loaiza-Tacuri et al. 2024) for exoplanets in common with this study are presented in Appendix B.

6. CHEMICAL EVOLUTION OF EXOPLANET HOSTS

In Figure 6, we show the Tinsley-Wallerstein diagram, which is the canonical diagram of the chemical evolution of the Galaxy that presents the distribution of $[X/Fe]$ versus $[Fe/H]$, for our sample of planet hosting stars. In general, our distributions successfully reproduce the shapes expected by the time-delay model (e.g., [Matteucci 2016](#)), in which we see the contribution of different stellar yields, low- (C, Fe, Ni) and high-mass (O, S) stars. Also, our results have significantly lower scatter when compared to non-homogeneous abundances, which is the case for those collected in the Hypatia database. Carbon shows roughly constant solar values, except in the low-metallicity regime for $[Fe/H] \lesssim -0.2$. Oxygen and sulfur show the typical behavior for α -elements, decreasing $[X/Fe]$ with increasing $[Fe/H]$. Finally, nickel closely follows Fe, showing almost a straight line on $[Ni/Fe] = 0.00$. We also show the distributions of the abundance ratios of C/O, C/S and O/S as functions of $[Fe/H]$ in Figure 6. The C/O and C/S ratios show a correlation with the metallicity as expected from the behavior of $[C/Fe]$, $[O/Fe]$, and $[S/Fe]$. The correlation of a modest increase in C/O with metallicity was also seen in [Nissen \(2013\)](#), [Teske et al. \(2014\)](#) and [Delgado Mena et al. \(2021\)](#). The O/S exhibits a tendency towards an anti-correlation with $[Fe/H]$.

Figure 6 also shows the distributions of $[X/Fe]$, C/O, C/S and O/S for stars that have effective temperatures $T_{\text{eff}} < 5300$ K for C and O, and $T_{\text{eff}} < 5350$ K for S (orange filled circles). The addition of these cooler stars generally increases the scatter in the abundance results. We can see that the abundances for the cooler stars fall systematically on the upper parts of the distributions for $[C/Fe]$ and $[S/Fe]$, and also for the C/O ratios. On the contrary, they tend to fall below for the $[O/Fe]$ distribution and are systematically lower for O/S. For C/S, the cooler stars are not systematically distributed. In the following, we will only consider the abundances of stars with $T_{\text{eff}} \geq 5300$ K for C and O and $T_{\text{eff}} \geq 5350$ K for S. For Ni, we will consider all abundances determined since they do not have any limitations regarding effective temperature.

In the bottom right panel of Figure 6 we show the distribution of the $[\alpha/Fe]$ versus $[Fe/H]$ for our sample (stars with $T_{\text{eff}} > 5300$ K for O and $T_{\text{eff}} > 5350$ K for S), where we calculate $[\alpha/Fe]$ as the average of oxygen and sulfur, the two α -elements studied here. Following [Ghezzi et al. \(2026\)](#), we used the separation estimated from Figure 1 of [Adibekyan et al. \(2011\)](#) to divide the host stars sample into low- and high- $[\alpha/Fe]$ sequences, in which *i*) $[\alpha/Fe] = 0.19$ for $[Fe/H] < -0.60$; *ii*) $[\alpha/Fe] = -0.20 \times [Fe/H] + 0.07$ for $-0.06 \leq [Fe/H] \leq 0.00$; *iii*) $[\alpha/Fe] = 0.07$ for $[Fe/H] > 0.00$, noting that in [Adibekyan et al. \(2011\)](#), $[\alpha/Fe]$ is the average of $[Mg/Fe]$, $[Si/Fe]$ and $[Ti/Fe]$. The majority of our sample belongs to the low- $[\alpha]$ sequence population. In total, we have 168 stars with both oxygen and sulfur abundances determined, for which 32 fall on the high- $[\alpha/Fe]$ sequence (corresponding to the chemical thick disk) and 136 on the low- $[\alpha/Fe]$ sequence (thin disk).

7. DISCUSSION: STAR-PLANET CONNECTION

In this section, we investigate relationships between stellar abundances and planetary radii (R_{pl}) determined in this work, as well as orbital periods (P_{orb}) and masses (M_{pl}) taken from the NASA Exoplanet Archive (see Table 3). As mentioned in Section 6, we are only considering abundances of C, O and S for stars with $T_{\text{eff}} \geq 5300$ K, $T_{\text{eff}} \geq 5300$ K and $T_{\text{eff}} \geq 5350$ K, respectively. The exoplanets were divided following the boundaries of [Wilson et al. \(2022\)](#). For planet size classes: (i) Sub-Earths (sE), $R_{\text{pl}} < 1 R_{\oplus}$; (ii) Super-Earths (SE), $1 R_{\oplus} \leq R_{\text{pl}} < 1.9 R_{\oplus}$; (iii) Sub-Neptunes (sN), $1.9 R_{\oplus} \leq R_{\text{pl}} < 4 R_{\oplus}$; (iv) Sub-Saturns (sS), $4 R_{\oplus} \leq R_{\text{pl}} < 8 R_{\oplus}$; (v) Jupiters (J), $8 R_{\oplus} \leq R_{\text{pl}} < 23 R_{\oplus}$. Also, for period classes: (i) hot, $P_{\text{orb}} \leq 10$ days; (ii) warm, $10 < P_{\text{orb}} \leq 100$ days; (iii) cool, $100 < P_{\text{orb}} \leq 300$ days. In total, we have 373 exoplanets with radii and orbital periods determined, 3 sE (hot), 45 SE (35 hot, 9 warm and 1 cool), 124 sN (68 hot, 54 warm and 2 cool), 44 sS (23 hot, 18 warm, 1 cool and 2 with $P_{\text{orb}} > 300$ days) and 157 J (115 hot, 32 warm, 6 cool and 6 with $P_{\text{orb}} > 300$ days). Given the small number of cool exoplanets and exoplanets with $P_{\text{orb}} > 300$ days in our sample, these are not considered in our analysis.

7.1. Single and Multi-planetary Systems

We divided our sample into stars having only one confirmed exoplanet (singles) and those having more than one confirmed exoplanet (multis). In the top row of Figure 7, we show the histograms of the distributions of $\log(R_{\text{pl}}/R_{\oplus})$, $\log(P_{\text{orb}}/\text{day})$ and $\log(M_{\text{pl}}/M_{\oplus})$. We can see from the top left and right panels that small and low-mass exoplanets are more frequent in multi-planetary systems, with median differences (singles – multis) of 9.05 for $\log(R_{\text{pl}}/R_{\oplus})$ and 1.29 for $\log(M_{\text{pl}}/M_{\oplus})$. For $\log(P_{\text{orb}}/\text{day})$ (top middle panel), the median difference between singles and multis is -0.32, meaning that exoplanets in multi-planetary systems tend to have larger orbital distances than exoplanets in single systems. We performed K-S tests between the distributions of $\log(R_{\text{pl}}/R_{\oplus})$, $\log(P_{\text{orb}}/\text{day})$ and $\log(M_{\text{pl}}/M_{\oplus})$ of the two

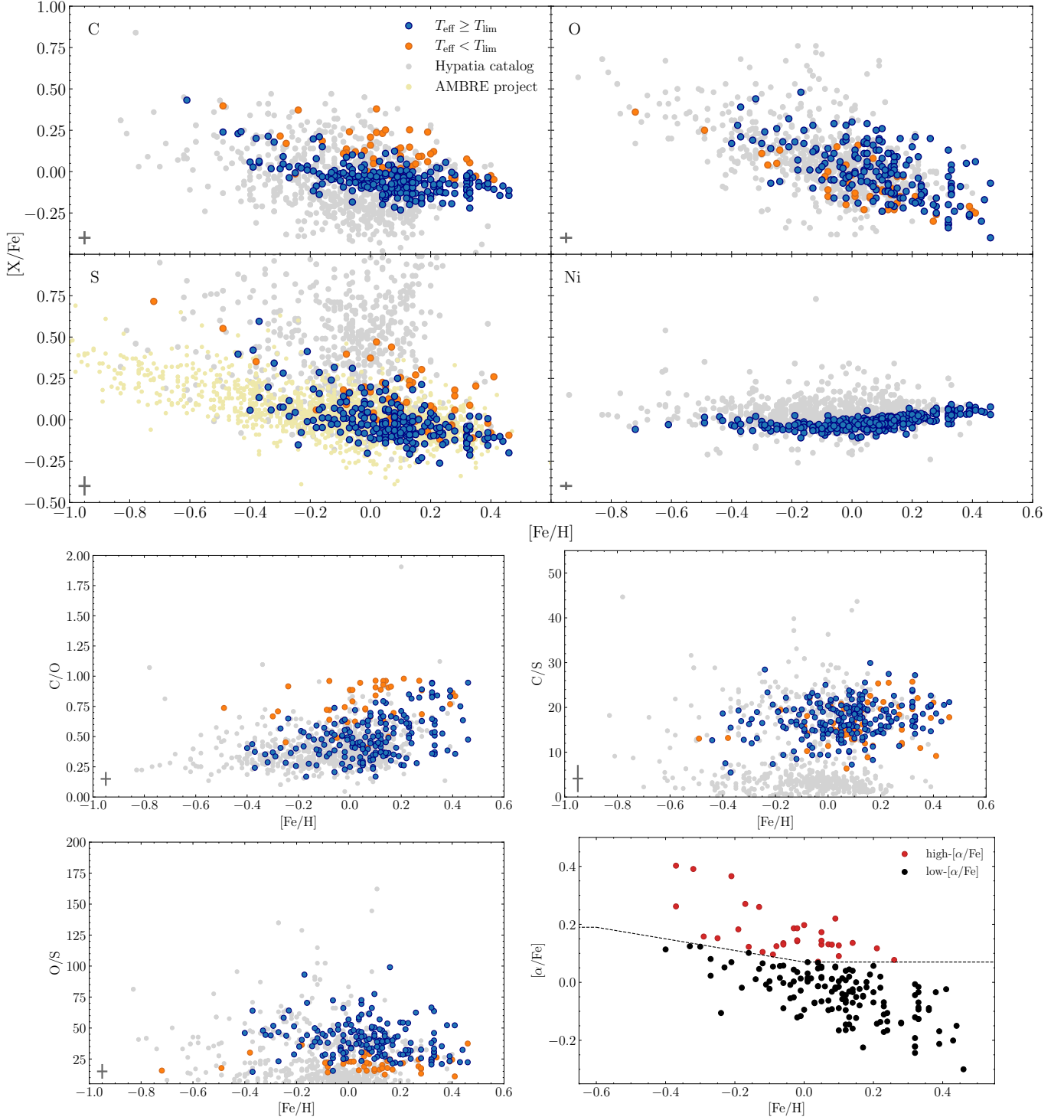


Figure 6. Distribution of $[X/Fe]$ of C (left panel of first row), O (right panel of first row), S (left panel of second row) and Ni (right panel of second row), C/O (left panel of third row), C/S (right panel of third row) and O/S (left panel of last row) ratios and, also, $[\alpha/Fe]$ (right panel of last row) with metallicity. The blue and orange circles represent, respectively, abundances for stars having effective temperatures above and below 5300 K, 5300 K and 5350 K for C, O and S abundances, respectively. The gray and light yellow dots represent the same distributions for the stars in the Hypatia catalog (Hinkel et al. 2014) and in the AMBRE Project (Perdigon et al. 2021), respectively. In the lower left of each panel, we show the median uncertainties in gray. The red and black circles represent, respectively, stars on the high- $[\alpha/Fe]$ and low- $[\alpha/Fe]$ sequences.

groups (singles and multis) and found percentages of $p_{KS} < 0.001$ of 100% for the three of them, i.e., the distributions of radii, orbital periods and masses of exoplanets in single and multi-planetary systems are significantly different. Similar results were found for P_{orb} (e.g., Wright et al. 2009) and R_{pl} (e.g., Muresan et al. 2026). Muresan et al. (2026) also investigated the R_{pl} distributions of singles and multis and found that, when removing the hot Jupiters from their sample, the R_{pl} distributions were indistinguishable. Here, we still find significant differences between the distributions of R_{pl} of singles and multis after removing the hot Jupiters (percentage of $p_{KS} < 0.001$ of 70%).

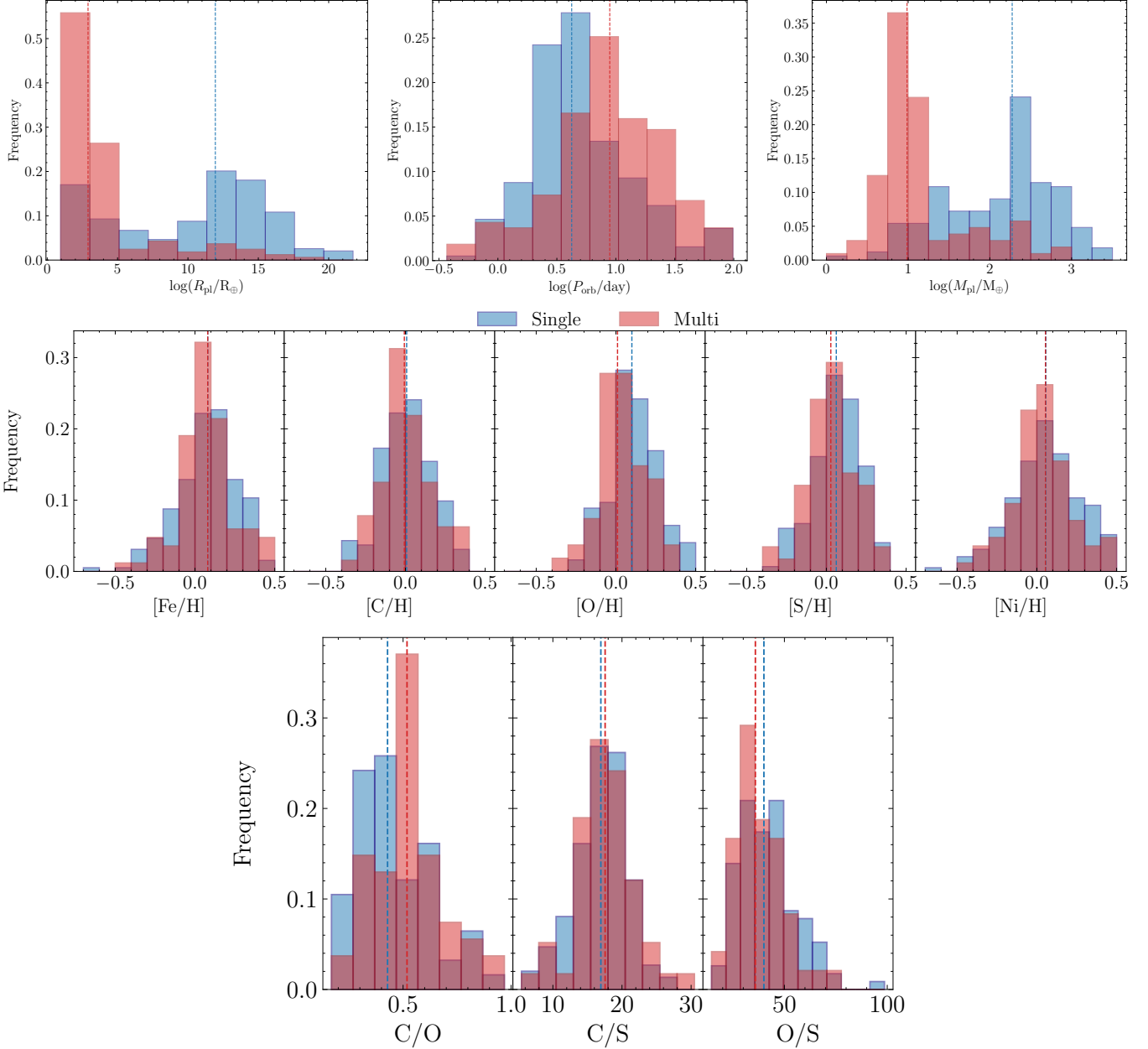


Figure 7. Histograms of $\log(R_{pl}/R_{\oplus})$, $\log(P_{orb}/\text{day})$, $\log(M_{pl}/M_{\oplus})$ (top panels), host star $[X/H]$ (middle panels) and C/O , C/S and O/S abundance ratios (bottom panels). Systems having only one confirmed exoplanet (singles) are shown in blue and systems with more than one confirmed exoplanet in red (multis). The dashed lines indicate the median values of each parameter and the colors match the ones from the histogram bars. The median differences (singles – multis) are 0.00, 0.01, 0.09, 0.03, 0.00, -0.09 ($(\Delta C/O)/(C/O_{\text{singles}}) \sim 21\%$), -0.62 ($\sim 4\%$) and 4.15 ($\sim 10\%$) for $[Fe/H]$, $[C/H]$, $[O/H]$, $[S/H]$, $[Ni/H]$, C/O , C/S and O/S , respectively.

In the middle and bottom panels of Figure 7, we show the distribution of [Fe/H], [C/H], [O/H], [S/H], [Ni/H], C/O, C/S and O/S ratios, we note that the abundance distributions for the singles and multis are very similar for all elements, except for C/O – for which there is an excess of exoplanets in single systems around stars with C/O \lesssim 0.50. These results for [Fe/H] are in agreement with other studies in the literature (e.g., Weiss et al. 2018; Ghezzi et al. 2021; Loaiza-Tacuri et al. 2025). We performed K-S tests between abundance distributions of the two groups (singles and multis) and found percentages of $p_{KS} < 0.001$ of 1%, 0%, 32%, 5%, 3%, 61%, 1% and 9% for [Fe/H], [C/H], [O/H], [S/H], [Ni/H], C/O, C/S and O/S, respectively, i.e., finding significant differences only between the distributions of C/O ratios of stars hosting single and multi-planetary systems.

The scarcity of massive exoplanets in multi-planetary systems might be caused by dynamical instabilities triggered by their presence, which increases collisions, ejections and planet-planet scattering, possibly reducing the number of planets in the system (e.g., Izidoro et al. 2017; Pan et al. 2025). Additionally, massive exoplanets are more frequent around metal-rich stars (e.g., Fischer & Valenti 2005; Sousa et al. 2011; Mortier et al. 2013; Ghezzi et al. 2018), which agrees with what we see in Figures 12 and 7. Pan et al. (2025) performed simulations of multi-planetary systems and classified the final stage of the system as “observed” singles or multis and found that the mean eccentricity and inclination of the planetary orbits increase significantly with host star [Fe/H]. Even though more than one planet might survive from this dynamically hot environment, their final orbits are highly misaligned and these systems might be observed as single-transit – compared to lower metallicity counterparts in which the planets can maintain nearly circular and coplanar orbits (see their Figure 4).

7.2. Distribution of Elemental Abundances of Stars Hosting Small and Giant Exoplanets

Recent studies have shown that the metallicity distribution of stars hosting sub-Saturn or Jupiter-like exoplanets is different from that of stars hosting smaller exoplanets, such as sub-Earths, super-Earths or sub-Neptunes. There is a dependence of giant exoplanet occurrence rate with metallicity, but this is not observed for stars hosting small exoplanets – where a wider range of metallicities is observed for stars hosting super-Earths and sub-Neptunes (e.g., Udry et al. 2006; Ghezzi et al. 2010a; Buchhave et al. 2012; Adibekyan et al. 2012b; Adibekyan 2019; Ghezzi et al. 2021; Ghezzi et al. 2026). However, there is a dependence with metallicity for stars hosting hot small exoplanets (e.g., Petigura et al. 2018b; Wilson et al. 2022; Mulders et al. 2016; Wanderley et al. 2025; Ghezzi et al. 2026). In this study, we divided the stars into two groups based on their exoplanet size classes: stars hosting giant exoplanets (sS or J) or small exoplanets (sE or SE or sN). If a star has at least one giant exoplanet, we define it as a giant exoplanet host. Throughout this and the following analysis, in order to better account for possible fluctuations and to improve the robustness of the statistical analysis, we bootstrapped the two groups 1000 times. We also performed two-sample Kolmogorov–Smirnov test²³ for each bootstrapped sample. For each bootstrapped sample, we calculate its median abundance and K-S p -value (herein, p_{KS}), obtaining a distribution of median abundances and p_{KS} . In this work, we consider a result to be significant if the $p_{KS} < 0.001$.

In the first row of Figure 8, we show that the abundance distributions for hosts of small exoplanets (orange histograms) have lower median values of [X/H] compared to those of giant exoplanets hosts (blue histograms). We can see from the comparison of the histograms that there is an excess of higher abundances in the distributions of giant exoplanet hosts for all elements. The median [X/H] differences (giant - small) are 0.09 dex, 0.04 dex, 0.12 dex, 0.10 dex and 0.09 dex for Fe, C, O, S and Ni, respectively. Similar results were found in the literature for Fe (e.g., Sousa et al. 2011; Wang & Fischer 2015; Ghezzi et al. 2021), Ni (e.g., Adibekyan et al. 2012b; Ghezzi et al. 2026) and, also, Mg (e.g., Adibekyan et al. 2012b) and Si (e.g., Adibekyan et al. 2012b; Ghezzi et al. 2026), which are α -elements as O and S. In the second row of Figure 8, we show the distribution of the abundance ratios of C/O, C/S and O/S²⁴ ratios for the two populations. The distributions of C/O in stars hosting small and large exoplanets are clearly different. The differences in the median abundance ratios (giant - small) for C/O, C/S and O/S are, respectively, -0.08 ((Δ C/O)/(C/O_{giants}) \sim 18%), -1.60 (9%) and 3.01 (7%). Such results suggest that stars hosting only small planets tend to have larger C/O ratios than those hosting at least one giant exoplanet, the differences for the C/S and O/S are not deemed to be significant (higher than \sim 12%).

For the K-S tests, we find $p_{KS} < 0.001$ for a large fraction of the bootstrapped samples for all elements (indicating possible differences in the distribution between giant and small exoplanet hosts), except C. For Fe, O, S, and Ni, we

²³ The two-sample Kolmogorov–Smirnov (K-S) tests were performed using `ks_2samp` function from Python `scipy` package.

²⁴ $X/Y = 10^{A(X)-A(Y)}$, where $A(X)$ and $A(Y)$ are the absolute abundances of X and Y, respectively.

obtained $p_{\text{KS}} < 0.001$ for approximately 65%, 99%, 91% and 68% of the bootstrapped samples, respectively. On the other hand, for C, we obtained $p_{\text{KS}} < 0.001$ for only 16%. For C/O, C/S and O/S, we obtained $p_{\text{KS}} < 0.001$ for 51%, 12% and 7%, respectively.

Finally, we also performed K-S tests for [X/Fe] distributions of small and large exoplanet hosts, but they all returned $p_{\text{KS}} < 0.001$ for a small fraction of the bootstrapped samples (between 2 – 43%) – suggesting that the trends observed for [X/H] are reflecting the correlation between [Fe/H] and R_{pl} (e.g., Ghezzi et al. 2026).

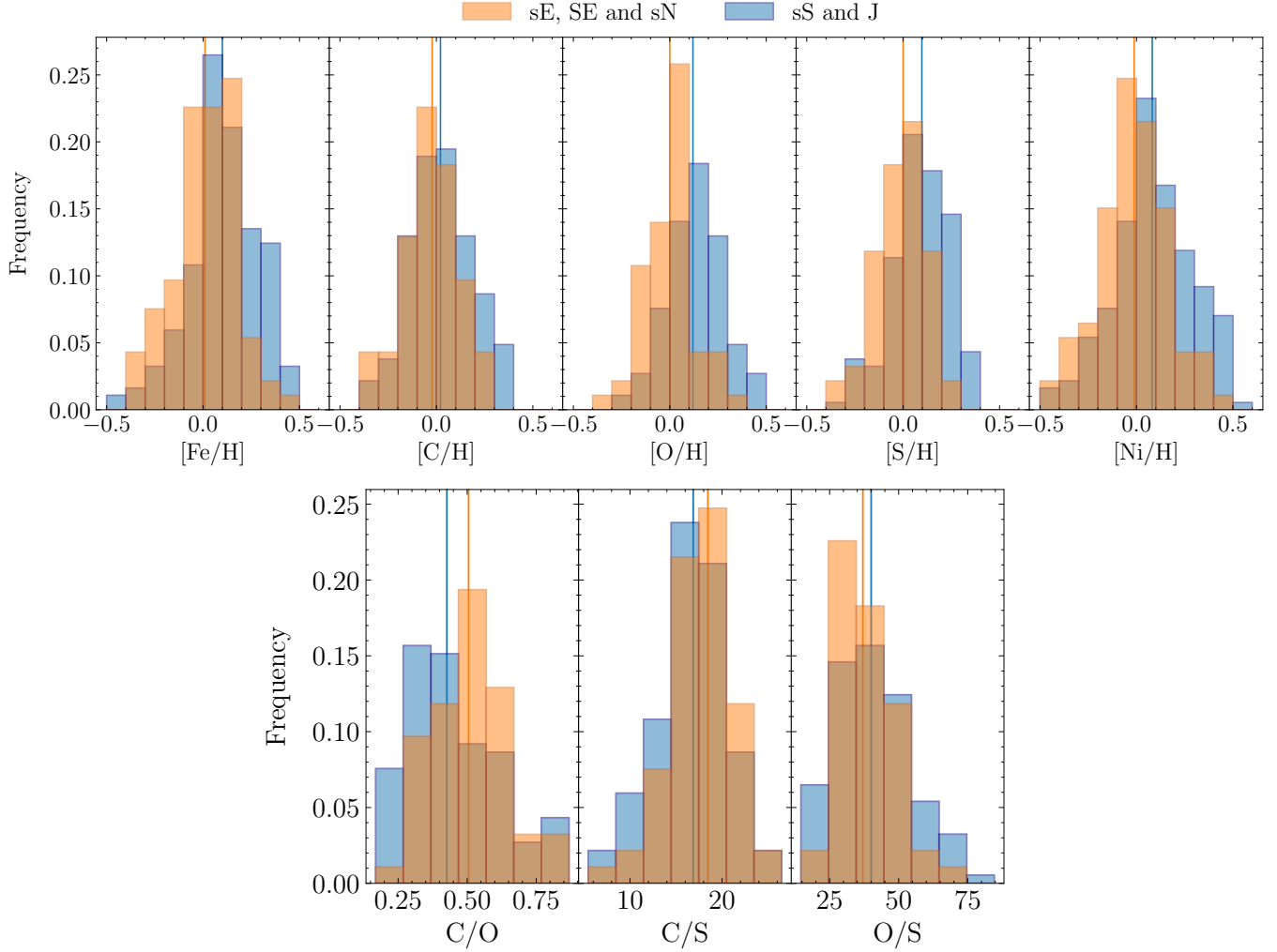


Figure 8. Distribution of elemental abundances for stars hosting giant exoplanets (sS and J, blue bars) and small exoplanets (sE, SE and sN, orange bars). In the first row, we show [Fe/H], [C/H], [O/H], [S/H] and [Ni/H]. In the second row, we show C/O, C/S and O/S. The vertical lines represent the median values for the 1000 bootstrapped samples, with colors matching the respective histograms.

7.3. Trends with Exoplanet Radius

We present the distributions of the abundances of [Fe/H], [C/H], [O/H], [S/H], [Ni/H], and the abundance ratios of C/O, C/S, and O/S as a function of exoplanet radius in the different panels of Figure 9. In our sample, we clearly see a transition where there is a drastic decrease in the amount of exoplanets present approximately between 4 – 8 R_{\oplus} . This gap falls within the sub-Saturn mass range (10 – 100 M_{\oplus}), which is expected to have a lower number of planets within the core accretion formation scenario because planets beyond the ice line grow so rapidly from 10 M_{\oplus} to 100 M_{\oplus} that only a few are left with the intermediate mass range 10 – 100 M_{\oplus} (e.g., Ida & Lin 2004).

For $[\text{Fe}/\text{H}]$ (see top left panel of Figure 9), the distribution of metallicity with exoplanet radius shows a clear tendency for host stars to be more metal-rich as exoplanet radius increases. We performed OLS regressions and obtained a median positive angular coefficient with median t -value=3.50 and $p_{\text{OLS}} < 0.001$ (p -value of the angular coefficient determined by the OLS regression) for 58% of the bootstrapped samples, indicating an overall increase in $[\text{Fe}/\text{H}]$ of the host star with the exoplanet radius (e.g., Buchhave et al. 2012; 2014; Petigura et al. 2018b; Ghezzi et al. 2021; Wilson et al. 2022; Ghezzi et al. 2026). Although the $[\text{Fe}/\text{H}]$ distribution for stars hosting Jupiter exoplanets covers basically our entire range of metallicities, their median $[\text{Fe}/\text{H}]$ is high (0.10 dex). Similarly to Petigura et al. 2018b (see their Figure 3) and Wilson et al. (2022) (see their Figure 9), we find a roughly constant mean $[\text{Fe}/\text{H}]$ up to $\sim 2 R_{\oplus}$ followed by a slight increase towards the Jupiter hosts. We also see an enhancement in $[\text{Fe}/\text{H}]$ for stars hosting sub-Neptunes with larger radii (3 – 4 R_{\oplus}) compared to stars hosting smaller sub-Neptunes (1.9 – 3 R_{\oplus}), which was also observed in the APOGEE Kepler sample analyzed by Wilson et al. (2022). The difference in the median values of the bootstrapped samples between the smaller and larger sub-Neptune hosts is 0.07 dex. However, the K-S tests resulted in a $p_{\text{KS}} < 0.001$ for only 2% of the bootstrapped samples, which indicates that there is not a statistically significant difference between the two distributions of sub-Neptune hosts.

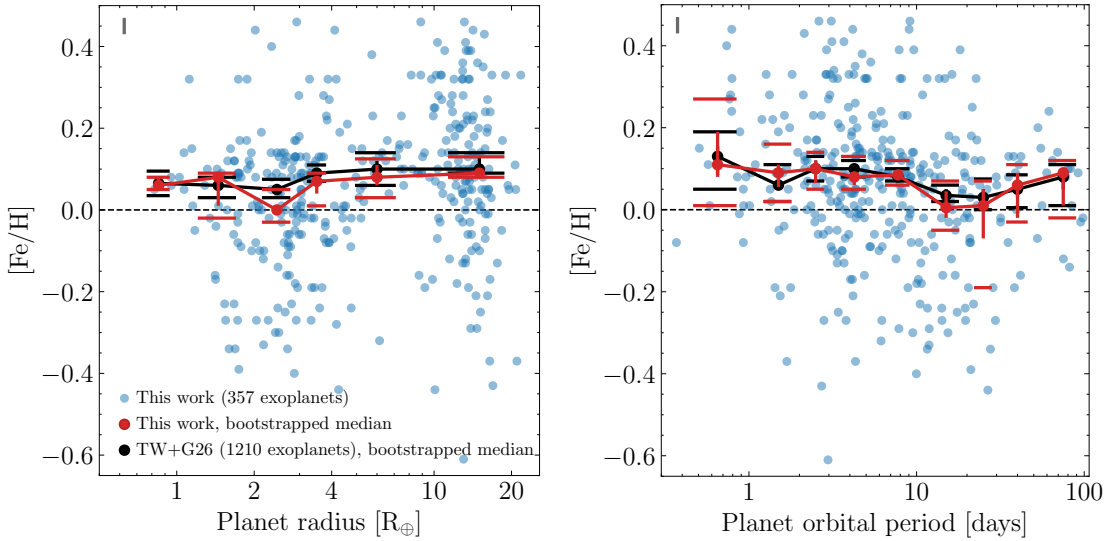


Figure 9. Distribution of $[\text{Fe}/\text{H}]$ of host stars with planet radius (left panel) and planet orbital period (right panel). The blue circles represent the sample from this work. The red circles represent the median abundances of the 1000 bootstrapped samples and their 68% confidence interval range of the distribution (equivalent to a 1σ range for a symmetric distribution) for the bins (0.7, 1], (1, 1.9], (1.9, 3], (3, 4], (4, 8] and (8, 22] R_{\oplus} and (0.3, 1], (1, 2], (2, 3], (3, 5.5], (5.5, 10], (10, 20], (20, 30], (30, 50] and (50, 100] days. The red horizontal bars represent the 95% confidence interval range, equivalent to a 2σ range. The black circles and horizontal bars correspond to the same quantities derived from the combination of the sample from this work and from Ghezzi et al. 2026. The black dashed lines represents the solar values. In the top left of each panel, we show the median uncertainties in gray.

Concerning the distribution of $[\text{X}/\text{H}]$ as a function of exoplanet radius (see top row of Figure 10), we find an overall similar behavior for C, O, S, and Ni, as that for the metallicity ($[\text{Fe}/\text{H}]$) – all elements generally show an increase in the abundances for large exoplanets. In particular, the distribution of the $[\text{Ni}/\text{H}]$ abundances with R_{pl} is quite similar and reminiscent of that of $[\text{Fe}/\text{H}]$, while in the case of $[\text{C}/\text{H}]$, the median abundances show a slight oscillation as R_{pl} increases, which is not seen for $[\text{Fe}/\text{H}]$. The OLS regressions show significant and steeper trends for the α elements versus R_{pl} , i.e., $[\text{O}/\text{H}]$ and $[\text{S}/\text{H}]$ with percentage of $p_{\text{OLS}} < 0.001$ of 99% and 82%, respectively, while the percentages are 9% and 32% for $[\text{C}/\text{H}]$ and $[\text{Ni}/\text{H}]$.

We also evaluated the $[\text{X}/\text{Fe}]$ for our sample, finding generally flat distributions for $[\text{C}/\text{Fe}]$, $[\text{O}/\text{Fe}]$, $[\text{S}/\text{Fe}]$, and $[\text{Ni}/\text{Fe}]$ as a function of R_{pl} for all elements. For $[\text{S}/\text{Fe}]$, Wilson et al. (2022) found a small positive correlation with R_{pl} – a result that was not recovered in our data. For $[\text{C}/\text{Fe}]$, $[\text{O}/\text{Fe}]$, $[\text{S}/\text{Fe}]$ and $[\text{Ni}/\text{Fe}]$, we performed K-S tests dividing the sample between Jupiter and non-Jupiter hosts and obtained $p_{\text{KS}} < 0.001$ for 27%, 11%, 0.5% and 6% of the bootstrapped samples, respectively, meaning no significant differences between the two types of host stars.

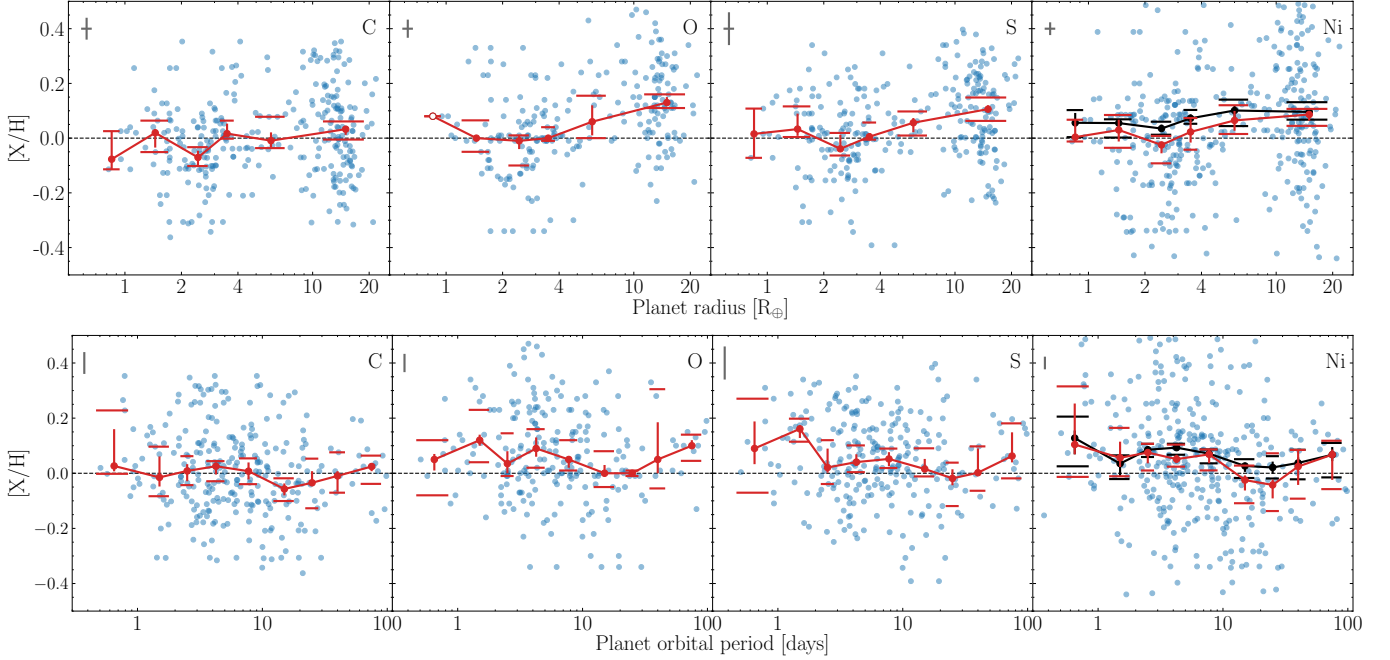


Figure 10. Distribution of $[X/H]$ of host stars with planet radius (top row) and planet orbital period (bottom row). The symbols and lines are the same as in Figure 9.

Moving on to C/O , in the left panel of the first row of Figure 11, we show the distribution of host star C/O versus exoplanet radius, with median C/O ratios per R_{pl} bin shown as filled red circles. The lowest median C/O value is found for Jupiter hosts ($0.43^{+0.02}_{-0.03}$) and this is lower than the solar value of 0.53, while the highest median value of C/O is $0.55^{+0.05}_{-0.01}$ for 3 – 4 R_{\oplus} sub-Neptune hosts ($(\Delta C/O)/(C/O_{3-4 \text{ sub-Neptunes}}) \approx 22\%$). In comparison, 1.9-3 R_{\oplus} sub-Neptune hosts have a median C/O ratio of $0.50^{+0.01}_{-0.02}$ ($\Delta \approx 9\%$). We find similar results using mean and median values from bootstrap and regular mean and median values – they agree that 3 – 4 R_{\oplus} sub-Neptune hosts have the highest C/O ratio and Jupiter hosts have the lowest C/O ratios. We performed K-S tests and found no significant differences between the C/O distributions of 1.9 – 3 R_{\oplus} and 3 – 4 R_{\oplus} sub-Neptune hosts ($p_{KS} < 0.001$ for 11% of the bootstrapped samples). However, we identified significant differences when comparing sub-Neptune hosts to the rest of the sample, Jupiter hosts to the rest of the sample and sub-Neptune hosts to Jupiter hosts, for which we found $p_{KS} < 0.001$ for 63%, 65% and 78% of the bootstrapped samples, respectively.

The distributions of host star C/S and O/S ratios as a function of exoplanet radii are presented in the middle and right panels of the first row of Figure 11. For C/S , the median abundances for all bins are slightly below solar ($C/S_{\odot}=18.62$), except for super-Earth hosts (median $C/S = 19.01^{+0.30}_{-0.40}$) and 3 – 4 R_{\oplus} sub-Neptune hosts (median $C/S = 19.14^{+0.47}_{-0.22}$) which are slightly above, but solar within the uncertainties. C/S ratios generally follow a similar behavior as C/O , in particular for $R_{pl} > 3 R_{\oplus}$. Similarly to C/O , the lowest median C/S value is found for Jupiter hosts ($16.79^{+0.21}_{-0.67}$), and the highest median value for 3 – 4 R_{\oplus} sub-Neptune hosts ($19.14^{+0.47}_{-0.09}$), resulting in a significant $\Delta \approx 12.3\%$. However, at lower R_{pl} , there is a different trend when compared to C/O – the 1 – 1.9 R_{\oplus} bin has a higher median C/S than those of the adjacent bins, while for C/O there is a smooth decline for $R_{pl} \leq 3 R_{\oplus}$. For the K-S tests, we find no statistically significant differences when comparing the distributions of C/S ratios of 3 – 4 R_{\oplus} sub-Neptune hosts with Jupiter hosts, 3 – 4 R_{\oplus} sub-Neptune hosts to the rest of the sample, and Jupiter hosts to the rest of the sample, having $p_{KS} < 0.001$ for 19%, 29% and 15% of the bootstrapped samples.

The median abundance ratios for O/S for all bins are slightly above solar ($O/S_{\odot}=35.48$), except for 3 – 4 R_{pl} sub-Neptune hosts. The lowest median O/S ratio is found for 3 – 4 R_{\oplus} sub-Neptune hosts (median $O/S = 35.04^{+1.40}_{-0.72}$) and the highest median value for sub-Saturn hosts (median $O/S = 43.80^{+0.66}_{-3.90}$) – the behavior is almost reverse of that of the C/O distribution, with differences in median O/S ratios corresponding to about $(\Delta O/S)/(O/S_{\text{sub-Saturn}}) \sim 20\%$. For the K-S tests, we find no statistically significant differences when comparing the distribution of O/S ratio of 3 – 4 R_{\oplus} sub-Neptune hosts with sub-Saturn hosts, 3 – 4 R_{\oplus} sub-Neptune hosts to the rest of the sample, or sub-Saturn hosts to the rest of the sample, having $p_{KS} < 0.001$ for 5%, 4% and 5% of the bootstrapped samples.

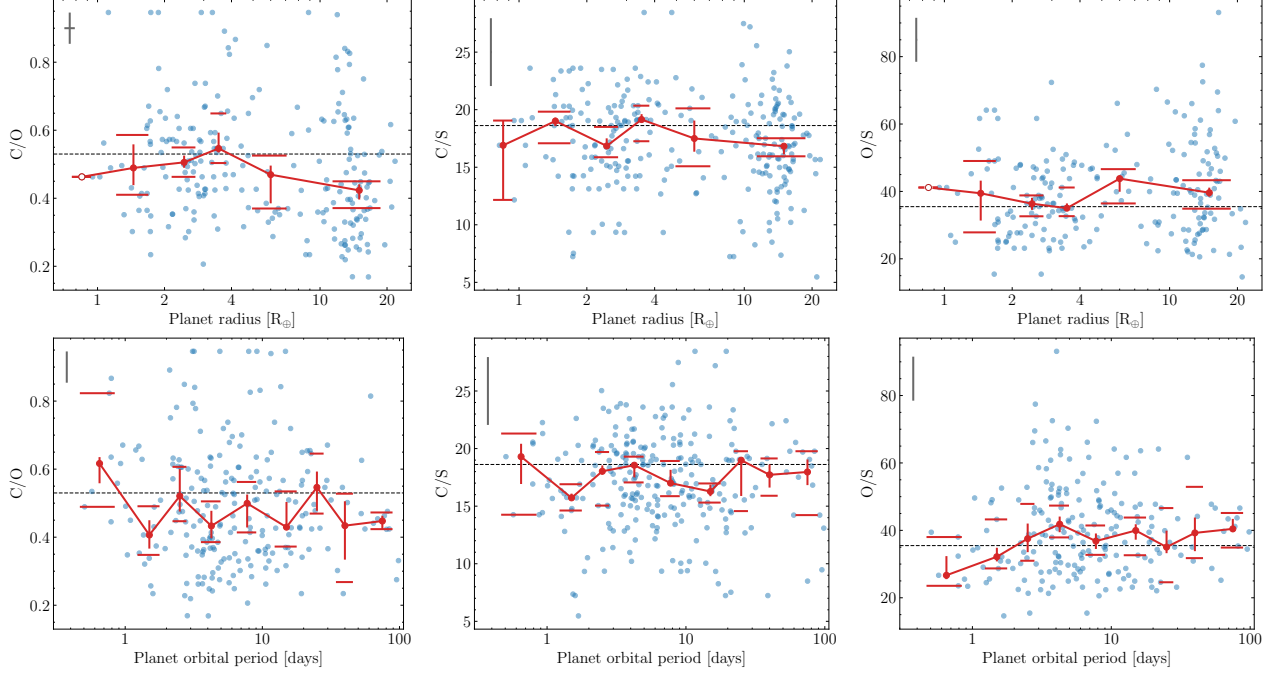


Figure 11. Distribution of C/O (left column), C/S (middle column) and O/S (right column) of host stars with planet radius (top row) and planet orbital period (bottom row). The symbols and lines are the same as in Figure 9.

7.4. Trends with Exoplanet Orbital Period

The distribution of host star $[\text{Fe}/\text{H}]$ as a function of exoplanet orbital period for our sample is shown in the right panel of Figure 9. Before we discuss these results, we point out that, unlike the previous studies that investigated trends of host star metallicities with exoplanet orbital periods (e.g., Mulders et al. 2016; Petigura et al. 2018b; Wilson et al. 2018), our sample of FGK stars has a significant number of large ($R_{\text{pl}} \geq 4 R_{\oplus}$) exoplanets (151 exoplanets, or, $\sim 42\%$ of our sample). One important result in the mentioned studies was that stars hosting hot exoplanets with orbital periods shorter than roughly 8 – 10 days tend to have larger metallicities when compared to exoplanets with longer orbital periods, and that this was true for samples of large and small exoplanets (Mulders et al. 2016). Metallicity enhancements for stars hosting short period exoplanets have also been found for M dwarfs, but, in that case, the exoplanet orbital period threshold was much shorter (~ 4 days; Wanderley et al. 2025).

In our sample, 75% of the hot exoplanets orbit stars with $[\text{Fe}/\text{H}] \geq 0.00$, for which approximately half are hot Jupiters (48%). We already know from the planet-metallicity correlation that giant exoplanets are more frequently found around metal-rich stars (e.g., Fischer & Valenti 2005; Mortier et al. 2013; Ghezzi et al. 2018). Elevated stellar metallicity change disk density profiles by increasing the dust-to-gas ratio, possibly triggering or amplifying certain migration mechanisms (e.g., Mulders et al. 2016; Petigura et al. 2018b; Dawson & Murray-Clay 2013). Since the origin of hot Jupiters is commonly associated with the migration of these giant planets to close-in orbits after their formation at higher orbital distances (e.g., Ida & Lin 2008; Dawson & Murray-Clay 2013; Dawson & Johnson 2018) – although *in situ* formation still remains under debate (e.g., Boley et al. 2016; Mathur & Becker 2025) – the higher frequency of close-in exoplanets around metal rich stars observed here and in many works (e.g., Mulders et al. 2016; Petigura et al. 2018b; Wilson et al. 2018) can be caused by the influence of the stellar metallicity in the dynamical instabilities of the proto-planetary disk.

The median $[\text{Fe}/\text{H}]$ results in this study (shown as red circles in Figure 9) stay moderately flat with increasing P_{orb} until $\sim 8 - 10$ days, having a median $[\text{Fe}/\text{H}]$ of 0.09 dex, and are lower for orbital periods between $\sim 10 - 30$ days, with a median metallicity of 0.01 dex. We performed K-S tests by dividing the sample at orbital periods ranging from 8 to 11 days, using a step size of 0.1 day, and found percentages of $p_{\text{KS}} < 0.001$ higher than 50% for transitions placed anywhere between 8.3 – 10.3 days. However, a larger median difference of 0.08 dex is found when placing the orbital period transition at 9.8 days, which is also where we obtained a larger percentage of 71% of the bootstrapped samples

with $p_{KS} < 0.001$ for the K-S tests. Furthermore, by testing the transition at 11 days, we obtained $p_{KS} < 0.001$ for 39% of the bootstrapped samples and this fraction only decreases with increasing orbital period transition.

Interestingly, we find that for larger orbital periods, between 30 – 100 days, there is an increase in the median [Fe/H] of host stars. It is clear from our results that the median iron abundance does not keep declining for larger orbital periods, and it is possible that this uptrend had not been seen in previous studies because our sample has a larger number of large planets at large orbital periods. We performed OLS regressions to the [Fe/H]- P_{orb} data and obtained a median negative angular coefficient with median t -value=-1.54 and $p_{OLS} < 0.001$ for 8% of the bootstrapped samples. However, if we remove the 30 – 50 and 50 – 100 days orbital period bins, the OLS regressions result in a median negative angular coefficient with median t -value=-4.35 and $p_{OLS} < 0.001$ for 82% of the bootstrapped samples. Thus, we do recover the trend in which we see an overall decrease in the [Fe/H] of the host star with increasing planet orbital period (e.g., Mulders et al. 2016; Petigura et al. 2018b; Wilson et al. 2018; Wilson et al. 2022), but for $P_{orb} \leq 30$ days.

To further investigate the uptrend with orbital period, we combined our exoplanet sample with the Kepler sample from Ghezzi et al. (2026), whose methodology for the determination of host star parameters and iron abundances is the exact same as in this study – making this a homogeneous sample. The combined sample has 1210 exoplanets and their median metallicities as a function of exoplanet orbital periods are shown as black symbols in Figure 9. The results for this combined sample confirm that the metallicities do not decline past $P_{orb} \sim 30$ days, having $p_{OLS} < 0.001$ for 43% and $|t_{OLS}| > 3$ for 32% of the bootstrapped samples for the whole P_{orb} range. We also segregated the combined sample into subsamples having small ($R_{pl} < 4 R_{\oplus}$) and large exoplanets ($R_{pl} \geq 4 R_{\oplus}$) and we find similar uptrends in metallicity for exoplanets with $P_{orb} > 30$ days for both the small and large exoplanet regimes, , having $p_{OLS} < 0.001$ for 19% and $|t_{OLS}| > 3$ for 13% of the bootstrapped samples for the whole P_{orb} range of small exoplanets and $p_{OLS} < 0.001$ for 23% and $|t_{OLS}| > 3$ for 17% for the giant exoplanets.

The distributions of [X/H] for the studied elements with exoplanet orbital period are shown in the bottom row of Figure 10. We can see that, overall, the behavior of the elemental abundances is similar for all elements. For completeness, we also investigated the abundance differences for the samples of stars hosting hot ($P_{orb} \leq 10$ days) versus warm_(10,30) ($10 < P_{orb} \leq 30$ days) exoplanets for the elements [C/H], [O/H], [S/H], and [Ni/H], as well as the C/O, C/S, and O/S ratios. The median abundance differences for “hot minus warm_(10,30)” are found in Table 4. For the entire sample, besides [Fe/H], we find a significant abundance difference ($\Delta > 0.05$) only for the element [Ni/H]. When segregating the sample into stars hosting only small exoplanets (sE, SE and/or sN), we find significant abundance differences between hot and warm_(10,30) for all elements. For stars hosting at least one giant exoplanet (sS and/or J), we only see significant differences for [Fe/H], [C/H] and [Ni/H]. For systems having at least one sub-Neptune, we find significant differences for [Fe/H], [S/H] and [Ni/H] – elements that are (Fe and Ni) or behave (S) as refractories in the protoplanetary disk. For systems having at least one sub-Saturn, we find significant differences for all elements. However, for systems having at least one Jupiter, there are no significant differences between hot and warm_(10,30). Regarding the abundance ratios, we see significant differences ($(\Delta/X/Y)/(X/Y_{hot}) > 1 - 10^{0.05} \approx 12\%$) for C/O and O/S for stars hosting only small planets, O/S for stars hosting at least one sub-Neptune and C/S for stars hosting at least one sub-Saturn. Finally, we performed K-S tests between hot and warm_(10,30) hosts and obtained high percentages of $p_{KS} < 0.001$ for the bootstrapped samples only for [Fe/H] and [Ni/H] for the entire sample, [Fe/H], [C/H] and [Ni/H] for stars hosting only small planets, [Fe/H] and [Ni/H] for stars hosting at least one sub-Neptune and [Fe/H], [C/H] and [Ni/H] for stars hosting at least one sub-Saturn.

We also investigated the distribution of [X/Fe] with exoplanet orbital period for all elements and found no trends over the entire range of P_{orb} , with $p_{OLS} < 0.001$ for 3%, 1%, 3% and 0% of the OLS regressions of the bootstrapped samples for [C/Fe], [O/Fe], [S/Fe] and [Ni/Fe], respectively – showing there are no significant trends. For [S/Fe], Wilson et al. (2022) found a significant positive correlation (p -value= 1.2×10^{-5}), which we did not recover – as the median [S/Fe] stays mostly constant.

In the bottom row of Figure 11, we show the distributions of host star C/O, C/S and O/S with orbital period. Starting with C/O, the median C/O abundance ratios show a slight oscillation as P_{orb} increases, but stay moderately flat with values below solar, except for stars hosting exoplanets with $P_{orb} \leq 1$ day, which have the highest median C/O value of $0.62^{+0.02}_{-0.06}$. The median C/O for host stars with exoplanets having $20 < P_{orb} \leq 30$ days ($0.55^{+0.05}_{-0.07}$) is basically solar. We also see a generally flat distribution of median C/S as a function of exoplanet orbital period. The median values of C/S are fairly close or below the solar value (18.62). Here again, the highest median C/S value is found for stars hosting exoplanets $P_{orb} \leq 1$ day ($19.29^{+1.12}_{-2.37}$), but this bin has a very small number of exoplanets (9 exoplanets). For O/S, there is a clear increase in the median O/S ratios versus exoplanet orbital period for P_{orb} up to

Type	N_{pl} (hot, warm _(10,30))	$\Delta[\text{Fe}/\text{H}]$	$\Delta[\text{C}/\text{H}]$	$\Delta[\text{O}/\text{H}]$	$\Delta[\text{S}/\text{H}]$	$\Delta[\text{Ni}/\text{H}]$	% $p_{\text{KS}} < 0.001$ (Fe, C, O, S, Ni)
All	244, 47	$0.11^{+0.06}_{-0.01}$	$0.05^{+0.05}_{-0.01}$	$0.05^{+0.04}_{-0.03}$	$0.03^{+0.06}_{-0.03}$	$0.11^{+0.03}_{-0.05}$	83, 24, 6, 11, 79
sE/SE/sN	89, 20	$0.22^{+0.06}_{-0.04}$	$0.13^{+0.03}_{-0.07}$	$0.06^{+0.06}_{-0.01}$	$0.11^{+0.09}_{-0.05}$	$0.24^{+0.06}_{-0.06}$	95, 66, 6, 36, 96
sS/J	138, 34	$0.07^{+0.04}_{-0.03}$	$0.08^{+0.03}_{-0.02}$	$0.04^{+0.05}_{-0.05}$	$0.03^{+0.04}_{-0.05}$	$0.09^{+0.03}_{-0.03}$	43, 28, 9, 4, 47
sN	68, 23	$0.09^{+0.03}_{-0.06}$	$0.04^{+0.10}_{-0.05}$	$0.04^{+0.04}_{-0.06}$	$0.06^{+0.06}_{-0.08}$	$0.10^{+0.06}_{-0.05}$	60, 17, 10, 21, 52
sS	23, 14	$0.16^{+0.02}_{-0.04}$	$0.13^{+0.02}_{-0.04}$	$0.14^{+0.06}_{-0.07}$	$0.08^{+0.06}_{-0.07}$	$0.17^{+0.03}_{-0.07}$	91, 94, 17, 25, 90
J	115, 20	$0.01^{+0.05}_{-0.04}$	$0.01^{+0.09}_{-0.05}$	$0.01^{+0.09}_{-0.06}$	$-0.01^{+0.07}_{-0.04}$	$0.04^{+0.09}_{-0.03}$	2, 3, 0, 3, 4

$\Delta\text{C}/\text{O}$	$\Delta\text{C}/\text{S}$	$\Delta\text{O}/\text{S}$	% $p_{\text{KS}} < 0.001$ (C/O, C/S, O/S)
$0.05^{+0.05}_{-0.03}$	$0.47^{+0.62}_{-0.72}$	$-3.40^{+2.77}_{-2.64}$	4,6,11
$0.13^{+0.10}_{-0.05}$	$1.89^{+0.53}_{-0.63}$	$-8.53^{+2.84}_{-2.12}$	29,17,19
$-0.02^{+0.06}_{-0.02}$	$1.27^{+1.03}_{-0.92}$	$1.22^{+2.99}_{-2.82}$	2,20,3
$0.03^{+0.08}_{-0.10}$	$0.82^{+1.21}_{-1.28}$	$-7.91^{+3.43}_{-10.70}$	6,5,22
$-0.03^{+0.16}_{-0.12}$	$3.30^{+2.31}_{-1.39}$	$0.40^{+4.07}_{-10.58}$	5,12,2
$-0.02^{+0.20}_{-0.10}$	$1.04^{+1.24}_{-1.40}$	$1.76^{+2.91}_{-6.65}$	3,8,4

Table 4. Median [Fe/H], [C/H], [O/H], [S/H], [Ni/H], C/O, C/S, and O/S abundance differences between (hot - warm_(10,30) days) for the samples of stars hosting exoplanets. “All” corresponds to the entire sample, sE/SE/sN to stars hosting only small exoplanets, sS/J to stars hosting at least one giant exoplanet and, sN, sS and J to stars hosting at least one sub-Neptune, sub-Saturn and Jupiter, respectively. The last column presents the percentage of bootstrapped samples with $p_{\text{KS}} < 0.001$ for the K-S tests for the distributions of [Fe/H], [C/H], [O/H], [S/H], [Ni/H], and C/O, C/S and O/S.

5.5 days. This is followed by a slight oscillation as P_{orb} increases. All median O/S values having $P_{\text{orb}} > 5.5$ days are above or near solar (34.48). The lowest value of $26.67^{+5.69}_{-1.14}$ is found for stars hosting exoplanets with $P_{\text{orb}} \leq 1$ day – unlike C/O and C/S distributions for which this bin had the highest median value.

7.5. Trends with Exoplanet Mass

Examining planetary masses adds another fundamental property with which to probe possible correlations with stellar chemistry. The masses of the exoplanets in this study come from non-homogeneous literature sources (see Table 3). Although we have masses determined for 270 exoplanets, here, we will consider only exoplanets with masses having uncertainties below 20%, resulting in a sample with 199 exoplanets. Figure 12 shows stellar [X/H] and abundance ratios versus exoplanetary mass. From left to right, we show Fe and Ni in the first row, C, O and S in the second row and C/O, C/S and O/S in the last row. In each panel, the solar ratios are indicated by the black horizontal dashed lines and the masses of Jupiter, Saturn, Uranus and Neptune are shown as the red, yellow, pink and green hexagons, respectively. We note a gap in all of the panels, dividing the distributions into two mass groups. These groups are separated by a gap covering a mass range of $\sim 20 - 100 M_{\oplus}$ ($\log(M_{\text{pl}}/M_{\oplus}) \sim 1.3 - 2$). This mass range is roughly where the sub-Saturn desert is located (e.g., *Ida & Lin 2004*). The “mass gap” is most accentuated in [O/H], [S/H], C/O and O/S, while [Fe/H], [Ni/H], [C/H] and C/S do not yield such a clean segregation. However, this might be associated with the reduced number of available [O/H] and [S/H] abundances for planet-hosting stars compared to [Fe/H] and [Ni/H].

To identify if these gaps are statistically significant and their locations, we performed K–S tests by dividing the sample at $\log(M_{\text{pl}}/M_{\oplus})$ ranging from 1.3 to 2.3, using a step size of 0.1. All the tests pointed to a gap at ~ 1.4 ($\sim 25 M_{\oplus}$) with a percentage of $p_{\text{KS}} < 0.001$ of 94%, 55%, 100%, 99% and 86% for [Fe/H], [C/H], [O/H], [S/H] and [Ni/H], respectively, and 74%, 42% and 22% for C/O, C/S and O/S. These results corroborate with the existence of an assumed vertical gap (zero slope) for all elements and abundance ratios, except for [C/H], C/S and O/S. The previous work by *Delgado Mena et al. (2021)* did not find a significant difference between the distribution of the C/O ratios of stars hosting exoplanets with M_{pl} below and above $30 M_{\oplus}$. In their work, *Delgado Mena et al. (2021)* used the oxygen results from *Bertran de Lis et al. (2015)* for both the 6158 Å O I line and the 6300 Å [O I] line to obtain C/O ratios. To further investigate the signature in the C/O ratios, we combined our sample with their C/O₆₃₀₀ sample, resulting in a total sample of 121 host stars, and found a percentage of $p_{\text{KS}} < 0.001$ of 68% for the K-S tests between

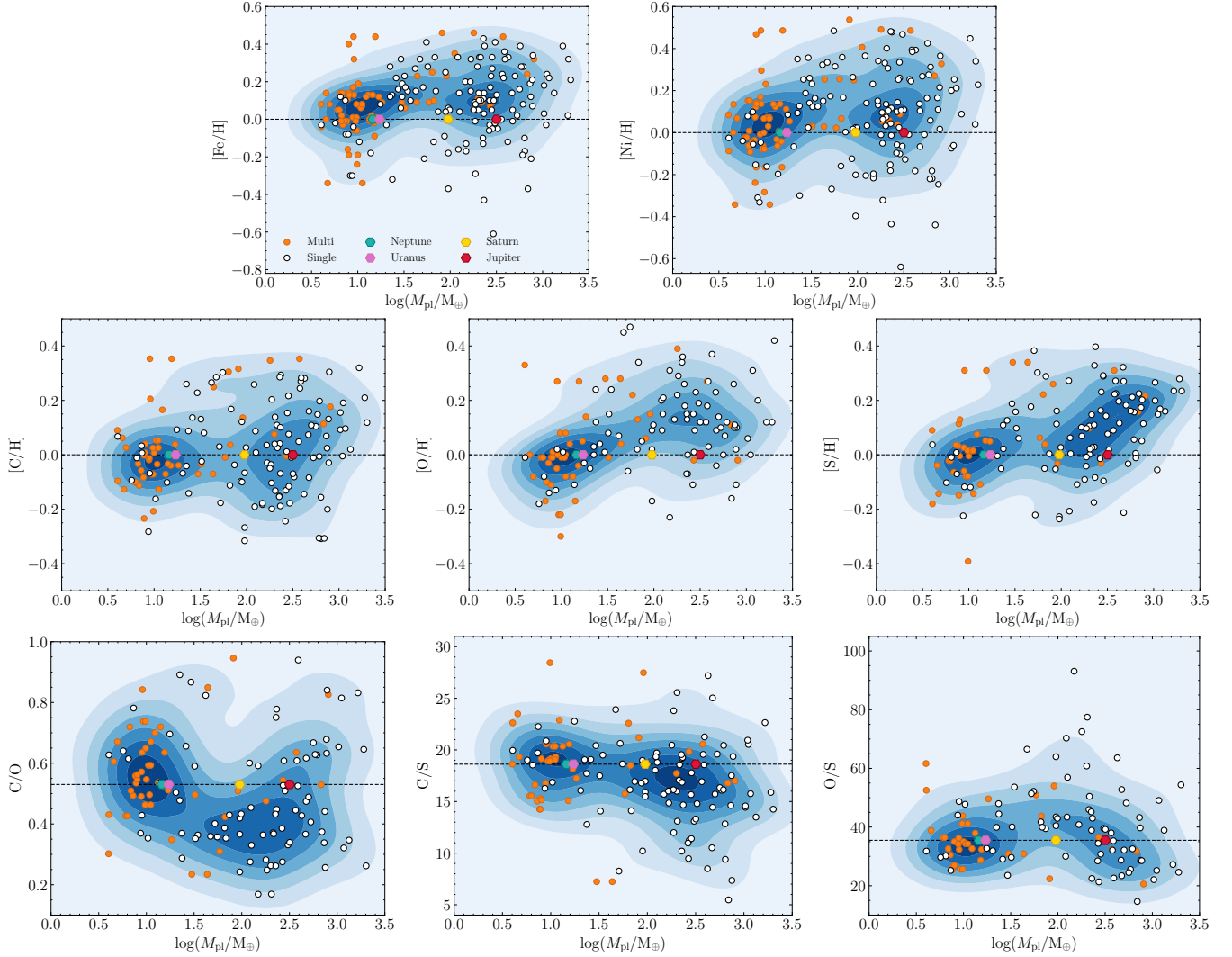


Figure 12. Distribution of $[X/H]$ and abundance ratios of host stars as a function of exoplanet mass. In the first row, we show $[Fe/H]$ (left panel) and $[Ni/H]$ (right panel). In the second row, $[C/H]$ (left panel), $[O/H]$ (middle panel) and $[S/H]$ (right panel). In the last row, C/O (left panel), C/S (middle panel), and O/S (left panel) ratios. Stars having only one exoplanet confirmed are presented in white circles (single) and, having more than one exoplanet confirmed, in orange circles (multi). Jupiter, Saturn, Uranus and Neptune are represented by the red, yellow, pink and green hexagons, respectively. The blue heat map represents the distribution of all exoplanets, independently of their status as single or multi. The black dashed lines represent the solar values.

the distribution of C/O ratios of stars hosting exoplanets with M_{pl} below and above $30 M_{\oplus}$ – still finding a significant difference.

We note that stars hosting low-mass exoplanets ($\log(M_{pl}/M_{\oplus}) < 1.4$) are closely clustered around solar abundances with median abundances of 0.04, -0.02, -0.01, 0.00 and 0.01 for $[Fe/H]$, $[C/H]$, $[O/H]$, $[S/H]$, $[Ni/H]$, respectively, and 0.56, 19.06 and 34.32 for C/O , C/S and O/S , while massive exoplanet hosts are, in general, more scattered. There is a small cluster of exoplanets around 2.4 and $[X/H] \sim 0.08$ in the middle of $[Fe/H]$ and $[Ni/H]$ distributions but they represent a small fraction of massive exoplanets. The median abundances of massive exoplanet ($\log(M_{pl}/M_{\oplus}) \geq 1.4$) hosts are 0.13, 0.04, 0.12, 0.12 and 0.12, and 0.44, 16.79 and 30.40, i.e., iron-peak and α -elements above solar values, C/O and C/S below solar values and $[C/H]$ and O/S around solar value.

In Figure 12, we see that massive exoplanets are preferentially found around oxygen-enriched stars, whereas this trend is not observed for carbon abundances. This may point to the greater importance of the H_2O ice line compared to the CO and CO_2 ice lines in the formation of giant exoplanet cores within the core-accretion scenario. Since giant

planet core growth must occur on a short timescale, before disk dispersal, formation at smaller orbital distances favors more frequent collisions and, consequently, more efficient accretion of solid material (e.g., [Drażkowska & Alibert 2017](#); [Leemker et al. 2026](#)). In this context, the H₂O ice line is located significantly closer to the star than the CO and CO₂ ice lines. A similar trend is observed for sulfur abundances, but this may be related to the fact that both O and S are α -elements. To test this hypothesis, it is necessary to determine the abundances of additional α -elements (e.g., Mg, and Si) to assess whether this pattern holds. [Robinson et al. \(2006\)](#), using the SPOCS data of [Fischer & Valenti \(2005\)](#), observed that stars hosting giant exoplanets have enhanced [Si/Fe] and [Ni/Fe] abundances compared to field stars with the same [Fe/H], which may arise primarily from the oxygen and silicon correlation. For the Kepler sample, [Ghezzi et al. \(2026\)](#) found statistically significant differences between the [X/H] abundances of stars hosting only small exoplanets and only giant exoplanets for the α -elements Si and Ti, but not for Mg and Ca. Finally, for the HARPS GTO sample, [Costa Silva et al. \(2020\)](#) observed a higher frequency of exoplanets around stars with solar [S/Fe] ($-0.10 < [S/Fe] < 0.10$). This is also found in our work, in which we have a total of 86 exoplanets around stars with solar [S/Fe] compared to 51 exoplanets around stars with non-solar [S/Fe].

We performed OLS regressions and obtained percentages of $p_{\text{OLS}} < 0.001$ of 30%, 7%, 90%, 95%, 23%, 2%, 36% and 0% for [Fe/H], [C/H], [O/H], [S/H], [Ni/H], C/O, C/S, and O/S, respectively, and positive angular coefficients for all elements and negative for all abundance ratios. Additionally, to account for different detection biases, we restrained our sample to exoplanets detected through planetary transit and having mass uncertainties below 20% and found percentages of $p_{\text{OLS}} < 0.001$ of 88% and 68% for [O/H] and [S/H], respectively, and below 14% for the other abundances. These results are in agreement with what we found for R_{pl} , in which α -elements have steeper trends. We also investigated the distribution of [X/Fe] with $\log(M_{\text{pl}}/M_{\oplus})$ and found no trends for all elements, with percentages of $p_{\text{OLS}} < 0.001$ below 28% for all elements.

We divided our sample into hot ($P_{\text{orb}} \leq 10$ days) and warm exoplanets ($10 < P_{\text{orb}} \leq 100$) and performed OLS regressions. For the hot exoplanets, we found no trends for all abundances (percentages of $p_{\text{OLS}} < 0.001$ below 45%). For the warm exoplanets, we found significant trends with [O/H] and [S/H] (percentages of $p_{\text{OLS}} < 0.001$ of 56% and 83%, respectively), while the percentages were below 42% for the other abundances. Considering that the hot exoplanets did not form in their current orbits, but rather migrated closer to the host star (e.g., [Ida & Lin 2008](#); [Dawson & Murray-Clay 2013](#)), the absence of trends between the α -elements and $\log(M_{\text{pl}}/M_{\oplus})$ for hot exoplanets may indicate that these trends are possibly associated to the exoplanets actual formation locations, assuming that most of the warm exoplanets preserve their orbital distances.

Regarding the distribution the planets of the Solar system for [X/H], we note that Uranus (pink hexagon) and Neptune (green hexagon) fall, for all elements, close to the border of the over-density of low-mass exoplanets. Saturn (yellow hexagon) falls near the lower-mass border of the over-density of massive exoplanets for all elements, except [O/H]. Jupiter (red hexagon) falls at the intermediate-mass border of the over-density of giant exoplanets for [Fe/H], [Ni/H] and [S/H], in the middle for [C/H] and outside for [O/H].

Focusing on the C/O ratios, [Figure 12](#) suggests that the underlying stellar C/O ratio plays a role in the position of the mass gap. The gap is not as pronounced at lower values of C/O ($\lesssim 0.35$), with the lower-mass limit of gas giant planets (which form by runaway gas accretion) increasing with larger C/O ratios. The increasing low-mass limit for gas giant planets may point to enhanced C/O ratios driving a more efficient (or faster) build-up of giant planet solid cores to the critical mass at which runaway accretion of gas from the disk occurs. We note that at the solar value of C/O = 0.53, not only does Jupiter (red hexagon) fall to the right of this mass gap, but Saturn (yellow hexagon) falls near the lower-mass limit edge for a gas giant planet, while both Uranus (pink hexagon) and Neptune (green hexagon) fall at masses well below the gap. In the case of the ratios of O/S, the mass gap spans the same mass range and, while the behavior of the mass limits seem to behave in the opposite sense from that of C/O, this results from the use of oxygen in the numerator instead of the denominator. Taken together, the three panels of [Figure 12](#) reveal the importance of the stellar abundances of C, O, and S in influencing exoplanetary architectures.

In addition to the gap in mass, increasing host star C/O ratios seem to result in larger fractions of lower-mass exoplanets relative to giant exoplanets. There seems to be a slope in the trend of C/O versus exoplanet mass in the sense that, at low M_{pl} , the lower envelope of the distribution has higher C/O ratios (C/O ~ 0.4) than the high M_{pl} regime (C/O ~ 0.2).

In order to investigate how sensitive the trends with $\log(M_{\text{pl}}/M_{\oplus})$ are to the precision of [X/H], abundance ratios and $\log(M_{\text{pl}}/M_{\oplus})$, we performed OLS regressions through 1000 Monte Carlo resamplings, considering a normal distribution for the uncertainties of exoplanetary masses, [X/H] and abundance ratios uncertainties, and found percentages of

$p_{\text{OLS}} < 0.001$ of 91% and 84% for [O/H] and [S/H], respectively. The other elements and abundance ratios remain with percentages below 40%, i.e., not having significant trends with $\log(M_{\text{pl}}/M_{\oplus})$. Summarizing, the trends between $\log(M_{\text{pl}}/M_{\oplus})$ and α -elements are robust.

7.5.1. Singles versus Multis

In Figure 12, we show the distribution of [X/H] and C/O, C/S and O/S ratios with $\log(M_{\text{pl}}/M_{\oplus})$ for stars with single systems (white circles) and stars with multi-planetary systems (orange circles). As discussed in Section 7.1, low-mass exoplanets are preferentially found in multi-planetary systems, while massive exoplanets are mostly found in single systems. We performed OLS regressions for the distributions of abundances with $\log(M_{\text{pl}}/M_{\oplus})$, finding for singles $p_{\text{OLS}} < 0.001$ of 71% for [S/H] and below 27% for the other abundances, and, for multis, 72%, 64% and 60% for [Fe/H], [C/H] and [Ni/H], respectively, and below 40% for the other abundances. In summary, for singles, we find a significant trend with [S/H], while for multis, we find significant trends with [Fe/H], [C/H] and [Ni/H].

7.5.2. Populations of Low-[α /Fe] versus High-[α /Fe] Stars

In order to investigate whether the previously found trends between the host star abundances of [O/H] and [S/H] with exoplanetary mass are sensitive to the host stars belonging to different Galactic populations (thin versus thick disk), we first compare, in the top left panel of Figure 13, the histograms of $\log(M_{\text{pl}}/M_{\oplus})$ for exoplanets orbiting low-[α /Fe] (shown in white) and high-[α /Fe] (shown in red) host stars. The two histograms cover the same range in M_{pl} between 4 – 2000 M_{\oplus} , but they have peaks at different masses: roughly at 10 M_{\oplus} and 200 M_{\oplus} , respectively, for the low-[α /Fe] and high-[α /Fe] distributions. The K-S tests show that their $\log(M_{\text{pl}}/M_{\oplus})$ distributions are indistinguishable (percentage of $p_{\text{KS}} < 0.001$ of 2%). The distributions of host star [X/H] and C/O, C/S and O/S with exoplanetary mass are shown in the other panels of Figure 13, which are similar to those shown in Figure 12, but now the different colors segregate between the high-[α /Fe] (red circles) and low-[α /Fe] stars (black circles).

We find statistically significant trends for host star [X/H] versus $\log(M_{\text{pl}}/M_{\oplus})$ in the low-[α /Fe] population for all elements studied. In contrast, we find no trends for the high-[α /Fe] host star population (the percentages of $p_{\text{OLS}} < 0.001$ are 85%, 56%, 81%, 84%, 80%, 0%, 2%, and 0% for [Fe/H], [C/H], [O/H], [S/H], [Ni/H], C/O, C/S and O/S, respectively, for the low-[α /Fe] population and below 14% for all abundances for the high-[α /Fe] population). We acknowledge that it is possible that stars on the high-[α /Fe] sequence have significant trends between [X/H] and $\log(M_{\text{pl}}/M_{\oplus})$ – which may not have been detected here due to low-number statistics (20 exoplanets).

Recall that although our sample has thick disk stars, it is composed mostly of thin disk stars and, as discussed in Section 7.5, for the full sample we found statistically significant trends between host star [X/H] versus $\log(M_{\text{pl}}/M_{\oplus})$ only for [O/H] and [S/H] (the α -elements studied here), and not for [Fe/H], [C/H] and [Ni/H]. In contrast, for the thin disk sample only, we now find trends for all elements. The possible explanation for this different signature is that there is a higher proportion of massive exoplanets (75%) compared to low-mass exoplanets (25%) around high-[α /Fe] stars (top left panel of Figure 13). The higher proportion of these high-[α /Fe] massive exoplanets tends to flatten the trends between [Fe/H] and [Ni/H] versus $\log(M_{\text{pl}}/M_{\oplus})$. (There are 35 low-mass exoplanets (38%) and 56 massive exoplanets (62%) around low-[α /Fe] stars.) Figure 13 shows that, for [Fe/H] and [Ni/H], as expected, the exoplanets from the high-[α /Fe] sequence (red circles) orbit stars with $[X/H] \lesssim 0.1$. In our sample, below roughly solar metallicity, exoplanets from the low-[α /Fe] sequence (black circles) are scarce.

For the host star C/O, C/S and O/S ratios, as expected, the exoplanets around high-[α /Fe] are mostly found around stars with C/O and C/S below solar. For O/S, they are indistinguishable from the low-[α /Fe] population. For the complete sample, we do not find statistically significant trends between host star abundance ratios and exoplanetary mass. When segregating into two groups, stars on the low- and high-[α /Fe] sequences, we find similar results. Finally, it would be interesting to confirm these results with other α -elements.

7.6. Elemental Abundance Ratios in Hosting Stars and Giant Exoplanets

Probing the elemental abundance ratios in exoplanet host stars is important due to the constraints that they can provide with respect to the formation and distribution of chemical species in the protoplanetary disk (e.g., Thiabaud et al. 2015a, 2015b). The distribution of the elements in the disk is mainly governed by the proximity to the protostar over time, so present-day exoplanet elemental ratio abundances serve as probes of the relative location of planet formation to the ice lines of a variety of C/N/O-bearing (e.g., Öberg et al. 2011; Madhusudhan 2019; Ohno & Fortney 2023) and S-bearing molecules (Crossfield 2023) considering the standard core accretion model for planet formation (Pollack et al. 1996).

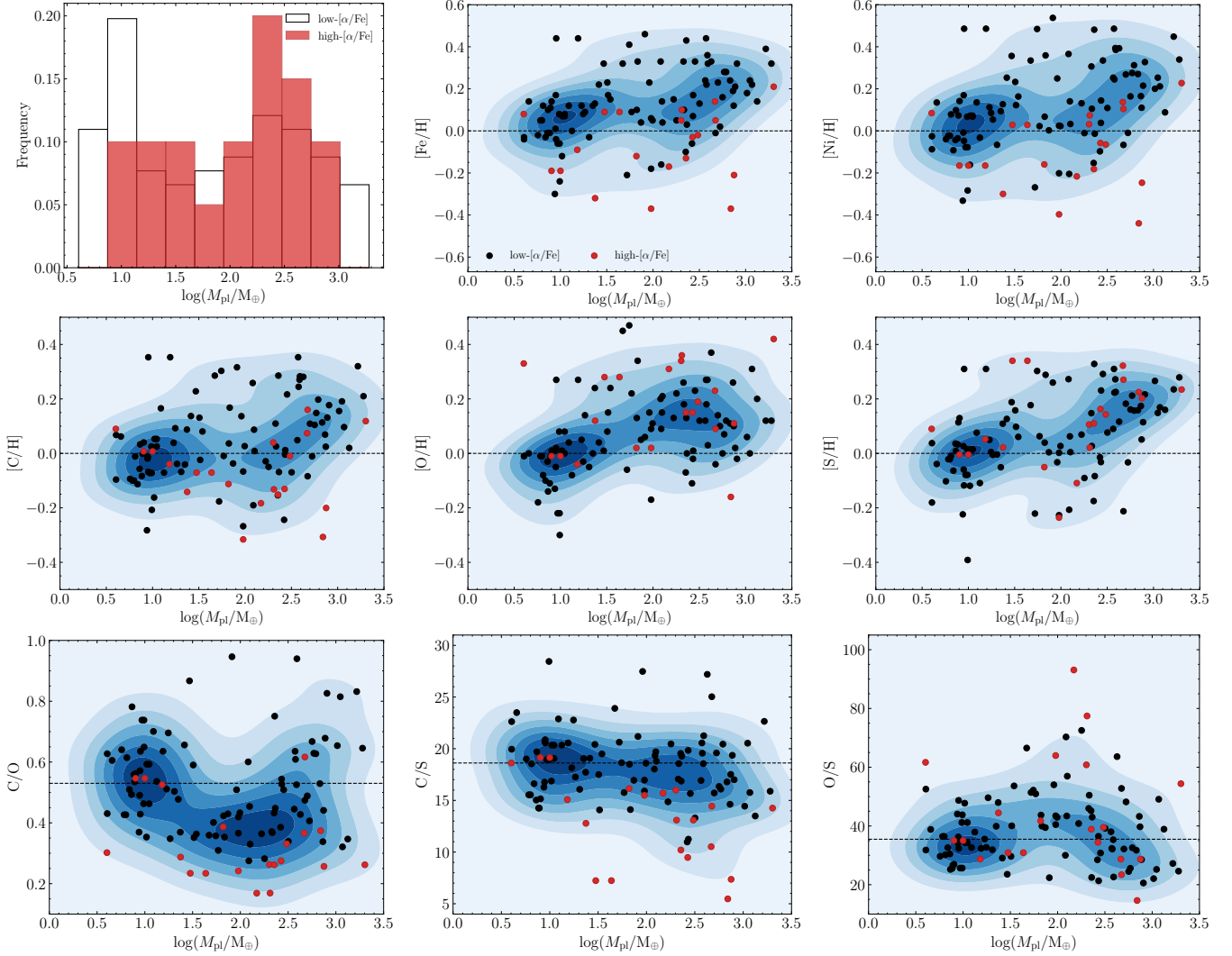


Figure 13. In the top left panel, we show the mass distributions of exoplanets around stars having low- $[\alpha/\text{Fe}]$ (white) and high- $[\alpha/\text{Fe}]$ (red). In the other panels, we show the distribution of $[X/\text{H}]$ and abundance ratios of host stars as a function of exoplanet mass. In the top row, we show $[\text{Fe}/\text{H}]$ (middle panel) and $[\text{Ni}/\text{H}]$ (right panel). In the second row, $[\text{C}/\text{H}]$ (left panel), $[\text{O}/\text{H}]$ (middle panel) and $[\text{S}/\text{H}]$ (right panel). In the last row, C/O (left panel), C/S (middle panel), and O/S (left panel) ratios. Stars on the low- $[\alpha/\text{Fe}]$ are presented in black circles and, on the high- $[\alpha/\text{Fe}]$, in red circles. The blue heat map represents the distribution of all exoplanets, independently of their status as low- or high- $[\alpha/\text{Fe}]$. The black dashed lines represent the solar values.

7.6.1. C/O ratios

Besides H and He, C and O are the most abundant elements in the Universe and are present in the primordial molecular cloud and in the protoplanetary disk – having been the first elemental abundance ratio proposed to possibly trace the formation pathway of giant planets (e.g., Seager et al. 2005). Different locations of the ice lines of H_2O , CO and CO_2 governs the availability of C and O and, consequently, C/O in the gas and solid phases throughout the disk (e.g., Öberg et al. 2011; Espinoza et al. 2017), which will contribute to the final composition of the exoplanet through the accretion of these materials.

The study by Teske et al. (2014) determined the carbon and oxygen abundances of a stellar sample hosting 16 Jupiter exoplanets and found no significant trends between host star C/O ratio and exoplanet equilibrium temperature (T_{eq}) and radius. In Figure 14 (top row), we present our C/O results for our sample containing 75 hot Jupiters. We collected the exoplanet equilibrium temperature values from the NASA Exoplanet Archive and performed OLS regressions for the host star C/O as a function of exoplanet R_{pl} and T_{eq} . For C/O versus T_{eq} , we find no trend ($p_{\text{KS}} < 0.001$ for 0%

of the bootstrapped samples) for a sample of 95 hot Jupiters – in general agreement with [Teske et al. \(2014\)](#) results. For C/O versus R_{pl} , we see no trend with the OLS regressions (0%).

Our sample allows for investigating the behavior of the host star C/O ratio versus R_{pl} and T_{eq} for all exoplanet classes in this study, segregating the exoplanets samples as before: all, sE/SE/sN, sS/J, sN, sS, J, hot, warm_{(10,30]} and warm_{(10,100]}). We performed OLS regressions of host star C/O versus R_{pl} and T_{eq} for all combinations and found a statistically significant trend only for host star C/O versus R_{pl} for stars hosting hot exoplanets (156 exoplanets), for which we obtained median $R^2 = 0.07^{+0.04}_{-0.03}$, a negative angular coefficient with median t -value $= -3.44^{+0.87}_{-0.96}$ and $p_{\text{KS}} < 0.001$ for 54% of the bootstrapped samples.

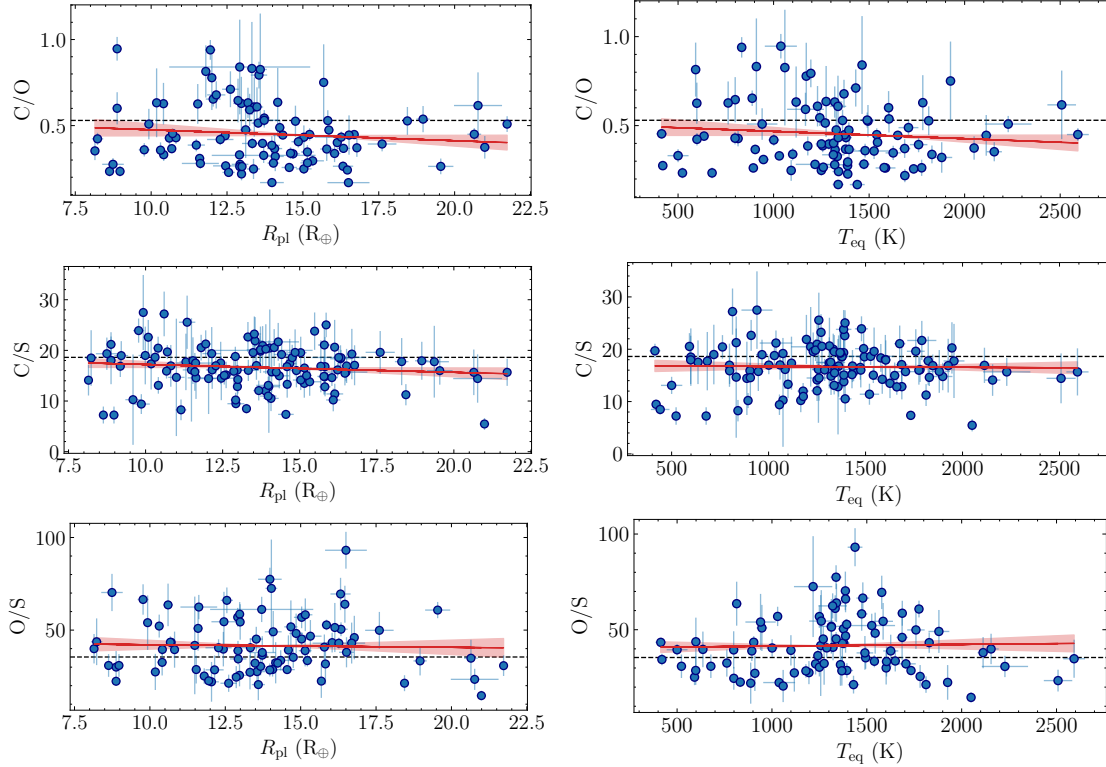


Figure 14. Distribution of C/O (top row), C/S (middle row) and O/S (bottom row) of stars hosting hot Jupiters with planet radius (left panel) and planet equilibrium temperature (right panel). The red line is the OLS linear regression and the painted part represents the errors associated with the regression. The black dashed line represents the solar value.

COMPARISONS WITH EXOPLANET C/O RATIOS

Over 40 giant exoplanets have their atmospheric C/O abundance ratios determined and published in the literature to date (e.g., [Bonnefoy et al. 2018](#); [Changeat et al. 2022](#); [Weiner Mansfield et al. 2024](#)) and these measured C/O ratios can vary considerably between exoplanets from the same system and, also, from the host star C/O value (e.g., [Madhusudhan 2012](#); [Konopacky et al. 2013](#); [Moses et al. 2013](#)). Recently, [Baburaj et al. \(2025\)](#) determined stellar C/O ratios of five stars with directly imaged exoplanets and found a similar stellar-planet C/O ratio (within 1σ) for seven exoplanets of their sample composed of eight giant exoplanets ($1 M_{\text{J}} < M_{\text{pl}} < 62 M_{\text{J}}$), suggesting that these were formed via gravitational instability process. The only exception was the exoplanet HD 206893 b, which showed $C/O_{\text{pl}} > C/O_{\star}$. Jupiter serves an excellent comparison between stellar and giant planet C/O. It is generally accepted that it formed through core accretion ([Pollack et al. 1996](#)). Although the C/O ratio can potentially tell us much about Jupiter’s formation ([Lodders 2004](#)), its atmospheric C/O is extremely challenging to determine because water clouds form in the deep atmosphere and deplete the gas in water vapor, the main oxygen carrier. Recent determinations using data from the Juno mission vary depending on the temperature structure used in the models to describe its atmosphere, having values ranging from a solar C/O ratio ([Li et al. 2024](#)) to ~ 2.9 ([Yang et al. 2026](#)).

For our sample, we have six exoplanets in common with the study of [Changeat et al. \(2022\)](#), which provide atmospheric C/O ratios recovered from their free-chemistry retrievals of Hubble Space Telescope (HST) and Spitzer data. Our derived solar C/O ratio is 0.53 while, for [Changeat et al. \(2022\)](#), the solar ratio is 0.55. In Figure 15, we show the results for $\Delta C/O$ (exoplanet-host star) as functions of exoplanet radius and mass. The host star C/O ratios obtained here range between 0.41 and 0.75, and this sample of exoplanets has masses between $\sim 228 - 530 M_{\oplus}$ or $0.72 - 1.67 M_J$ ([Gillon et al. 2014](#); [Stassun et al. 2017](#); [Cortés-Zuleta et al. 2020](#); [Ehrenreich et al. 2020](#); [Noguer et al. 2024](#)). The exoplanet C/O ratios determined by [Changeat et al. \(2022\)](#) are found to be larger than the stellar ones ($C/O_{\text{pl}} > C/O_{\star}$) for all exoplanets, having a median difference of 0.43 ± 0.13 , which is higher than the median difference of -0.04 ± 0.04 found for the directly imaged exoplanets from [Baburaj et al. \(2025\)](#), represented by gray points in the right panel of the second row in Figure 15.

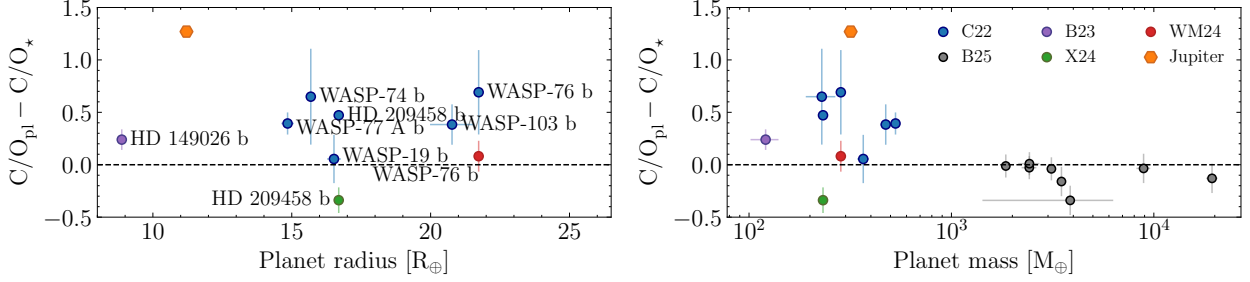


Figure 15. Distributions of $C/O_{\text{pl}} - C/O_{\star}$ with R_{pl} determined in this work (left panel) and M_{pl} taken from the NASA Exoplanet Archive (right panel). The black dashed lines represent the solar values, blue, violet, green, red and gray points represent atmospheric C/O data from [Changeat et al. \(2022\)](#) (C22), [Bean et al. \(2023\)](#) (B23), [Xue et al. \(2024\)](#) (X24), [Weiner Mansfield et al. \(2024\)](#) (WM24) and [Baburaj et al. \(2025\)](#) (B25), and the orange hexagon represents Jupiter ([Lodders 2004](#)) for comparison.

We have two exoplanets in our sample with atmospheric C/O ratios determined using transmission spectra obtained with the James Webb Space Telescope (JWST, [Gardner et al. 2006, 2023](#)), HD 149026 b ($C/O_{\text{pl}} = 0.84 \pm 0.03$, [Bean et al. 2023](#)) and HD 209458 b ($C/O_{\text{pl}} = 0.11^{+0.12}_{-0.06}$, [Xue et al. 2024](#)), and one with the Immersion GRating Infrared Spectrometer (IGRINS) on the Gemini-S telescope, WASP-76 b ($C/O_{\text{pl}} = 0.90^{+0.13}_{-0.14}$, [Weiner Mansfield et al. 2024](#)). They have stellar C/O ratios determined in our work, 0.60 ± 0.09 , 0.45 ± 0.02 and 0.51 ± 0.05 for HD 149026, HD 209458 and WASP-76, respectively, and exoplanetary masses from the NASA Exoplanet Archive, $120.78 \pm 19.07 M_{\oplus}$ ([Stassun et al. 2017](#)), $232.02 \pm 12.71 M_{\oplus}$ ([Stassun et al. 2017](#)) and $284.14^{+4.45}_{-4.13} M_{\oplus}$ ([Ehrenreich et al. 2020](#)). The median difference $C/O_{\text{pl}} - C/O_{\star}$ is 0.08 ± 0.16 , which is more compatible with the exoplanets from [Baburaj et al. \(2025\)](#) instead of [Changeat et al. \(2022\)](#), as can also be seen in Figure 14 (second row, right panel). This might be due to the fact that, as stressed by [Changeat et al. \(2022\)](#), HST and Spitzer data alone are not sensitive enough to precisely constrain atmospheric C/O of exoplanets. However, we also note that the exoplanets from [Baburaj et al. \(2025\)](#) are more massive and orbit further away from their host stars. This spread we observed for differences between the planetary and stellar C/O ratios reinforces the importance of keep pursuing the characterization of exoplanet atmospheres with high-quality data, such as from JWST, to increase the number of accurate atmospheric C/O determinations to better constrain exoplanet formation mechanisms.

Our results do not suggest trends between $\Delta C/O$ (exoplanet – host star) versus exoplanet radius (p -value = 0.56). However, concerning the behavior of $\Delta C/O$ versus exoplanet mass, there is a hint of a possible anti-correlation when considering the $\Delta C/O$ for the lower mass exoplanets from [Changeat et al. \(2022\)](#) and the more massive exoplanets from [Baburaj et al. \(2025\)](#). There seems to be a possible threshold in exoplanet mass (from this plot, possibly around $\sim 10^3 M_{\oplus}$ or $\sim 3.15 M_J$), although this is, at this point, a speculation) below which the C/O ratios of exoplanets tend to be larger than those of their host stars, while this is not the case for the more massive exoplanets, where their C/O ratios are roughly the same or lower than the host stars. In this context, [Hoch et al. \(2023\)](#) analyzed the C/O ratios of nine directly imaged planets and 25 transiting exoplanets from [Changeat et al. \(2022\)](#) and found a trend between exoplanet C/O ratios and their masses (M_J), with a break around $4 M_J$ in which exoplanets below this mass show a wide spread of C/O ratios ($\sim 0.3 - 1.6$) and more massive exoplanets are restricted to values around 0.7 ± 0.2 – which aligns with our possible threshold around $3 M_J$. The two groups of exoplanets are different according to K-S and Anderson-Darling tests ($p_{\text{KS}} = 0.0007$ and $p_{\text{AD}} = 0.0009$), indicating possibly two different formation pathways. However, considering

only the higher-quality data from JWST and IGRINS, we see no significant difference ($p_{\text{KS}} = 0.19$ and $p_{\text{AD}} = 0.14$). We also looked for possible trends between $\Delta\text{C/O}$ and R_{pl} , P_{orb} , M_{pl} , $[\text{X}/\text{H}]$ and $[\text{X}/\text{Fe}]$ and found none.

In conclusion, exoplanet formation and evolution are stochastic processes that involve many mechanisms, such as possible exoplanet migration during its formation, inhomogeneities in the disk, non-static disk temperature profile, fraction of gas and solids accreted, vertical mixing and others (e.g., Espinoza et al. 2017; Madhusudhan 2019). In this regard, C/O is important but, for a more complete overview of exoplanets' formation history, C/O needs to be analyzed together with a wider variety of elemental ratios due to the high volatility of both C and O (e.g., Pacetti et al. 2022).

7.6.2. C/S and O/S ratios

In contrast with C/N/O-bearing molecules, which have condensation temperatures below 200 K (Lodders et al. 2025), S condenses into troilite (FeS) at much higher temperatures (~ 700 K), placing its ice line closer to the star at ~ 0.3 AU (e.g., Oka et al. 2011). Kama et al. (2019) estimated that $\gtrsim 90\%$ of disk sulfur is in the form of ices or refractory minerals, which indicates that sulfur has a refractory behavior in the disk (e.g., Lodders 2004). In light of that, Crossfield (2023) used volatile-to-sulfur ratios (C/S and O/S) to investigate two different models of giant planet formation, through the accretion of pebbles versus planetesimals. For example, for the hot Jupiter WASP-39 b, they suggest that planetesimal accretion is more consistent with the observed SO_2 composition of the atmosphere. This emerges from the fact that pebble accretion models predict that gas giants become highly enriched in volatile elements compared to refractories (e.g., Schneider & Bitsch 2021a, 2021b, 2022) and planetesimals accretion models predict solar C/S and O/S ratios, as well as C/O values (e.g., Pacetti et al. 2022).

Continuing to focus on the giant exoplanets, we now explore the distributions of host star C/S and O/S ratios with exoplanet radius and equilibrium temperature (see the middle and bottom rows of Figure 14). C/S and O/S versus R_{pl} and T_{eq} have similar behaviors as the distribution of C/O ratios, showing a generally flat trend (percentages of p -values < 0.001 for 0% of the bootstrapped samples), with a slightly negative inclinations of the OLS regressions and no statistically significant trends.

COMPARISONS WITH EXOPLANET C/S AND O/S RATIOS

To the best of our knowledge, HAT-P-26 b is the only exoplanet with atmospheric C/S and O/S determined (Gressier et al. 2025) using JWST. In that study, they found atmospheric C/S ratio of $1.29_{-0.97}^{+2.87} \times \text{solar}$ and O/S ratio of $5.39_{-3.61}^{+6.62} \times \text{solar}$, i.e., C/S ratio between $0.3 - 4 \times \text{solar}$ and O/S ratio between $2 - 12 \times \text{solar}$. HAT-P-26 b is a low-mass giant exoplanet with $R_{\text{pl}} = 6.333_{-0.359}^{+0.807} R_{\oplus}$ and $M_{\text{pl}} = 18.751 \pm 2.225 M_{\oplus}$ (Hartman et al. 2011). Its determined radius in our work is $6.68 \pm 0.11 R_{\oplus}$, which is in agreement with Hartman et al. (2011) results. HAT-P-26 b is a hot exoplanet with $P_{\text{orb}} = 4.24$ days (Stassun et al. 2017).

This exoplanet is part of our sample. We determined its host star atmospheric parameters and found $T_{\text{eff}} = 5071$ K, $[\text{Fe}/\text{H}] = 0.04$ dex and $\log g = 4.51$ dex, and obtained $A(\text{C}) = 8.69 \pm 0.11$ dex and $A(\text{S}) = 7.42 \pm 0.03$ dex, and a C/S ratio of 18.62 ± 4.83 . (Unfortunately, due to atmospheric contamination in the [O I] line, $A(\text{O})$ could not be determined.) However, as discussed in Section 4.4, in this low effective temperature regime, our derived C, and S abundances are likely affected by systematics. Here, we can use the calibration (OLS regression) from Section 4.4 to correct the C and S abundances of HAT-P-26. The corrected absolute abundances are $A(\text{C})_{\text{corrected}} = 8.55$ dex and $A(\text{S})_{\text{corrected}} = 7.20$ dex, resulting in a host star $\text{C/S}_{\text{corrected}} = 22.39 \pm 4.83$.

Using the atmospheric C/S value determined for HAT-P-26 b in Gressier et al. (2025) of $\text{C/S}_{\text{HAT-P-26 b}} = 0.3 - 4 \times \text{solar}$, and adopting the solar C/S ratio of 18.62 ± 2.71 derived in this study, we obtain $\text{C/S}_{\text{HAT-P-26 b}} = 5.59 - 74.48$, which is $0.27 - 3.46 \times$ the C/S ratio of the host star. According to Gressier et al. (2025), C/S ratios $\sim 3 - 20 \times \text{solar}$ are expected in pebble accretion formation scenarios, which typically take place beyond the FeS ice line. However, the current uncertainties in the exoplanet atmospheric C/S ratio limit the diagnostic power to distinguish between alternative scenarios for planet formation (e.g., Turrini et al. 2021; Crossfield 2023). Finally, in the coming years, the number of H_2S and SO_2 detections with JWST will increase, allowing for a broader picture of how sulfur impacts atmospheric processes and planet formation scenarios (e.g., Polman et al. 2023).

8. CONCLUSIONS

In this paper, we determined atmospheric parameters and chemical abundances for 290 solar-type exoplanet hosting stars selected from the NASA Exoplanet Archive. We analyzed high-resolution and high SNR publicly available spectra from HARPS-North and HARPS-South archives. The atmospheric parameters effective temperature (T_{eff}), metallicity

([Fe/H]), surface gravity ($\log g$) and microturbulent velocity (v_{mic}), were determined using a classical spectroscopic analysis (Ghezzi et al. 2018, 2021). We determined stellar radius, mass, and age for the sample stars using the isochrone method with the PARAM code (da Silva et al. 2006). Chemical abundances of carbon, oxygen, sulfur, and nickel were derived using atomic lines and the LTE line analysis code MOOG (Snedden 1973). Based on abundance data available in VizieR and the Hypatia catalog, as of December 2025, we report, for the first time, carbon abundances for 75 stars, oxygen abundances for 63 stars, sulfur abundances for 115 stars, and nickel abundances for 69 stars.

We investigated possible trends between the chemical composition of host stars, exoplanet radii (R_{pl}), exoplanet orbital periods (P_{orb}) and exoplanet mass (M_{pl}). In addition, we also discussed the similarities between atmospheric abundance ratios of exoplanet atmospheres and their hosting-star abundance ratios for a small sample of exoplanets. The main results obtained in this work are as follows:

- In our sample, stars hosting giant exoplanets ($R_{\text{pl}} > 4 R_{\oplus}$) have a higher median [X/H] than stars hosting small exoplanets for all studied elements (see Figure 8). K-S tests were performed between the two samples (with and without giant exoplanets) and returned significant differences for all [X/H], except [C/H]. This suggests that there is likely a difference in the distributions of [Fe/H], [O/H], [S/H], and [Ni/H] between stars hosting giant and small exoplanets. In addition, we find a correlation between exoplanet radius and host star [Fe/H] (see Figure 9). Such results are in line with previous findings from the literature (e.g., Petigura et al. 2018b; Ghezzi et al. 2021; Wilson et al. 2022; Ghezzi et al. 2026). The distributions of host star [O/H], [S/H], and [Ni/H] versus exoplanet radius are overall similar to the behavior for [Fe/H], but the slopes are steeper for the α -elements [O/H] and [S/H];
- The [Fe/H] of stars hosting hot exoplanets ($P_{\text{orb}} \lesssim 10$ days) are, on average, more metal rich than those hosting warm exoplanets, as previously found (e.g., Mulders et al. 2016). When considering only exoplanets with $P_{\text{orb}} \leq 30$ days, OLS regressions show a statistically significant anti-correlation between host star [Fe/H] and P_{orb} (see Figure 9). One significant result from this study is that [Fe/H] does not continue to decline as the orbital period increases, but rather rises again for exoplanets with larger orbital periods. The median [Fe/H] abundances stay moderately flat around 0.09 dex for $P_{\text{orb}} \lesssim 10$ days, decrease to 0.01 dex for $10 \lesssim P_{\text{orb}} \lesssim 30$ days and increase again to 0.09 dex for $P_{\text{orb}} > 30$ days. To further confirm these trends we combined our sample with the Kepler sample from Ghezzi et al. (2026), resulting in a combined sample of 1210 exoplanets, all with host star parameters derived homogeneously. The results from this larger combined sample are very similar to the ones from our sample, confirming that the median [Fe/H] are enhanced for large orbital period regime;
- When segregating the sample into stars hosting only small exoplanets (sub-Earths, super-Earths and/or sub-Neptunes), we find significant differences between the abundances of hot ($P_{\text{orb}} \leq 10$ days) and warm ($10 < P_{\text{orb}} \leq 30$ days) exoplanet hosts for all elements. This is also observed between stars hosting hot and warm sub-Saturns. However, for systems having at least one Jupiter-size exoplanet, no differences were found between hosts of hot and warm exoplanets. The K-S tests suggest significant (p -value <0.001) differences for Fe, C and Ni for hosts of small exoplanets, Fe and Ni for sub-Neptune hosts, and Fe, C and Ni for sub-Saturn hosts. For C/S and O/S, when segregating the sample into stars hosting exoplanets of different size classes, we find significant differences between stars hosting hot and warm exoplanets for systems having at least 1 sub-Saturn for C/S and for systems hosting only small exoplanets and at least 1 sub-Neptune for O/S;
- Concerning the C/O ratios, hosts of 3 – 4 R_{\oplus} sub-Neptunes have the highest median C/O value of $0.55^{+0.05}_{-0.01}$, while the lowest values of $0.43^{+0.02}_{-0.03}$ are found for Jupiter hosts (see Figure 11). The K-S tests suggest that their differences are significant. There is an anti-correlation between C/O ratios versus R_{pl} for stars hosting hot exoplanets. Also, stars hosting only small exoplanets ($R_{\text{pl}} \leq 4 R_{\oplus}$) have higher median C/O ratio than stars hosting at least one giant exoplanet. By segregating the sample, we find significant differences between stars hosting hot and warm exoplanets for systems having only small exoplanets;
- For our sample, there seems to be a gap in exoplanet mass between $\sim 20 - 100 M_{\oplus}$ in the distribution of host-star [X/H] as a function of exoplanet mass (see Figure 12). Stars hosting low-mass exoplanets show median abundances around solar values for all elements, whereas stars hosting massive exoplanets exhibit higher median abundances, with the exception of carbon. The fact that giant exoplanets are preferentially found around oxygen-enriched stars, but not carbon-enriched stars, may point to the greater importance of the H₂O ice line compared to the CO and CO₂ ice lines in the formation of giant exoplanet cores;

- The distribution of [O/H] and [S/H] as a function of exoplanet mass, for our sample, shows steep trends – the α -elements studied here (see Figure 12). However, when dividing the sample into hot and warm exoplanet hosts, these trends are only found for warm exoplanets – which may be linked to the orbital distances in which these exoplanets are formed;
- We find a significant difference between the distributions of C/O ratios of stars hosting low-mass versus massive exoplanets; increasing C/O ratios seem to result in larger fractions of low-mass exoplanets relative to massive exoplanets (see Figure 12). Additionally, the position of the gap in exoplanet mass changes with the C/O abundance ratios, with the lower-mass limit for giant exoplanets increasing with increasing C/O ratios. This may indicate that enhanced C/O ratios result in a more efficient (or faster) build-up of solid cores to the critical mass that results in runaway gas accretion and the formation of a giant planets;
- Our sample has 20 exoplanets orbiting high-[α /Fe] stars and 91 orbiting low-[α /Fe] stars. There is a higher fraction of low-mass exoplanets around low-[α /Fe] stars and, also, of massive exoplanets around high-[α /Fe] stars (see Figure 13). We find trends between host star [X/H] and $\log(M_{\text{pl}}/M_{\oplus})$ only for exoplanets around low-[α /Fe] stars – including [Fe/H] and [Ni/H], for which no trends were found for the complete sample. The higher fraction of massive exoplanets orbiting high-[α /Fe] stars, most of them around [Fe/H] \lesssim 0.00, may be responsible for flatter trends between [Fe/H] and [Ni/H] versus $\log(M_{\text{pl}}/M_{\oplus})$;
- The C/O ratios for the host stars were also compared with those ratios measured in the atmospheres of exoplanets (see Figure 15). We have six exoplanets in common with the sample of [Changeat et al. \(2022\)](#) (HST+Spitzer data) and we find that $C/O_{\text{pl}} > C/O_{\star}$ for all exoplanets. When comparing our results with the C/O ratios from the sample of eight directly imaged exoplanets from [Baburaj et al. \(2025\)](#), which are more massive and have longer periods than ours, we see that, unlike our sample, seven out of eight exoplanets from [Baburaj et al. \(2025\)](#) had a lower C/O atmospheric ratios than their host stars. Such results combined suggest that there seems to be a possible threshold in exoplanet mass around $\sim 3.15 M_{\text{J}}$ beyond which the C/O ratios in host stars are larger than in the exoplanets ([Hoch et al. 2023](#)). However, by adding 3 exoplanets with atmospheric C/O ratios determined using higher-quality data from JWST and IGRINS, we see no threshold – the $\Delta C/O$ ratios are close to or lower than zero (ranging from -0.34 to 0.24) even for lower-mass planets.

We thank the anonymous referee for insightful questions that helped to improve the paper. We thank Eve J. Lee for discussions that resulted in reshaping the paper. This study was financed in part by the Coordenação de Aperfeiçoamento de Pessoal de Nível Superior – Brasil (CAPES) – Finance Code 001. E.C.A. acknowledges financial support from Fundação Carlos Chagas Filho de Amparo à Pesquisa do Estado do Rio de Janeiro (FAPERJ) through a Ph.D. Scholarship Grade A under grant E-26/203.647/2024. L.G. acknowledges financial support from Fundação Carlos Chagas Filho de Amparo à Pesquisa do Estado do Rio de Janeiro (FAPERJ), through the ARC research grant E-26/211.386/2019. This research has made use of the NASA Exoplanet Archive, which is operated by the California Institute of Technology, under contract with the National Aeronautics and Space Administration under the Exoplanet Exploration Program. This research used the facilities of the Italian Center for Astronomical Archive (IA2) operated by INAF at the Astronomical Observatory of Trieste. This research is based on data obtained from the ESO Science Archive Facility with DOI: <https://doi.org/10.18727/archive/33> ([European Southern Observatory \(ESO\) 2014](#)). This work has made use of the VALD database, operated at Uppsala University, the Institute of Astronomy RAS in Moscow, and the University of Vienna. The research shown here acknowledges the use of the Hypatia Catalog Database, an on-line compilation of stellar abundance data as described in [Hinkel et al. \(2014\)](#), which was supported by NASA’s Nexus for Exoplanet System Science (NExSS) research coordination network and the Vanderbilt Initiative in Data-Intensive Astrophysics (VIDA). This research has made use of the SIMBAD astronomical database and the VizieR catalogue access tool, operated at CDS, Strasbourg, France ([Wenger et al. 2000](#)). The original description of the VizieR service was published in [Ochsenbein et al. \(2000\)](#). This research has made use of the NASA/IPAC Infrared Science Archive, which is funded by the National Aeronautics and Space Administration and operated by the California Institute of Technology.

A. LIST OF SPECTRA

We present the identifications of the spectra used in this work, obtained from the ESO Science Archive Facility (HARPS-South data) and the Italian Center for Astronomical Archive (HARPS-North data) in Table 5.

Star	RA J2000 (deg)	DEC J2000 (deg)	General	N_{general}
55 Cnc	133.1468373	28.3298154	HARP.N.2014-01-02T01-37-59.495_s1d_A,HARP.N.2014...	3
BD+20 594	53.6511231	20.5990205	ADP.2015-11-16T02:00:40.567,ADP.2015...	25
CoRoT-1	102.0798591	-3.1021394	ADP.2014-09-18T12:10:34.533,ADP.2014...	34
CoRoT-4	102.1946233	-0.6727861	ADP.2014-09-18T12:17:41.010,ADP.2014...	25

Oxygen	N_{oxygen}
HARP.N.2014-01-01T23-42-13.573_s1d_A,HARP.N.2014...	2
ADP.2015-11-16T02:00:40.567,ADP.2015...	25
-	-
-	-

Table 5. HARPS-South and HARPS-North data used. Column 1 shows the stellar identification. Columns 2 and 3 show the coordinates. Columns 4 and 5 show the original identification of the spectra obtained in the archives and the total number of spectra, respectively. Columns 6 and 7 show the spectra clean of telluric features or any contamination (see Section 4.2) and the total number of spectra, respectively.

NOTE—This table is published in its entirety in the machine-readable format. A portion is shown here for guidance regarding its form and content.

B. COMPARISONS WITH RESULTS FROM THE LITERATURE

B.1. Atmospheric Parameters

We compared our atmospheric parameters with the values from the Mean PASTEL catalog (Soubiran et al. 2022), which is the mean version of the PASTEL catalog (Soubiran et al. 2016), a compilation of atmospheric parameters determinations using high-resolution data. In Figure 16, we see an excellent agreement for the 75 stars in common with the catalog, finding median differences of 12 ± 33 K, -0.01 ± 0.03 and 0.02 ± 0.06 dex for T_{eff} , $[\text{Fe}/\text{H}]$ and $\log g$, respectively, and R^2 values of 0.04, 0.01 and 0.36 for the residuals. The R^2 value of $\log g$ is being very influenced by the stars with $\log g > 4.65$ dex in PASTEL – without them, the value decreases to 0.22.

For the stars with the greatest differences, although still acceptable, we highlight a couple of them. For T_{eff} , we highlight Kepler-1300, WASP-32, WASP-42 and WASP-70 A. For Kepler-1300 (5830 ± 21 K), PASTEL has a mean value of 6023 ± 25 K based on 3 determinations, 6021 ± 60 K (Petigura et al. 2017), 6027 ± 28 K (Brewer & Fischer 2018) and 6014 ± 100 K (Furlan et al. 2018), but we find a determination more compatible with ours in the literature, 5874 K (McQuillan et al. 2013). For WASP-32 (6159 ± 21 K), PASTEL has only one value of 6427 ± 141 K (Mortier et al. 2013), but we find 6111 ± 51 (Magrini et al. 2022) in the literature. For WASP-42 (5102 ± 41 K), PASTEL has only one value of 5315 ± 79 K (Mortier et al. 2013), but we find 5031 ± 80 K (Magrini et al. 2022) and 5115 K (Matsuno et al. 2024) in the literature. For $[\text{Fe}/\text{H}]$, we highlight Kepler-1300 and WASP-32. For Kepler-1300 (0.12 ± 0.02 dex), PASTEL has a mean value of -0.13 ± 0.03 dex. For WASP-32 (-0.02 ± 0.02 dex), PASTEL has only one measurement of 0.28 ± 0.10 dex (Mortier et al. 2013), but we find 0.03 dex (Boettner et al. 2024) and 0.02 dex (Ye et al. 2025) in the literature. For $\log g$, we highlight WASP-32 and WASP-71. For WASP-32 (4.42 ± 0.09 dex), PASTEL has a mean value of 4.93 ± 0.10 dex, but we find 4.40 dex (Chen et al. 2021) and 4.38 dex (de Laverny et al. 2025) in the literature.

B.2. Carbon, Nickel and Sulfur

We compare our abundances determined with equivalent widths, i.e., those of C, Ni and S, with the median absolute abundances from the updated version of the Hypatia catalog (Hinkel et al. 2014, H14) to check if our values are compatible with a global distribution of these abundances. Additionally, we also compare our results with those from

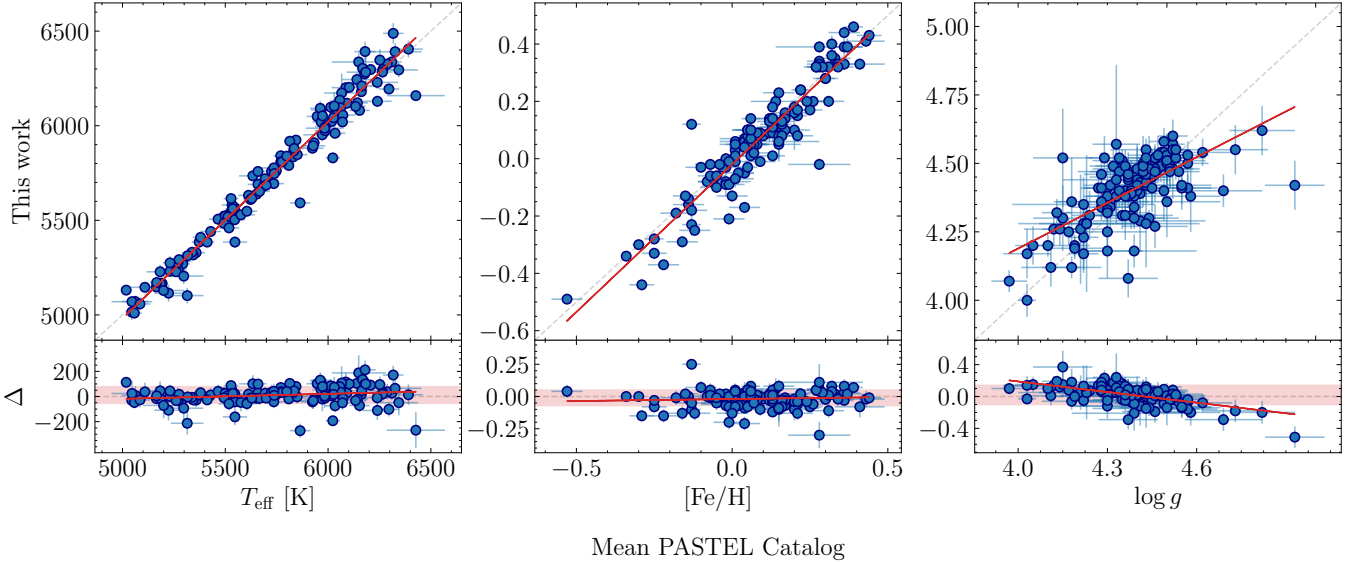


Figure 16. Comparisons between the atmospheric parameters determined in this work and from the Mean PASTEL catalog (Soubiran et al. 2022). T_{eff} in the left column, $[\text{Fe}/\text{H}]$ in the middle column and $\log g$ in the right column. The lower panels of each row show the residuals, where $\Delta_{\text{par}} = \text{par}_{\text{this work}} - \text{par}_{\text{literature}}$. The gray dashed lines represent equality, 1:1, the red lines are the linear regressions fitted to the data and the painted area is the $\pm 2\text{MAD}$ region around the median difference.

the 2022 paper of the GAPS Programme at TNG, Biazzo et al. (2022) (hereafter, BI22), for a wider appraisal of the accuracy and precision of our approach. Finally, we also compare with the abundances C and Ni abundances of Brewer et al. (2016) (hereafter, B16) and S abundances of Perdigon et al. (2021) (hereafter, P21). In Figure 17, we compare our abundances directly.

For the Hypatia catalog, we have 59 stars in common with carbon abundances. The median difference between carbon abundances is -0.01 ± 0.04 dex and we found a $R^2 = 0.12$ for the linear fit of the residuals. However, it is noteworthy that high uncertainties can be found in H14 values and this might be due to the fact that, besides having measurements of a variety of techniques, it also has different carbon indicators, mixing atomic lines and molecular band abundances together – which, in general, do not agree in the literature (e.g., Delgado Mena et al. 2021). For nickel, we have an excellent agreement for the 53 stars in common, with a median difference of -0.02 ± 0.03 dex and $R^2 = 0.01$ for the linear fit of the residuals. For C and Ni, we can see a clear outlier in the plots. This star is Kepler-1300, having $A(\text{C}) = 8.53 \pm 0.03$ dex and $A(\text{Ni}) = 6.35 \pm 0.03$ dex. In the catalog, their values are based on determinations by Brewer & Fischer (2018), 8.22 ± 0.09 dex and 6.07 ± 0.05 dex, respectively. Lastly, for sulfur, we have 28 stars in common, with a median difference of 0.00 ± 0.07 dex and $R^2 = 0.51$ for the linear fit of the residuals, reflecting the presence of a moderate trend. This dispersion is typical considering that the blends in sulfur lines decrease the precision of the abundance determination. There are two stars pushing the trend observed in the residuals, K2-188 (7.07 ± 0.05 dex) and TOI-1736 (7.23 ± 0.02 dex), having T_{eff} values of 5959 K and 5753 K, respectively. In the Hypatia catalog, K2-188 and TOI-1736 values are based on determinations by Plotnikova et al. (2024), 7.69 ± 0.09 dex and 6.82 ± 0.09 dex, respectively.

For the stars in common with Brewer et al. (2016), in general, we find an excellent agreement. For carbon, we have 43 stars in common, with a median difference of 0.03 ± 0.04 dex and $R^2 = 0.04$ for the linear fit of the residuals. For nickel, we have 53 stars in common, with a median difference of 0.00 ± 0.03 dex and $R^2 = 0.01$ for the linear fit of the residuals.

For Perdigon et al. (2021) (sulfur), we have 17 stars in common, finding a median difference of -0.02 ± 0.03 dex and $R^2 = 0.19$ for the linear fit of the residuals, reflecting the presence of a weak trend.

For the 18 stars in common with Biazzo et al. (2022), we find median differences of 0.01 ± 0.06 dex, -0.01 ± 0.02 dex and -0.03 ± 0.07 dex for C, Ni and S, respectively, and corresponding R^2 values for the linear fits of the residuals of 0.08, 0.25 and 0.30, reflecting the presence of a weak trend with Ni and S. However, the higher values of dispersion and R^2 found for the residuals might be due to the scarcity of stars in common.

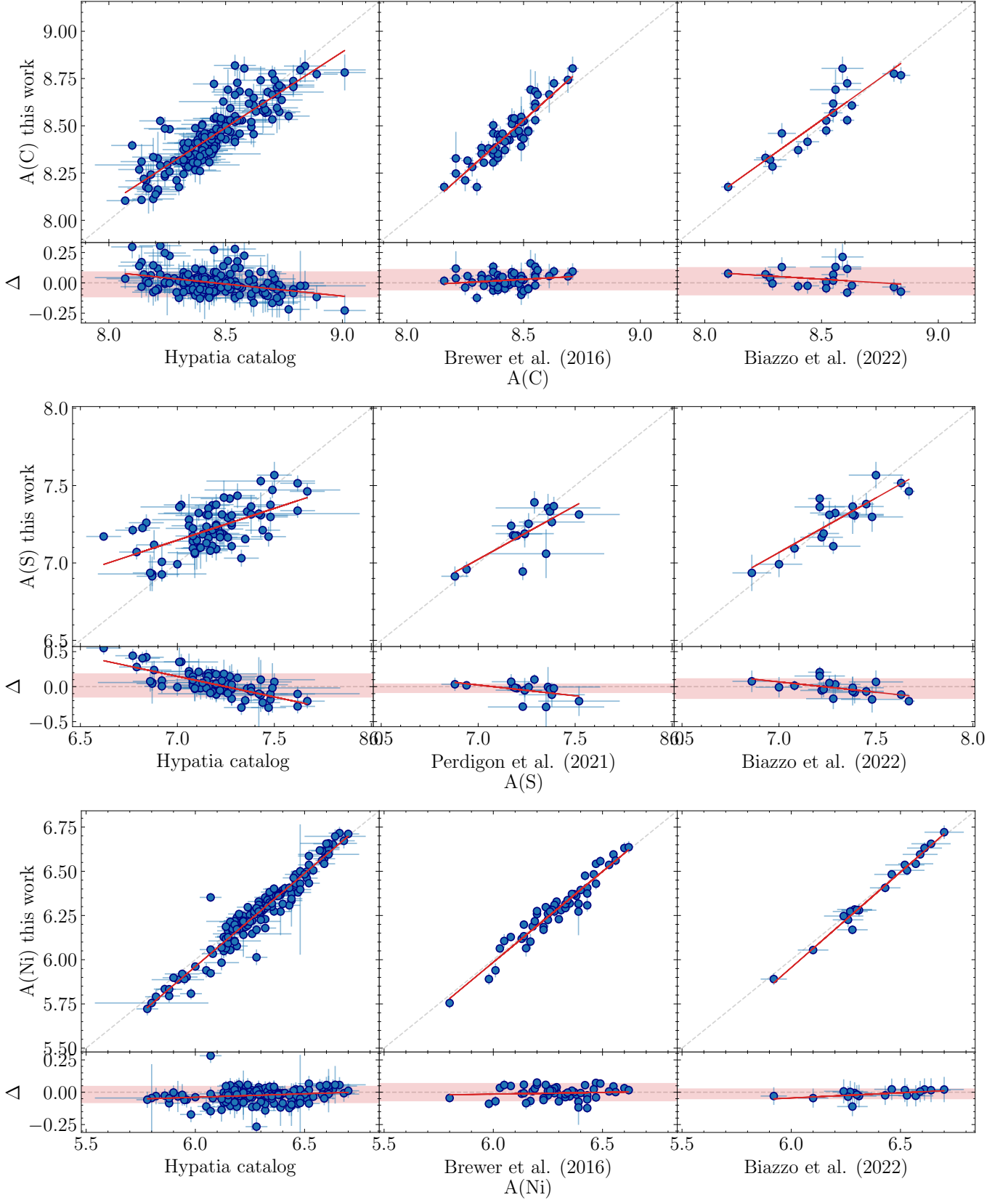


Figure 17. Comparisons between the absolute abundances of C (top row), S (middle row) and Ni (bottom row) determined in this work and in the literature. We compare our abundances with the Hypatia catalog (H14, Hinkel et al. 2014), Brewer et al. (2016) (B16), Perdigon et al. (2021) (P21) and the GAPS Programme sample (BI22, Biazzo et al. 2022). The lines and painted areas are the same as in Figure 16.

B.3. Oxygen

We compare our oxygen abundances, determined using spectral synthesis, with the values of H14, B16 and BI22 (see Figure 18). The abundances from H14 are compiled from works in which oxygen was determined exclusively using the O I triplet at 777 nm, which are lines that suffer from NLTE effects (e.g., Amarsi et al. 2019). B16 determined their abundances using spectral synthesis of the O I triplet at 777 nm and some molecular lines, including OH. BI22 determined their abundances using two methods, the MOOG driver `blends` with EWs (measured with `splot` task from Tody1986) of O I triplet and NLTE corrections by Amarsi et al. (2015) and, also, spectral synthesis of the [O I] line using the MOOG driver `synth`. For the final abundances, they considered the weighted average of the values from the two methods.

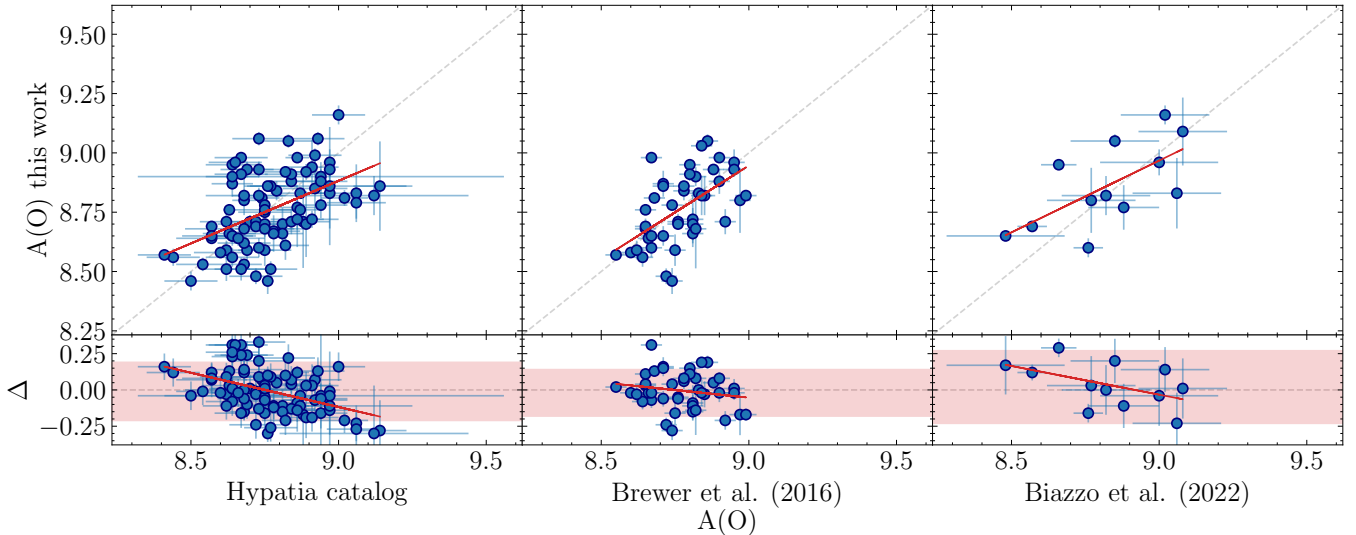


Figure 18. Comparisons between the absolute abundances of O determined in this work and in the literature. We compare our abundances with the Hypatia catalog (H14, Hinkel et al. 2014), Brewer et al. (2016) (B16) and the GAPS Programme sample (BI22, Biazzo et al. 2022). The lines and painted areas are the same as in Figure 16.

Comparing with H14, B16 and BI22, we have 35, 44 and 13 stars in common, respectively, finding median differences of -0.04 ± 0.18 dex, -0.02 ± 0.09 dex and 0.01 ± 0.13 dex and R^2 values of 0.20, 0.06 and 0.22 for the residuals, reflecting the presence of a weak trend with H14 and BI22. Again, this might be due to the low number of stars in common. However, in the literature, we can find examples of the same group using fixed atmospheric parameters and finding different oxygen abundances depending on the indicator they used. Ecuivillon et al. (2006) reported mean abundances of oxygen of a sample of 96 planet-hosting stars determined using 4 different indicators, finding 0.10 ± 0.16 dex with near-UV OH lines, 0.12 ± 0.16 dex with [O I] line, -0.16 ± 0.17 dex with NLTE O I triplet and 0.15 ± 0.17 dex with LTE O I triplet. Finally, considering the discrepancies between oxygen abundances of different indicators, adding the differences of atmospheric parameters and methodologies, these numbers represent a general good agreement between our abundances and those from the literature.

Additionally, to the best of our knowledge, there is not a large sample of stars in common with this work having oxygen abundances determined based on the O I line at 6158 Å. We determined oxygen abundances for 17 stars with the O I line at 6158 Å applying the same methodology as the one used for the [O I] line at 6300 Å (see Section 4.2), but manually. We obtained an excellent agreement between the oxygen abundances obtained with the two oxygen indicators, finding a median difference ($A(O)_{6300} - A(O)_{6158}$) of 0.03 dex for the entire sample, 0.04 dex for the subsample having $80 < \text{SNR} < 120$ and 0.00 dex for the subsample having $\text{SNR} > 400$ (see Figure 19), and MAD of 0.08 for the three subsamples. Finally, we obtained $A(O) = 8.70 \pm 0.05$ dex for the Ceres 2009-02-08 solar spectrum, which is the same abundance obtained using the [O I] line at 6300 Å.

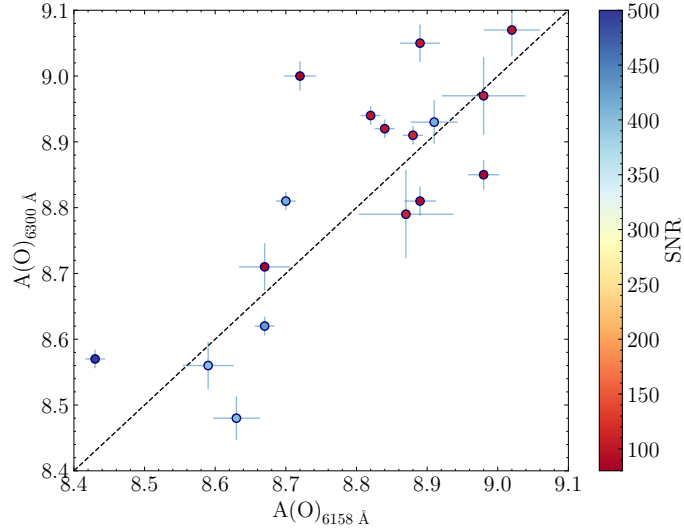


Figure 19. Comparison between abundances of oxygen determined in this work using [O I] line at 6300 Å and O I line at 6158 Å. The colors represent the SNR of the spectra.

B.4. Stellar Radii

We compared our stellar radii with the values from [Stassun et al. \(2017\)](#) (hereafter, S17), [Petigura et al. \(2018a\)](#) (hereafter, P18a), [Kruse et al. \(2019\)](#) (hereafter, K19) and [Loaiza-Tacuri et al. \(2024\)](#) (hereafter, LT24). S17 used T_{eff} , [Fe/H] and $\log g$ values from PASTEL catalog ([Soubiran et al. 2016](#)), broadband photometric data from all-sky catalogs and parallaxes from Gaia DR1 ([Gaia Collaboration et al. 2016](#)) to calculate stellar bolometric fluxes and angular radii. After, they determined stellar radii using the Stefan-Boltzmann law. P18a used HIRES spectra to determine atmospheric parameters for the planet-hosting stars and `isoclassify` Python package ([Huber et al. 2017](#)) to determine stellar masses and radii. K19 used Gaia DR2 ([Gaia Collaboration et al. 2018](#)) stellar radii. LT24 used HIRES spectra of K2 stars observed from campaigns zero through eight (C0-8) to determine atmospheric parameters using the q^2 code ([Ramírez et al. 2014](#)) for planet-hosting stars and PARAM v1.3 code ([da Silva et al. 2006](#)), associated with V magnitudes and Gaia DR3 parallaxes ([Gaia Collaboration et al. 2021](#)), to determine stellar radii.

In Figure 20, we see an excellent agreement with stellar radii values from the literature. We find a median difference of $0.06 \pm 0.03 R_{\odot}$, $0.00 \pm 0.02 R_{\odot}$, $-0.02 \pm 0.02 R_{\odot}$ and $0.04 \pm 0.02 R_{\odot}$ for 21, 13, 12 and 4 stars in common with S17, P18, K19 and LT24, respectively, and R^2 values of 0.02, 0.06, 0.49 and 0.00 for the residuals. The high R^2 value for the residuals with K19 might be associated with the low number statistics since we can visually see a good agreement.

B.5. Exoplanetary Radii

We compare our exoplanetary radii with the values calculated by the same authors mentioned in Section B.4. With their determined stellar radii, S17 used exoplanetary parameters from [exoplanets.org](#) to determine exoplanetary radii, P18a used transit depths calculated from K2 light curves from campaigns five through eight (C5-8), K19 used transit depths calculated from K2 light curves from C0-8 and LT24 used transit depth values from NASA Exoplanet Archive. We see a good agreement with exoplanetary radii values from the literature in Figure 21. We find a median difference of $0.42 \pm 0.51 R_{\oplus}$, $0.02 \pm 0.26 R_{\oplus}$, $0.21 \pm 0.20 R_{\oplus}$ and $0.15 \pm 0.07 R_{\oplus}$ for 56, 17, 31 and 14 exoplanets in common with S17, P18, K19 and LT24, respectively, and R^2 values of 0.00, 0.14, 0.08 and 0.00 for the residuals. Finally, the median uncertainties for the transit depth and exoplanetary radii are 3.00% and 2.00%, respectively.

REFERENCES

- Addison, B., Wright, D. J., Wittenmyer, R. A., et al. 2019, *PASP*, 131, 115003, doi: [10.1088/1538-3873/ab03aa](https://doi.org/10.1088/1538-3873/ab03aa)
- Addison, B. C., Tinney, C. G., Wright, D. J., & Bayliss, D. 2016, *ApJ*, 823, 29, doi: [10.3847/0004-637X/823/1/29](https://doi.org/10.3847/0004-637X/823/1/29)
- Adibekyan, V. 2019, *Geosciences*, 9, 105, doi: [10.3390/geosciences9030105](https://doi.org/10.3390/geosciences9030105)

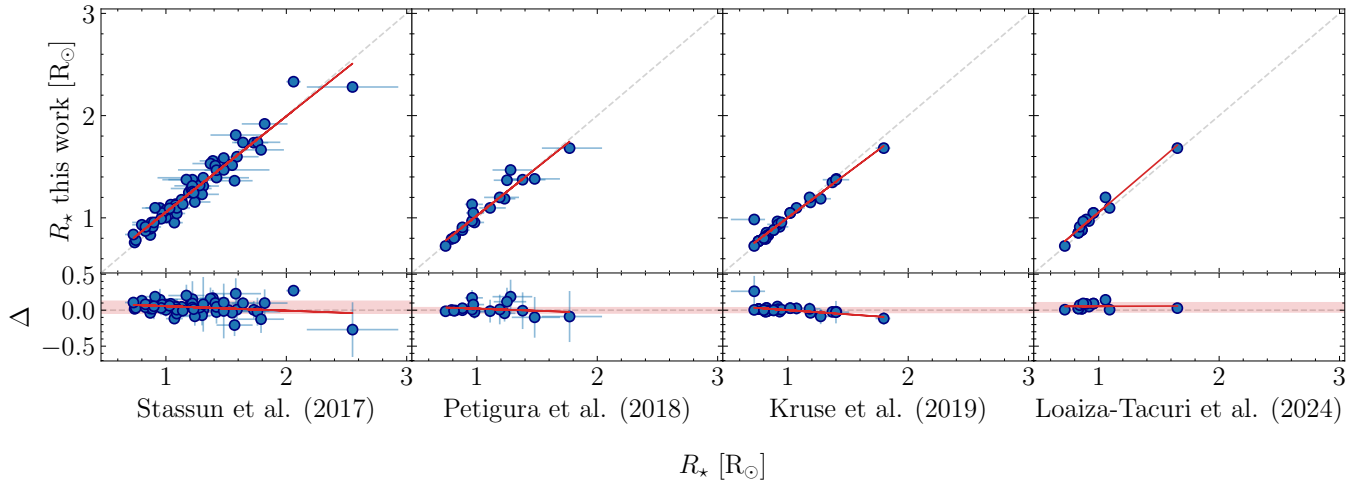


Figure 20. Comparisons between stellar radii determined in this work and in the literature. We compare with S17 (Stassun et al. 2017) in the first panel, P18a (Petigura et al. 2018a) in the second panel, K19 (Kruse et al. 2019) in the third panel and LT24 (Loaiza-Tacuri et al. 2024) in the fourth panel. We show the direct comparisons in the upper panels and the residuals in the lower panels. The lines and painted areas are the same as in Figure 16.

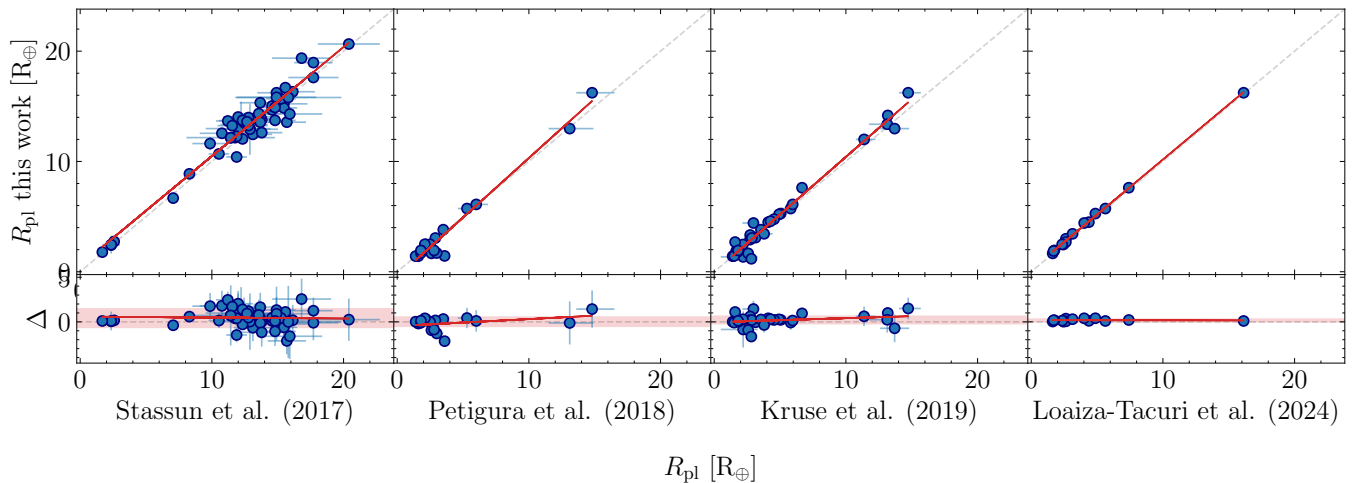


Figure 21. Comparisons between planetary radii determined in this work and in the literature. We compare with S17 (Stassun et al. 2017) in the first panel, P18a (Petigura et al. 2018a) in the second panel, K19 (Kruse et al. 2019) in the third panel and LT24 (Loaiza-Tacuri et al. 2024) in the fourth panel. The lines and painted areas are the same as in Figure 16.

Adibekyan, V. Z., Santos, N. C., Sousa, S. G., & Israelian, G. 2011, *A&A*, 535, L11, doi: [10.1051/0004-6361/201118240](https://doi.org/10.1051/0004-6361/201118240)

Adibekyan, V. Z., Sousa, S. G., Santos, N. C., et al. 2012b, *A&A*, 545, A32, doi: [10.1051/0004-6361/201219401](https://doi.org/10.1051/0004-6361/201219401)

Akeson, R. L., Chen, X., Ciardi, D., et al. 2013, *PASP*, 125, 989, doi: [10.1086/672273](https://doi.org/10.1086/672273)

Alderson, L., Wakeford, H. R., Alam, M. K., et al. 2023, *Nature*, 614, 664, doi: [10.1038/s41586-022-05591-3](https://doi.org/10.1038/s41586-022-05591-3)

Allende Prieto, C., Lambert, D. L., & Asplund, M. 2001, *ApJL*, 556, L63, doi: [10.1086/322874](https://doi.org/10.1086/322874)

Almenara, J. M., Hébrard, G., Díaz, R. F., et al. 2022, *A&A*, 663, A134, doi: [10.1051/0004-6361/202142964](https://doi.org/10.1051/0004-6361/202142964)

Alqasim, A., Grieves, N., Rosário, N. M., et al. 2024, *MNRAS*, 533, 1, doi: [10.1093/mnras/stae1767](https://doi.org/10.1093/mnras/stae1767)

Amarsi, A. M., Asplund, M., Collet, R., & Leenaarts, J. 2015, *MNRAS*, 454, L11, doi: [10.1093/mnrasl/slv122](https://doi.org/10.1093/mnrasl/slv122)

Amarsi, A. M., Nissen, P. E., & Skúladóttir, Á. 2019, *A&A*, 630, A104, doi: [10.1051/0004-6361/201936265](https://doi.org/10.1051/0004-6361/201936265)

Anders, F., Khalatyan, A., Chiappini, C., et al. 2019, *A&A*, 628, A94, doi: [10.1051/0004-6361/201935765](https://doi.org/10.1051/0004-6361/201935765)

Anders, F., Khalatyan, A., Queiroz, A. B. A., et al. 2022, *A&A*, 658, A91, doi: [10.1051/0004-6361/202142369](https://doi.org/10.1051/0004-6361/202142369)

Anderson, D. R., Collier Cameron, A., Delrez, L., et al. 2014, *MNRAS*, 445, 1114, doi: [10.1093/mnras/stu1737](https://doi.org/10.1093/mnras/stu1737)

- Anderson, D. R., Collier Cameron, A., Hellier, C., et al. 2015, *A&A*, 575, A61, doi: [10.1051/0004-6361/201423591](https://doi.org/10.1051/0004-6361/201423591)
- Anderson, D. R., Collier Cameron, A., Delrez, L., et al. 2017, *A&A*, 604, A110, doi: [10.1051/0004-6361/201730439](https://doi.org/10.1051/0004-6361/201730439)
- Armstrong, D. J., Osborn, A., Adibekyan, V., et al. 2023, *MNRAS*, 524, 5804, doi: [10.1093/mnras/stad2183](https://doi.org/10.1093/mnras/stad2183)
- Arnett, D. 1996, *Supernovae and Nucleosynthesis: An Investigation of the History of Matter from the Big Bang to the Present* (Princeton University Press)
- Asplund, M., Amarsi, A. M., & Grevesse, N. 2021, *A&A*, 653, A141, doi: [10.1051/0004-6361/202140445](https://doi.org/10.1051/0004-6361/202140445)
- Asplund, M., Grevesse, N., Sauval, A. J., Allende Prieto, C., & Kiselman, D. 2004, *A&A*, 417, 751, doi: [10.1051/0004-6361:20034328](https://doi.org/10.1051/0004-6361:20034328)
- Asplund, M., Grevesse, N., Sauval, A. J., & Scott, P. 2009, *ARA&A*, 47, 481, doi: [10.1146/annurev.astro.46.060407.145222](https://doi.org/10.1146/annurev.astro.46.060407.145222)
- Azevedo Silva, T., Demangeon, O. D. S., Barros, S. C. C., et al. 2022, *A&A*, 657, A68, doi: [10.1051/0004-6361/202141520](https://doi.org/10.1051/0004-6361/202141520)
- Baburaj, A., Konopacky, Q. M., Theissen, C. A., et al. 2025, *AJ*, 169, 55, doi: [10.3847/1538-3881/ad8dfc](https://doi.org/10.3847/1538-3881/ad8dfc)
- Barge, P., Baglin, A., Auvergne, M., et al. 2008, *A&A*, 482, L17, doi: [10.1051/0004-6361:200809353](https://doi.org/10.1051/0004-6361:200809353)
- Barragán, O., Aigrain, S., Kubyskhina, D., et al. 2019, *MNRAS*, 490, 698, doi: [10.1093/mnras/stz2569](https://doi.org/10.1093/mnras/stz2569)
- Barros, S. C. C., Demangeon, O., & Deleuil, M. 2016, *A&A*, 594, A100, doi: [10.1051/0004-6361/201628902](https://doi.org/10.1051/0004-6361/201628902)
- Battley, M. P., Collins, K. A., Ulmer-Moll, S., et al. 2024, *A&A*, 686, A230, doi: [10.1051/0004-6361/202449307](https://doi.org/10.1051/0004-6361/202449307)
- Bean, J. L., Xue, Q., August, P. C., et al. 2023, *Nature*, 618, 43, doi: [10.1038/s41586-023-05984-y](https://doi.org/10.1038/s41586-023-05984-y)
- Beard, C., Robertson, P., Dai, F., et al. 2024, *AJ*, 167, 70, doi: [10.3847/1538-3881/ad1330](https://doi.org/10.3847/1538-3881/ad1330)
- Becker, J. C., Vanderburg, A., Rodriguez, J. E., et al. 2019, *AJ*, 157, 19, doi: [10.3847/1538-3881/aaf0a2](https://doi.org/10.3847/1538-3881/aaf0a2)
- Bensby, T., Feltzing, S., & Lundström, I. 2004, *A&A*, 415, 155, doi: [10.1051/0004-6361:20031655](https://doi.org/10.1051/0004-6361:20031655)
- Bergemann, M., Hoppe, R., Semenova, E., et al. 2021, *MNRAS*, 508, 2236, doi: [10.1093/mnras/stab2160](https://doi.org/10.1093/mnras/stab2160)
- Bertran de Lis, S., Delgado Mena, E., Adibekyan, V. Z., Santos, N. C., & Sousa, S. G. 2015, *A&A*, 576, A89, doi: [10.1051/0004-6361/201424633](https://doi.org/10.1051/0004-6361/201424633)
- Biazzo, K., D’Orazi, V., Desidera, S., et al. 2022, *A&A*, 664, A161, doi: [10.1051/0004-6361/202243467](https://doi.org/10.1051/0004-6361/202243467)
- Boettner, C., Viswanathan, A., & Dayal, P. 2024, *A&A*, 692, A150, doi: [10.1051/0004-6361/202451537](https://doi.org/10.1051/0004-6361/202451537)
- Boley, A. C., Granados Contreras, A. P., & Gladman, B. 2016, *ApJL*, 817, L17, doi: [10.3847/2041-8205/817/2/L17](https://doi.org/10.3847/2041-8205/817/2/L17)
- Bonfanti, A., Delrez, L., Hooton, M. J., et al. 2021, *A&A*, 646, A157, doi: [10.1051/0004-6361/202039608](https://doi.org/10.1051/0004-6361/202039608)
- Bonfanti, A., Gandolfi, D., Egger, J. A., et al. 2023, *A&A*, 671, L8, doi: [10.1051/0004-6361/202245607](https://doi.org/10.1051/0004-6361/202245607)
- Bonfanti, A., Amateis, I., Gandolfi, D., et al. 2025, *A&A*, 693, A90, doi: [10.1051/0004-6361/202451300](https://doi.org/10.1051/0004-6361/202451300)
- Bonnefoy, M., Perraut, K., Lagrange, A. M., et al. 2018, *A&A*, 618, A63, doi: [10.1051/0004-6361/201832942](https://doi.org/10.1051/0004-6361/201832942)
- Bonomo, A. S., Hébrard, G., Raymond, S. N., et al. 2017, *A&A*, 603, A43, doi: [10.1051/0004-6361/201730624](https://doi.org/10.1051/0004-6361/201730624)
- Bonomo, A. S., Dumusque, X., Massa, A., et al. 2023, *A&A*, 677, A33, doi: [10.1051/0004-6361/202346211](https://doi.org/10.1051/0004-6361/202346211)
- Bordé, P., Bouchy, F., Deleuil, M., et al. 2010, *A&A*, 520, A66, doi: [10.1051/0004-6361/201014775](https://doi.org/10.1051/0004-6361/201014775)
- Borsato, L., Malavolta, L., Piotto, G., et al. 2019, *MNRAS*, 484, 3233, doi: [10.1093/mnras/stz181](https://doi.org/10.1093/mnras/stz181)
- Bouchy, F., Hebb, L., Skillen, I., et al. 2010, *A&A*, 519, A98, doi: [10.1051/0004-6361/201014817](https://doi.org/10.1051/0004-6361/201014817)
- Bouffleur, R. C., Emilio, M., Janot-Pacheco, E., et al. 2018, *MNRAS*, 473, 710, doi: [10.1093/mnras/stx2187](https://doi.org/10.1093/mnras/stx2187)
- Bourrier, V., Dumusque, X., Dorn, C., et al. 2018, *A&A*, 619, A1, doi: [10.1051/0004-6361/201833154](https://doi.org/10.1051/0004-6361/201833154)
- Brahm, R., Jordán, A., Bakos, G. Á., et al. 2016, *AJ*, 151, 89, doi: [10.3847/0004-6256/151/4/89](https://doi.org/10.3847/0004-6256/151/4/89)
- Brahm, R., Espinoza, N., Jordán, A., et al. 2018, *MNRAS*, 477, 2572, doi: [10.1093/mnras/sty795](https://doi.org/10.1093/mnras/sty795)
- Brahm, R., Ulmer-Moll, S., Hobson, M. J., et al. 2023, *AJ*, 165, 227, doi: [10.3847/1538-3881/accadd](https://doi.org/10.3847/1538-3881/accadd)
- Bressan, A., Marigo, P., Girardi, L., et al. 2012, *MNRAS*, 427, 127, doi: [10.1111/j.1365-2966.2012.21948.x](https://doi.org/10.1111/j.1365-2966.2012.21948.x)
- Brewer, J. M., & Fischer, D. A. 2018, *ApJS*, 237, 38, doi: [10.3847/1538-4365/aad501](https://doi.org/10.3847/1538-4365/aad501)
- Brewer, J. M., Fischer, D. A., Valenti, J. A., & Piskunov, N. 2016, *ApJS*, 225, 32, doi: [10.3847/0067-0049/225/2/32](https://doi.org/10.3847/0067-0049/225/2/32)
- Brinkman, C. L., Weiss, L. M., Huber, D., et al. 2025, *AJ*, 170, 109, doi: [10.3847/1538-3881/ade677](https://doi.org/10.3847/1538-3881/ade677)
- Brown, D. J. A., Collier Cameron, A., Díaz, R. F., et al. 2012, *ApJ*, 760, 139, doi: [10.1088/0004-637X/760/2/139](https://doi.org/10.1088/0004-637X/760/2/139)
- Brugamyer, E., Dodson-Robinson, S. E., Cochran, W. D., & Sneden, C. 2011, *ApJ*, 738, 97, doi: [10.1088/0004-637X/738/1/97](https://doi.org/10.1088/0004-637X/738/1/97)
- Bryant, E. M., Bayliss, D., Nielsen, L. D., et al. 2020, *MNRAS*, 499, 3139, doi: [10.1093/mnras/staa2976](https://doi.org/10.1093/mnras/staa2976)
- Buchhave, L. A., Bakos, G. Á., Hartman, J. D., et al. 2010, *ApJ*, 720, 1118, doi: [10.1088/0004-637X/720/2/1118](https://doi.org/10.1088/0004-637X/720/2/1118)
- Buchhave, L. A., Latham, D. W., Johansen, A., et al. 2012, *Nature*, 486, 375, doi: [10.1038/nature11121](https://doi.org/10.1038/nature11121)
- Buchhave, L. A., Bizzarro, M., Latham, D. W., et al. 2014, *Nature*, 509, 593, doi: [10.1038/nature13254](https://doi.org/10.1038/nature13254)

- Caffau, E., Bonifacio, P., Faraggiana, R., et al. 2005, *A&A*, 441, 533, doi: [10.1051/0004-6361:20052905](https://doi.org/10.1051/0004-6361:20052905)
- Caffau, E., Ludwig, H. G., Steffen, M., et al. 2008, *A&A*, 488, 1031, doi: [10.1051/0004-6361:200809885](https://doi.org/10.1051/0004-6361:200809885)
- Castelli, F., & Kurucz, R. L. 2003, in *IAU Symposium*, Vol. 210, *Modelling of Stellar Atmospheres*, ed. N. Piskunov, W. W. Weiss, & D. F. Gray, A20, doi: [10.48550/arXiv.astro-ph/0405087](https://doi.org/10.48550/arXiv.astro-ph/0405087)
- Castro-González, A., Lillo-Box, J., Armstrong, D. J., et al. 2024, *A&A*, 691, A233, doi: [10.1051/0004-6361/202451656](https://doi.org/10.1051/0004-6361/202451656)
- Chabrier, G. 2001, *ApJ*, 554, 1274, doi: [10.1086/321401](https://doi.org/10.1086/321401)
- Chakrabarty, A., & Sengupta, S. 2019, *AJ*, 158, 39, doi: [10.3847/1538-3881/ab24dd](https://doi.org/10.3847/1538-3881/ab24dd)
- Changeat, Q., Edwards, B., Al-Refai, A. F., et al. 2022, *ApJS*, 260, 3, doi: [10.3847/1538-4365/ac5cc2](https://doi.org/10.3847/1538-4365/ac5cc2)
- Chaturvedi, P., Goffo, E., Gandolfi, D., et al. 2025, *A&A*, 697, A169, doi: [10.1051/0004-6361/202453511](https://doi.org/10.1051/0004-6361/202453511)
- Chen, D.-C., Xie, J.-W., Zhou, J.-L., et al. 2021, *ApJ*, 909, 115, doi: [10.3847/1538-4357/abd5be](https://doi.org/10.3847/1538-4357/abd5be)
- Christiansen, J. L., Vanderburg, A., Burt, J., et al. 2017, *AJ*, 154, 122, doi: [10.3847/1538-3881/aa832d](https://doi.org/10.3847/1538-3881/aa832d)
- Ciceri, S., Mancini, L., Southworth, J., et al. 2016, *MNRAS*, 456, 990, doi: [10.1093/mnras/stv2698](https://doi.org/10.1093/mnras/stv2698)
- Cortés-Zuleta, P., Rojo, P., Wang, S., et al. 2020, *A&A*, 636, A98, doi: [10.1051/0004-6361/201936279](https://doi.org/10.1051/0004-6361/201936279)
- Cosentino, R., Lovis, C., Pepe, F., et al. 2012, in *Society of Photo-Optical Instrumentation Engineers (SPIE) Conference Series*, Vol. 8446, *Ground-based and Airborne Instrumentation for Astronomy IV*, ed. I. S. McLean, S. K. Ramsay, & H. Takami, 84461V, doi: [10.1117/12.925738](https://doi.org/10.1117/12.925738)
- Costa Silva, A. R., Delgado Mena, E., & Tsantaki, M. 2020, *A&A*, 634, A136, doi: [10.1051/0004-6361/201936523](https://doi.org/10.1051/0004-6361/201936523)
- Crossfield, I. J. M. 2023, *ApJL*, 952, L18, doi: [10.3847/2041-8213/ace35f](https://doi.org/10.3847/2041-8213/ace35f)
- Crouzet, N., McCullough, P. R., Burke, C., & Long, D. 2012, *ApJ*, 761, 7, doi: [10.1088/0004-637X/761/1/7](https://doi.org/10.1088/0004-637X/761/1/7)
- Cubas Armas, M., Asensio Ramos, A., & Socas-Navarro, H. 2020, *A&A*, 643, A142, doi: [10.1051/0004-6361/202037849](https://doi.org/10.1051/0004-6361/202037849)
- da Silva, L., Girardi, L., Pasquini, L., et al. 2006, *A&A*, 458, 609, doi: [10.1051/0004-6361:20065105](https://doi.org/10.1051/0004-6361:20065105)
- Dalba, P. A., Kane, S. R., Isaacson, H., et al. 2021, *AJ*, 161, 103, doi: [10.3847/1538-3881/abd408](https://doi.org/10.3847/1538-3881/abd408)
- . 2024, *ApJS*, 271, 16, doi: [10.3847/1538-4365/ad18c3](https://doi.org/10.3847/1538-4365/ad18c3)
- Dawson, R. I., & Johnson, J. A. 2018, *ARA&A*, 56, 175, doi: [10.1146/annurev-astro-081817-051853](https://doi.org/10.1146/annurev-astro-081817-051853)
- Dawson, R. I., & Murray-Clay, R. A. 2013, *ApJL*, 767, L24, doi: [10.1088/2041-8205/767/2/L24](https://doi.org/10.1088/2041-8205/767/2/L24)
- de Laverny, P., Ligi, R., Crida, A., Recio-Blanco, A., & Palicio, P. A. 2025, *A&A*, 699, A100, doi: [10.1051/0004-6361/202554739](https://doi.org/10.1051/0004-6361/202554739)
- Deeg, H. J., Moutou, C., Erikson, A., et al. 2010, *Nature*, 464, 384, doi: [10.1038/nature08856](https://doi.org/10.1038/nature08856)
- Delgado Mena, E., Adibekyan, V., Santos, N. C., et al. 2021, *A&A*, 655, A99, doi: [10.1051/0004-6361/202141588](https://doi.org/10.1051/0004-6361/202141588)
- Delrez, L., Ehrenreich, D., Alibert, Y., et al. 2021, *Nature Astronomy*, 5, 775, doi: [10.1038/s41550-021-01381-5](https://doi.org/10.1038/s41550-021-01381-5)
- Desidera, S., Damasso, M., Gratton, R., et al. 2023, *A&A*, 675, A158, doi: [10.1051/0004-6361/202244611](https://doi.org/10.1051/0004-6361/202244611)
- Díaz, M. R., Jenkins, J. S., Feng, F., et al. 2020, *MNRAS*, 496, 4330, doi: [10.1093/mnras/staa1724](https://doi.org/10.1093/mnras/staa1724)
- Doyle, L., Cegla, H. M., Anderson, D. R., et al. 2023, *MNRAS*, 522, 4499, doi: [10.1093/mnras/stad1240](https://doi.org/10.1093/mnras/stad1240)
- Dransfield, G., Triaud, A. H. M. J., Guillot, T., et al. 2022, *MNRAS*, 515, 1328, doi: [10.1093/mnras/stac1383](https://doi.org/10.1093/mnras/stac1383)
- Drimmel, R., Cabrera-Lavers, A., & López-Corrodoira, M. 2003, *A&A*, 409, 205, doi: [10.1051/0004-6361:20031070](https://doi.org/10.1051/0004-6361:20031070)
- Drażkowska, J., & Alibert, Y. 2017, *A&A*, 608, A92, doi: [10.1051/0004-6361/201731491](https://doi.org/10.1051/0004-6361/201731491)
- Eastman, J. D., Beatty, T. G., Siverd, R. J., et al. 2016, *AJ*, 151, 45, doi: [10.3847/0004-6256/151/2/45](https://doi.org/10.3847/0004-6256/151/2/45)
- Eberhardt, J., Trifonov, T., Henning, T., et al. 2025, *AJ*, 169, 298, doi: [10.3847/1538-3881/adc44e](https://doi.org/10.3847/1538-3881/adc44e)
- Ecuvillon, A., Israelian, G., Santos, N. C., et al. 2006, *A&A*, 445, 633, doi: [10.1051/0004-6361:20053469](https://doi.org/10.1051/0004-6361:20053469)
- Egger, J. A., Osborn, H. P., Kubyskhina, D., et al. 2024, *A&A*, 688, A223, doi: [10.1051/0004-6361/202450472](https://doi.org/10.1051/0004-6361/202450472)
- Ehlmann, B. L., Anderson, F. S., Andrews-Hanna, J., et al. 2016, *Journal of Geophysical Research (Planets)*, 121, 1927, doi: [10.1002/2016JE005134](https://doi.org/10.1002/2016JE005134)
- Ehrenreich, D., Lovis, C., Allart, R., et al. 2020, *Nature*, 580, 597, doi: [10.1038/s41586-020-2107-1](https://doi.org/10.1038/s41586-020-2107-1)
- Ellis, T. G., Boyajian, T., von Braun, K., et al. 2021, *AJ*, 162, 118, doi: [10.3847/1538-3881/ac141a](https://doi.org/10.3847/1538-3881/ac141a)
- Espinoza, N., Fortney, J. J., Miguel, Y., Thorngren, D., & Murray-Clay, R. 2017, *ApJL*, 838, L9, doi: [10.3847/2041-8213/aa65ca](https://doi.org/10.3847/2041-8213/aa65ca)
- Espinoza, N., Brahm, R., Henning, T., et al. 2020, *MNRAS*, 491, 2982, doi: [10.1093/mnras/stz3150](https://doi.org/10.1093/mnras/stz3150)
- European Southern Observatory (ESO). 2014, *HARPS reduced data obtained by standard ESO pipeline processing*, European Southern Observatory (ESO), doi: [10.18727/ARCHIVE/33](https://doi.org/10.18727/ARCHIVE/33)
- Fischer, D. A., & Valenti, J. 2005, *ApJ*, 622, 1102, doi: [10.1086/428383](https://doi.org/10.1086/428383)
- Frame, G., Armstrong, D. J., Cegla, H. M., et al. 2023, *MNRAS*, 523, 1163, doi: [10.1093/mnras/stad1452](https://doi.org/10.1093/mnras/stad1452)

- Fridlund, M., Livingston, J., Gandolfi, D., et al. 2020, MNRAS, 498, 4503, doi: [10.1093/mnras/staa2502](https://doi.org/10.1093/mnras/staa2502)
- Furlan, E., Ciardi, D. R., Cochran, W. D., et al. 2018, ApJ, 861, 149, doi: [10.3847/1538-4357/aaca34](https://doi.org/10.3847/1538-4357/aaca34)
- Gaia Collaboration, Brown, A. G. A., Vallenari, A., et al. 2016, A&A, 595, A2, doi: [10.1051/0004-6361/201629512](https://doi.org/10.1051/0004-6361/201629512)
- . 2018, A&A, 616, A1, doi: [10.1051/0004-6361/201833051](https://doi.org/10.1051/0004-6361/201833051)
- . 2021, A&A, 649, A1, doi: [10.1051/0004-6361/202039657](https://doi.org/10.1051/0004-6361/202039657)
- Gardner, J. P., Mather, J. C., Clampin, M., et al. 2006, SSRv, 123, 485, doi: [10.1007/s11214-006-8315-7](https://doi.org/10.1007/s11214-006-8315-7)
- Gardner, J. P., Mather, J. C., Abbott, R., et al. 2023, PASP, 135, 068001, doi: [10.1088/1538-3873/acd1b5](https://doi.org/10.1088/1538-3873/acd1b5)
- Georgieva, I. Y., Persson, C. M., Goffo, E., et al. 2023, A&A, 674, A117, doi: [10.1051/0004-6361/202345961](https://doi.org/10.1051/0004-6361/202345961)
- Ghezzi, L., Costa-Almeida, E., Loaiza-Tacuri, V., & Cunha, K. 2026, ApJ, 998, 301, doi: [10.3847/1538-4357/ae317d](https://doi.org/10.3847/1538-4357/ae317d)
- Ghezzi, L., Cunha, K., Smith, V. V., et al. 2010a, ApJ, 720, 1290, doi: [10.1088/0004-637X/720/2/1290](https://doi.org/10.1088/0004-637X/720/2/1290)
- Ghezzi, L., Cunha, K., Smith, V. V., & de la Reza, R. 2010b, ApJ, 724, 154, doi: [10.1088/0004-637X/724/1/154](https://doi.org/10.1088/0004-637X/724/1/154)
- Ghezzi, L., Cunha, K., Smith, V. V., et al. 2009, ApJ, 698, 451, doi: [10.1088/0004-637X/698/1/451](https://doi.org/10.1088/0004-637X/698/1/451)
- Ghezzi, L., Martinez, C. F., Wilson, R. F., et al. 2021, ApJ, 920, 19, doi: [10.3847/1538-4357/ac14c3](https://doi.org/10.3847/1538-4357/ac14c3)
- Ghezzi, L., Montet, B. T., & Johnson, J. A. 2018, ApJ, 860, 109, doi: [10.3847/1538-4357/aac37c](https://doi.org/10.3847/1538-4357/aac37c)
- Gill, S., Wheatley, P. J., Cooke, B. F., et al. 2020, ApJL, 898, L11, doi: [10.3847/2041-8213/ab9eb9](https://doi.org/10.3847/2041-8213/ab9eb9)
- Gill, S., Bayliss, D., Ulmer-Moll, S., et al. 2024, MNRAS, 533, 109, doi: [10.1093/mnras/stae1804](https://doi.org/10.1093/mnras/stae1804)
- Gillon, M., Smalley, B., Hebb, L., et al. 2009, A&A, 496, 259, doi: [10.1051/0004-6361:200810929](https://doi.org/10.1051/0004-6361:200810929)
- Gillon, M., Anderson, D. R., Collier-Cameron, A., et al. 2014, A&A, 562, L3, doi: [10.1051/0004-6361/201323014](https://doi.org/10.1051/0004-6361/201323014)
- Gonzalez, G. 1997, MNRAS, 285, 403, doi: [10.1093/mnras/285.2.403](https://doi.org/10.1093/mnras/285.2.403)
- Green, G. M., Schlafly, E., Zucker, C., Speagle, J. S., & Finkbeiner, D. 2019, ApJ, 887, 93, doi: [10.3847/1538-4357/ab5362](https://doi.org/10.3847/1538-4357/ab5362)
- Gressier, A., Batalha, N. E., Wogan, N., et al. 2025, AJ, 170, 292, doi: [10.3847/1538-3881/ae0929](https://doi.org/10.3847/1538-3881/ae0929)
- Grieves, N., Bouchy, F., Ulmer-Moll, S., et al. 2022, A&A, 668, A29, doi: [10.1051/0004-6361/202244077](https://doi.org/10.1051/0004-6361/202244077)
- Grziwa, S., Gandolfi, D., Csizmadia, S., et al. 2016, AJ, 152, 132, doi: [10.3847/0004-6256/152/5/132](https://doi.org/10.3847/0004-6256/152/5/132)
- Guenther, E. W., Goffo, E., Sebastian, D., et al. 2024, MNRAS, 529, 141, doi: [10.1093/mnras/stae494](https://doi.org/10.1093/mnras/stae494)
- Hacker, A., Díaz, R. F., Armstrong, D. J., et al. 2024, MNRAS, 532, 1612, doi: [10.1093/mnras/stae1420](https://doi.org/10.1093/mnras/stae1420)
- Hartman, J. D., Bakos, G. Á., Kipping, D. M., et al. 2011, ApJ, 728, 138, doi: [10.1088/0004-637X/728/2/138](https://doi.org/10.1088/0004-637X/728/2/138)
- Hartman, J. D., Bakos, G. Á., Torres, G., et al. 2014, AJ, 147, 128, doi: [10.1088/0004-6256/147/6/128](https://doi.org/10.1088/0004-6256/147/6/128)
- Hawthorn, F., Bayliss, D., Armstrong, D. J., et al. 2023, MNRAS, 524, 3877, doi: [10.1093/mnras/stad1840](https://doi.org/10.1093/mnras/stad1840)
- Hébrard, G., Collier Cameron, A., Brown, D. J. A., et al. 2013, A&A, 549, A134, doi: [10.1051/0004-6361/201220363](https://doi.org/10.1051/0004-6361/201220363)
- Heidari, N., Hébrard, G., Martioli, E., et al. 2025, A&A, 694, A36, doi: [10.1051/0004-6361/202451519](https://doi.org/10.1051/0004-6361/202451519)
- Hellier, C., Anderson, D. R., Collier Cameron, A., et al. 2015, AJ, 150, 18, doi: [10.1088/0004-6256/150/1/18](https://doi.org/10.1088/0004-6256/150/1/18)
- . 2017, MNRAS, 465, 3693, doi: [10.1093/mnras/stw3005](https://doi.org/10.1093/mnras/stw3005)
- Hellier, C., Anderson, D. R., Bouchy, F., et al. 2019, MNRAS, 482, 1379, doi: [10.1093/mnras/sty2741](https://doi.org/10.1093/mnras/sty2741)
- Hinkel, N. R., Timmes, F. X., Young, P. A., Pagano, M. D., & Turnbull, M. C. 2014, AJ, 148, 54, doi: [10.1088/0004-6256/148/3/54](https://doi.org/10.1088/0004-6256/148/3/54)
- Hinkel, N. R., & Unterborn, C. T. 2018, ApJ, 853, 83, doi: [10.3847/1538-4357/aaa5b4](https://doi.org/10.3847/1538-4357/aaa5b4)
- Hobson, M. J., Trifonov, T., Henning, T., et al. 2023, AJ, 166, 201, doi: [10.3847/1538-3881/acfc1d](https://doi.org/10.3847/1538-3881/acfc1d)
- Hobson, M. J., Bouchy, F., Lavie, B., et al. 2024, A&A, 688, A216, doi: [10.1051/0004-6361/202450505](https://doi.org/10.1051/0004-6361/202450505)
- Hoch, K. K. W., Konopacky, Q. M., Theissen, C. A., et al. 2023, AJ, 166, 85, doi: [10.3847/1538-3881/ace442](https://doi.org/10.3847/1538-3881/ace442)
- Howard, A. W., Sinukoff, E., Blunt, S., et al. 2025, ApJS, 278, 52, doi: [10.3847/1538-4365/adc5e4](https://doi.org/10.3847/1538-4365/adc5e4)
- Hoyer, S., Gandolfi, D., Armstrong, D. J., et al. 2021, MNRAS, 505, 3361, doi: [10.1093/mnras/stab1427](https://doi.org/10.1093/mnras/stab1427)
- Huber, D., Zinn, J., Bojsen-Hansen, M., et al. 2017, ApJ, 844, 102, doi: [10.3847/1538-4357/aa75ca](https://doi.org/10.3847/1538-4357/aa75ca)
- Ida, S., & Lin, D. N. C. 2004, ApJ, 604, 388, doi: [10.1086/381724](https://doi.org/10.1086/381724)
- . 2008, ApJ, 673, 487, doi: [10.1086/523754](https://doi.org/10.1086/523754)
- Izidoro, A., Ogihara, M., Raymond, S. N., et al. 2017, MNRAS, 470, 1750, doi: [10.1093/mnras/stx1232](https://doi.org/10.1093/mnras/stx1232)
- Jenkins, J. S., Díaz, M. R., Kurtovic, N. T., et al. 2020, Nature Astronomy, 4, 1148, doi: [10.1038/s41550-020-1142-z](https://doi.org/10.1038/s41550-020-1142-z)
- Johansson, S., Litzén, U., Lundberg, H., & Zhang, Z. 2003, ApJL, 584, L107, doi: [10.1086/374037](https://doi.org/10.1086/374037)
- Johnson, M. C., Gandolfi, D., Fridlund, M., et al. 2016, AJ, 151, 171, doi: [10.3847/0004-6256/151/6/171](https://doi.org/10.3847/0004-6256/151/6/171)
- Jones, M. I., Reinartz, Y., Brahm, R., et al. 2024, A&A, 683, A192, doi: [10.1051/0004-6361/202348147](https://doi.org/10.1051/0004-6361/202348147)
- Jordán, A., Bakos, G. Á., Bayliss, D., et al. 2020, AJ, 160, 222, doi: [10.3847/1538-3881/aba530](https://doi.org/10.3847/1538-3881/aba530)

- Kabáth, P., Chaturvedi, P., MacQueen, P. J., et al. 2022, *MNRAS*, 513, 5955, doi: [10.1093/mnras/stac1254](https://doi.org/10.1093/mnras/stac1254)
- Kama, M., Shorttle, O., Jermyn, A. S., et al. 2019, *ApJ*, 885, 114, doi: [10.3847/1538-4357/ab45f8](https://doi.org/10.3847/1538-4357/ab45f8)
- Kane, S. R., Hill, M. L., Dalba, P. A., et al. 2023, *AJ*, 165, 252, doi: [10.3847/1538-3881/acd17a](https://doi.org/10.3847/1538-3881/acd17a)
- Kirby, E. N., Xie, J. L., Guo, R., Kovalev, M., & Bergemann, M. 2018, *ApJS*, 237, 18, doi: [10.3847/1538-4365/aac952](https://doi.org/10.3847/1538-4365/aac952)
- Konopacky, Q. M., Barman, T. S., Macintosh, B. A., & Marois, C. 2013, *Science*, 339, 1398, doi: [10.1126/science.1232003](https://doi.org/10.1126/science.1232003)
- Kosiarek, M. R., Blunt, S., López-Morales, M., et al. 2019, *AJ*, 157, 116, doi: [10.3847/1538-3881/aafe83](https://doi.org/10.3847/1538-3881/aafe83)
- Krenn, A. F., Kubyshkina, D., Fossati, L., et al. 2024, *A&A*, 686, A301, doi: [10.1051/0004-6361/202348584](https://doi.org/10.1051/0004-6361/202348584)
- Krijt, S., Kama, M., McClure, M., et al. 2023, in *Astronomical Society of the Pacific Conference Series*, Vol. 534, *Protostars and Planets VII*, ed. S. Inutsuka, Y. Aikawa, T. Muto, K. Tomida, & M. Tamura, 1031, doi: [10.48550/arXiv.2203.10056](https://doi.org/10.48550/arXiv.2203.10056)
- Kruse, E., Agol, E., Luger, R., & Foreman-Mackey, D. 2019, *ApJS*, 244, 11, doi: [10.3847/1538-4365/ab346b](https://doi.org/10.3847/1538-4365/ab346b)
- Kuhn, R. B., Rodriguez, J. E., Collins, K. A., et al. 2016, *MNRAS*, 459, 4281, doi: [10.1093/mnras/stw880](https://doi.org/10.1093/mnras/stw880)
- Lambert, D. L. 1978, *MNRAS*, 182, 249, doi: [10.1093/mnras/182.2.249](https://doi.org/10.1093/mnras/182.2.249)
- Leemker, M., Facchini, S., Curone, P., et al. 2026, *A&A*, 705, A193, doi: [10.1051/0004-6361/202557609](https://doi.org/10.1051/0004-6361/202557609)
- Li, C., Allison, M., Atreya, S., et al. 2024, *Icarus*, 414, 116028, doi: [10.1016/j.icarus.2024.116028](https://doi.org/10.1016/j.icarus.2024.116028)
- Lillo-Box, J., Lopez, T. A., Santerne, A., et al. 2020, *A&A*, 640, A48, doi: [10.1051/0004-6361/202037896](https://doi.org/10.1051/0004-6361/202037896)
- Limongi, M., & Chieffi, A. 2003, *Memorie della Societa Astronomica Italiana Supplementi*, 3, 58
- Livingston, J. H., Endl, M., Dai, F., et al. 2018, *AJ*, 156, 78, doi: [10.3847/1538-3881/aaccde](https://doi.org/10.3847/1538-3881/aaccde)
- Livingston, J. H., Gandolfi, D., Trani, A. A., et al. 2024, *Scientific Reports*, 14, 27219, doi: [10.1038/s41598-024-76490-y](https://doi.org/10.1038/s41598-024-76490-y)
- Loaiza-Tacuri, V., Cunha, K., Smith, V. V., et al. 2024, *ApJ*, 970, 53, doi: [10.3847/1538-4357/ad4b15](https://doi.org/10.3847/1538-4357/ad4b15)
- Loaiza-Tacuri, V., Souto, D., Quispe-Huaynasi, F., et al. 2025, *ApJS*, 281, 61, doi: [10.3847/1538-4365/ae14f9](https://doi.org/10.3847/1538-4365/ae14f9)
- Lockley, I. S., Armstrong, D. J., Fernández Fernández, J., et al. 2025, *MNRAS*, 541, 919, doi: [10.1093/mnras/staf939](https://doi.org/10.1093/mnras/staf939)
- Lodders, K. 2004, *ApJ*, 611, 587, doi: [10.1086/421970](https://doi.org/10.1086/421970)
- Lodders, K., Bergemann, M., & Palme, H. 2025, *SSRv*, 221, 23, doi: [10.1007/s11214-025-01146-w](https://doi.org/10.1007/s11214-025-01146-w)
- Lopez, T. A., Barros, S. C. C., Santerne, A., et al. 2019, *A&A*, 631, A90, doi: [10.1051/0004-6361/201936267](https://doi.org/10.1051/0004-6361/201936267)
- Luck, R. E. 2015, *AJ*, 150, 88, doi: [10.1088/0004-6256/150/3/88](https://doi.org/10.1088/0004-6256/150/3/88)
- Luck, R. E., & Heiter, U. 2005, *AJ*, 129, 1063, doi: [10.1086/427250](https://doi.org/10.1086/427250)
- . 2006, *AJ*, 131, 3069, doi: [10.1086/504080](https://doi.org/10.1086/504080)
- Maciejewski, G., Golonka, J., Loboda, W., et al. 2023, *MNRAS*, 525, L43, doi: [10.1093/mnras/sladd078](https://doi.org/10.1093/mnras/sladd078)
- Maciejewski, G., Ohlert, J., Dimitrov, D., et al. 2014, *AcA*, 64, 11, doi: [10.48550/arXiv.1402.6518](https://doi.org/10.48550/arXiv.1402.6518)
- Madhusudhan, N. 2012, *ApJ*, 758, 36, doi: [10.1088/0004-637X/758/1/36](https://doi.org/10.1088/0004-637X/758/1/36)
- . 2019, *ARA&A*, 57, 617, doi: [10.1146/annurev-astro-081817-051846](https://doi.org/10.1146/annurev-astro-081817-051846)
- Magrini, L., Danielski, C., Bossini, D., et al. 2022, *A&A*, 663, A161, doi: [10.1051/0004-6361/202243405](https://doi.org/10.1051/0004-6361/202243405)
- Majewski, S. R., Schiavon, R. P., Frinchaboy, P. M., et al. 2017, *AJ*, 154, 94, doi: [10.3847/1538-3881/aa784d](https://doi.org/10.3847/1538-3881/aa784d)
- Mancini, L., Kemmer, J., Southworth, J., et al. 2016, *MNRAS*, 459, 1393, doi: [10.1093/mnras/stw659](https://doi.org/10.1093/mnras/stw659)
- Mancini, L., Esposito, M., Covino, E., et al. 2018, *A&A*, 613, A41, doi: [10.1051/0004-6361/201732234](https://doi.org/10.1051/0004-6361/201732234)
- Manni, F., Naponiello, L., Mancini, L., et al. 2025, *A&A*, 701, A230, doi: [10.1051/0004-6361/202556081](https://doi.org/10.1051/0004-6361/202556081)
- Mantovan, G., Malavolta, L., Desidera, S., et al. 2024a, *A&A*, 682, A129, doi: [10.1051/0004-6361/202347472](https://doi.org/10.1051/0004-6361/202347472)
- Mantovan, G., Wilson, T. G., Borsato, L., et al. 2024b, *A&A*, 691, A67, doi: [10.1051/0004-6361/202451841](https://doi.org/10.1051/0004-6361/202451841)
- Martinez, C. F., Cunha, K., Ghezzi, L., & Smith, V. V. 2019, *ApJ*, 875, 29, doi: [10.3847/1538-4357/ab0d93](https://doi.org/10.3847/1538-4357/ab0d93)
- Mathur, D., & Becker, J. 2025, *PASP*, 137, 114402, doi: [10.1088/1538-3873/ae135a](https://doi.org/10.1088/1538-3873/ae135a)
- Matrozos, E., Ryde, N., & Dupree, A. K. 2013, *A&A*, 559, A115, doi: [10.1051/0004-6361/201322317](https://doi.org/10.1051/0004-6361/201322317)
- Matsuno, T., Starkenburg, E., Balbinot, E., & Helmi, A. 2024, *A&A*, 685, A59, doi: [10.1051/0004-6361/202245762](https://doi.org/10.1051/0004-6361/202245762)
- Matteucci, F. 2016, in *Journal of Physics Conference Series*, Vol. 703, *Journal of Physics Conference Series*, 012004, doi: [10.1088/1742-6596/703/1/012004](https://doi.org/10.1088/1742-6596/703/1/012004)
- Maxted, P. F. L., Anderson, D. R., Collier Cameron, A., et al. 2016, *A&A*, 591, A55, doi: [10.1051/0004-6361/201628250](https://doi.org/10.1051/0004-6361/201628250)
- Mayor, M., & Queloz, D. 1995, *Nature*, 378, 355, doi: [10.1038/378355a0](https://doi.org/10.1038/378355a0)
- Mayor, M., Pepe, F., Queloz, D., et al. 2003, *The Messenger*, 114, 20
- McGruder, C. D., López-Morales, M., Brahm, R., & Jordán, A. 2023, *ApJL*, 944, L56, doi: [10.3847/2041-8213/acb154](https://doi.org/10.3847/2041-8213/acb154)

- McQuillan, A., Mazeh, T., & Aigrain, S. 2013, *ApJL*, 775, L11, doi: [10.1088/2041-8205/775/1/L11](https://doi.org/10.1088/2041-8205/775/1/L11)
- Méndez, A., Rivera-Valentín, E. G., Schulze-Makuch, D., et al. 2021, *Astrobiology*, 21, 1017, doi: [10.1089/ast.2020.2342](https://doi.org/10.1089/ast.2020.2342)
- Mills, S. M., Howard, A. W., Weiss, L. M., et al. 2019, *AJ*, 157, 145, doi: [10.3847/1538-3881/ab0899](https://doi.org/10.3847/1538-3881/ab0899)
- Mishurov, Y. N., & Tkachenko, R. V. 2019, *MNRAS*, 485, 2225, doi: [10.1093/mnras/stz526](https://doi.org/10.1093/mnras/stz526)
- Moore, C. E. 1945, *Contributions from the Princeton University Observatory*, 20, 1
- Mortier, A., Santos, N. C., Sousa, S. G., et al. 2013, *A&A*, 557, A70, doi: [10.1051/0004-6361/201321641](https://doi.org/10.1051/0004-6361/201321641)
- Moses, J. I., Madhusudhan, N., Visscher, C., & Freedman, R. S. 2013, *ApJ*, 763, 25, doi: [10.1088/0004-637X/763/1/25](https://doi.org/10.1088/0004-637X/763/1/25)
- Moutou, C., Bruntt, H., Guillot, T., et al. 2008, *A&A*, 488, L47, doi: [10.1051/0004-6361:200810273](https://doi.org/10.1051/0004-6361:200810273)
- Mulders, G. D., Pascucci, I., Apai, D., Frasca, A., & Molenda-Żakowicz, J. 2016, *AJ*, 152, 187, doi: [10.3847/0004-6256/152/6/187](https://doi.org/10.3847/0004-6256/152/6/187)
- Mullally, F., Coughlin, J. L., Thompson, S. E., et al. 2015, *ApJS*, 217, 31, doi: [10.1088/0067-0049/217/2/31](https://doi.org/10.1088/0067-0049/217/2/31)
- Muresan, A., Persson, C. M., & Fridlund, M. 2026, *A&A*, 707, A355, doi: [10.1051/0004-6361/202557468](https://doi.org/10.1051/0004-6361/202557468)
- Murgas, F., Nowak, G., Masseron, T., et al. 2022, *A&A*, 668, A158, doi: [10.1051/0004-6361/202244459](https://doi.org/10.1051/0004-6361/202244459)
- Murphy, M. M., Beatty, T. G., Welbanks, L., & Fu, G. 2025, *AJ*, 169, 286, doi: [10.3847/1538-3881/adc684](https://doi.org/10.3847/1538-3881/adc684)
- Nabbie, E., Huang, C. X., Burt, J. A., et al. 2024, *AJ*, 168, 132, doi: [10.3847/1538-3881/ad60be](https://doi.org/10.3847/1538-3881/ad60be)
- NASA Exoplanet Archive. 2025, *Planetary Systems*, Version: 2025-11-30 10:44, NExSci-Caltech/IPAC, doi: [10.26133/NEA12](https://doi.org/10.26133/NEA12)
- Nascimbeni, V., Borsato, L., Zingales, T., et al. 2023, *A&A*, 673, A42, doi: [10.1051/0004-6361/202245486](https://doi.org/10.1051/0004-6361/202245486)
- Nicholson, B. A., Aigrain, S., Eisner, N. L., et al. 2024, *MNRAS*, 532, 4632, doi: [10.1093/mnras/stae1821](https://doi.org/10.1093/mnras/stae1821)
- Nielsen, L. D., Bouchy, F., Turner, O. D., et al. 2019, *MNRAS*, 489, 2478, doi: [10.1093/mnras/stz2351](https://doi.org/10.1093/mnras/stz2351)
- Nielsen, L. D., Gandolfi, D., Armstrong, D. J., et al. 2020, *MNRAS*, 492, 5399, doi: [10.1093/mnras/staa197](https://doi.org/10.1093/mnras/staa197)
- Nikolov, N., Sing, D. K., Pont, F., et al. 2014, *MNRAS*, 437, 46, doi: [10.1093/mnras/stt1859](https://doi.org/10.1093/mnras/stt1859)
- Nissen, P. E. 2013, *A&A*, 552, A73, doi: [10.1051/0004-6361/201321234](https://doi.org/10.1051/0004-6361/201321234)
- Noguer, F. R., Corley, S., Pearson, K. A., et al. 2024, *PASP*, 136, 064401, doi: [10.1088/1538-3873/ad57f5](https://doi.org/10.1088/1538-3873/ad57f5)
- Öberg, K. I., Murray-Clay, R., & Bergin, E. A. 2011, *ApJL*, 743, L16, doi: [10.1088/2041-8205/743/1/L16](https://doi.org/10.1088/2041-8205/743/1/L16)
- Ochsenbein, F., Bauer, P., & Marcout, J. 2000, *A&AS*, 143, 23, doi: [10.1051/aas:2000169](https://doi.org/10.1051/aas:2000169)
- Ohno, K., & Fortney, J. J. 2023, *ApJ*, 956, 125, doi: [10.3847/1538-4357/ace531](https://doi.org/10.3847/1538-4357/ace531)
- Oka, A., Nakamoto, T., & Ida, S. 2011, *ApJ*, 738, 141, doi: [10.1088/0004-637X/738/2/141](https://doi.org/10.1088/0004-637X/738/2/141)
- Orell-Miquel, J., Nowak, G., Murgas, F., et al. 2023, *A&A*, 669, A40, doi: [10.1051/0004-6361/202244120](https://doi.org/10.1051/0004-6361/202244120)
- Osborn, A., Armstrong, D. J., Fernández Fernández, J., et al. 2023, *MNRAS*, 526, 548, doi: [10.1093/mnras/stad2575](https://doi.org/10.1093/mnras/stad2575)
- Osborn, H. P., Armstrong, D. J., Adibekyan, V., et al. 2021, *MNRAS*, 502, 4842, doi: [10.1093/mnras/stab182](https://doi.org/10.1093/mnras/stab182)
- Otegi, J. F., Bouchy, F., Helled, R., et al. 2021, *A&A*, 653, A105, doi: [10.1051/0004-6361/202040247](https://doi.org/10.1051/0004-6361/202040247)
- Pacetti, E., Turrini, D., Schisano, E., et al. 2022, *ApJ*, 937, 36, doi: [10.3847/1538-4357/ac8b11](https://doi.org/10.3847/1538-4357/ac8b11)
- Palle, E., Nowak, G., Luque, R., et al. 2019, *A&A*, 623, A41, doi: [10.1051/0004-6361/201834001](https://doi.org/10.1051/0004-6361/201834001)
- Pan, M., Liu, B., Jiang, L., et al. 2025, *ApJ*, 985, 7, doi: [10.3847/1538-4357/adc7a9](https://doi.org/10.3847/1538-4357/adc7a9)
- Perdigon, J., de Laverny, P., Recio-Blanco, A., et al. 2021, *A&A*, 647, A162, doi: [10.1051/0004-6361/202040147](https://doi.org/10.1051/0004-6361/202040147)
- Persson, C. M., Georgieva, I. Y., Gandolfi, D., et al. 2022, *A&A*, 666, A184, doi: [10.1051/0004-6361/202244118](https://doi.org/10.1051/0004-6361/202244118)
- Petigura, E. A., Howard, A. W., Marcy, G. W., et al. 2017, *AJ*, 154, 107, doi: [10.3847/1538-3881/aa80de](https://doi.org/10.3847/1538-3881/aa80de)
- Petigura, E. A., Crossfield, I. J. M., Isaacson, H., et al. 2018a, *AJ*, 155, 21, doi: [10.3847/1538-3881/aa9b83](https://doi.org/10.3847/1538-3881/aa9b83)
- Petigura, E. A., Marcy, G. W., Winn, J. N., et al. 2018b, *AJ*, 155, 89, doi: [10.3847/1538-3881/aaa54c](https://doi.org/10.3847/1538-3881/aaa54c)
- Petigura, E. A., Livingston, J., Batygin, K., et al. 2020, *AJ*, 159, 2, doi: [10.3847/1538-3881/ab5220](https://doi.org/10.3847/1538-3881/ab5220)
- Plotnikova, A., Spina, L., Ratcliffe, B., Casali, G., & Carraro, G. 2024, *A&A*, 691, A298, doi: [10.1051/0004-6361/202451167](https://doi.org/10.1051/0004-6361/202451167)
- Polanski, A. S., Lubin, J., Beard, C., et al. 2024, *ApJS*, 272, 32, doi: [10.3847/1538-4365/ad4484](https://doi.org/10.3847/1538-4365/ad4484)
- Pollack, J. B., Hubickyj, O., Bodenheimer, P., et al. 1996, *Icarus*, 124, 62, doi: [10.1006/icar.1996.0190](https://doi.org/10.1006/icar.1996.0190)
- Polman, J., Waters, L. B. F. M., Min, M., Miguel, Y., & Khorshid, N. 2023, *A&A*, 670, A161, doi: [10.1051/0004-6361/202244647](https://doi.org/10.1051/0004-6361/202244647)
- Pope, B. J. S., Parviainen, H., & Aigrain, S. 2016, *MNRAS*, 461, 3399, doi: [10.1093/mnras/stw1373](https://doi.org/10.1093/mnras/stw1373)
- Psaridi, A., Bouchy, F., Lendl, M., et al. 2023, *A&A*, 675, A39, doi: [10.1051/0004-6361/202346406](https://doi.org/10.1051/0004-6361/202346406)
- Queiroz, A. B. A., Anders, F., Santiago, B. X., et al. 2018, *MNRAS*, 476, 2556, doi: [10.1093/mnras/sty330](https://doi.org/10.1093/mnras/sty330)

- Ramírez, I., Meléndez, J., Bean, J., et al. 2014, *A&A*, 572, A48, doi: [10.1051/0004-6361/201424244](https://doi.org/10.1051/0004-6361/201424244)
- Rauer, H., Queloz, D., Csizmadia, S., et al. 2009, *A&A*, 506, 281, doi: [10.1051/0004-6361/200911902](https://doi.org/10.1051/0004-6361/200911902)
- Rice, M., Wang, X.-Y., Wang, S., et al. 2023, *AJ*, 166, 266, doi: [10.3847/1538-3881/ad09de](https://doi.org/10.3847/1538-3881/ad09de)
- Robinson, S. E., Laughlin, G., Bodenheimer, P., & Fischer, D. 2006, *ApJ*, 643, 484, doi: [10.1086/502795](https://doi.org/10.1086/502795)
- Rodríguez, J. E., Quinn, S. N., Zhou, G., et al. 2021, *AJ*, 161, 194, doi: [10.3847/1538-3881/abe38a](https://doi.org/10.3847/1538-3881/abe38a)
- Rodríguez Martínez, R., Eastman, J. D., Collins, K. A., et al. 2025, *AJ*, 169, 72, doi: [10.3847/1538-3881/ad9b90](https://doi.org/10.3847/1538-3881/ad9b90)
- Rosário, N. M., Demangeon, O. D. S., Barros, S. C. C., et al. 2024, *A&A*, 686, A282, doi: [10.1051/0004-6361/202347759](https://doi.org/10.1051/0004-6361/202347759)
- Ryabchikova, T., Piskunov, N., Kurucz, R. L., et al. 2015, *PhyS*, 90, 054005, doi: [10.1088/0031-8949/90/5/054005](https://doi.org/10.1088/0031-8949/90/5/054005)
- Santerne, A., Hébrard, G., Lillo-Box, J., et al. 2016, *ApJ*, 824, 55, doi: [10.3847/0004-637X/824/1/55](https://doi.org/10.3847/0004-637X/824/1/55)
- Santos, N. C., Israelian, G., & Mayor, M. 2000, *A&A*, 363, 228, doi: [10.48550/arXiv.astro-ph/0009182](https://doi.org/10.48550/arXiv.astro-ph/0009182)
- Schneider, A. D., & Bitsch, B. 2021a, *A&A*, 654, A71, doi: [10.1051/0004-6361/202039640](https://doi.org/10.1051/0004-6361/202039640)
- . 2021b, *A&A*, 654, A72, doi: [10.1051/0004-6361/202141096](https://doi.org/10.1051/0004-6361/202141096)
- . 2022, How drifting and evaporating pebbles shape giant planets (Corrigendum), *Astronomy & Astrophysics*, Volume 659, id.C3, 3 pp., doi: [10.1051/0004-6361/202141096](https://doi.org/10.1051/0004-6361/202141096)
- Schulte, J., Rodríguez, J. E., Latham, D. W., et al. 2025, *MNRAS*, 543, 292, doi: [10.1093/mnras/staf1455](https://doi.org/10.1093/mnras/staf1455)
- Seager, S., & Mallén-Ornelas, G. 2003, *ApJ*, 585, 1038, doi: [10.1086/346105](https://doi.org/10.1086/346105)
- Seager, S., Richardson, L. J., Hansen, B. M. S., et al. 2005, *ApJ*, 632, 1122, doi: [10.1086/444411](https://doi.org/10.1086/444411)
- Seidel, J. V., Lendl, M., Bourrier, V., et al. 2020, *A&A*, 643, A45, doi: [10.1051/0004-6361/202039058](https://doi.org/10.1051/0004-6361/202039058)
- Sha, L., Huang, C. X., Shporer, A., et al. 2021, *AJ*, 161, 82, doi: [10.3847/1538-3881/abd187](https://doi.org/10.3847/1538-3881/abd187)
- Sha, L., Vanderburg, A. M., Huang, C. X., et al. 2023, *MNRAS*, 524, 1113, doi: [10.1093/mnras/stad1666](https://doi.org/10.1093/mnras/stad1666)
- Sharma, A., Stonkutė, E., Drazdauska, A., et al. 2024, *A&A*, 691, A160, doi: [10.1051/0004-6361/202451889](https://doi.org/10.1051/0004-6361/202451889)
- Shaw, D. E., Weiss, L. M., Agol, E., et al. 2025, *AJ*, 170, 146, doi: [10.3847/1538-3881/ade67b](https://doi.org/10.3847/1538-3881/ade67b)
- Shields, A. L. 2019, *ApJS*, 243, 30, doi: [10.3847/1538-4365/ab2fe7](https://doi.org/10.3847/1538-4365/ab2fe7)
- Smith, A. M. S. 2015, *AcA*, 65, 117, doi: [10.48550/arXiv.1412.0451](https://doi.org/10.48550/arXiv.1412.0451)
- Smith, A. M. S., Acton, J. S., Anderson, D. R., et al. 2021, *A&A*, 646, A183, doi: [10.1051/0004-6361/202039712](https://doi.org/10.1051/0004-6361/202039712)
- Snedden, C. A. 1973, PhD thesis, University of Texas, Austin
- Soubiran, C., Brouillet, N., & Casamiquela, L. 2022, *A&A*, 663, A4, doi: [10.1051/0004-6361/202142409](https://doi.org/10.1051/0004-6361/202142409)
- Soubiran, C., Le Campion, J.-F., Brouillet, N., & Chemin, L. 2016, *A&A*, 591, A118, doi: [10.1051/0004-6361/201628497](https://doi.org/10.1051/0004-6361/201628497)
- Sousa, S. G., Santos, N. C., Adibekyan, V., Delgado-Mena, E., & Israelian, G. 2015, *A&A*, 577, A67, doi: [10.1051/0004-6361/201425463](https://doi.org/10.1051/0004-6361/201425463)
- Sousa, S. G., Santos, N. C., Israelian, G., Mayor, M., & Monteiro, M. J. P. F. G. 2007, *A&A*, 469, 783, doi: [10.1051/0004-6361:20077288](https://doi.org/10.1051/0004-6361:20077288)
- Sousa, S. G., Santos, N. C., Israelian, G., Mayor, M., & Udry, S. 2011, *A&A*, 533, A141, doi: [10.1051/0004-6361/201117699](https://doi.org/10.1051/0004-6361/201117699)
- Southworth, J., Mancini, L., Tregloan-Reed, J., et al. 2015, *MNRAS*, 454, 3094, doi: [10.1093/mnras/stv2183](https://doi.org/10.1093/mnras/stv2183)
- Southworth, J., Tregloan-Reed, J., Andersen, M. I., et al. 2016, *MNRAS*, 457, 4205, doi: [10.1093/mnras/stw279](https://doi.org/10.1093/mnras/stw279)
- Sozzetti, A., Damasso, M., Bonomo, A. S., et al. 2021, *A&A*, 648, A75, doi: [10.1051/0004-6361/202040034](https://doi.org/10.1051/0004-6361/202040034)
- Spite, M., Caffau, E., Andrievsky, S. M., et al. 2011, *A&A*, 528, A9, doi: [10.1051/0004-6361/201015926](https://doi.org/10.1051/0004-6361/201015926)
- Stassun, K. G., Collins, K. A., & Gaudi, B. S. 2017, *AJ*, 153, 136, doi: [10.3847/1538-3881/aa5df3](https://doi.org/10.3847/1538-3881/aa5df3)
- Steffen, M., Prakašavičius, D., Caffau, E., et al. 2015, *A&A*, 583, A57, doi: [10.1051/0004-6361/201526406](https://doi.org/10.1051/0004-6361/201526406)
- Suárez-Andrés, L., Israelian, G., González Hernández, J. I., et al. 2018, *A&A*, 614, A84, doi: [10.1051/0004-6361/201730743](https://doi.org/10.1051/0004-6361/201730743)
- Takada-Hidai, M., Takeda, Y., Sato, S., et al. 2002, *ApJ*, 573, 614, doi: [10.1086/340748](https://doi.org/10.1086/340748)
- Takeda, Y., Omiya, M., Harakawa, H., & Sato, B. 2016, *PASJ*, 68, 81, doi: [10.1093/pasj/psw071](https://doi.org/10.1093/pasj/psw071)
- Tala Pinto, M., Jordán, A., Acuña, L., et al. 2025, *A&A*, 694, A268, doi: [10.1051/0004-6361/202452517](https://doi.org/10.1051/0004-6361/202452517)
- Teske, J., Díaz, M. R., Luque, R., et al. 2020, *AJ*, 160, 96, doi: [10.3847/1538-3881/ab9f95](https://doi.org/10.3847/1538-3881/ab9f95)
- Teske, J. K. 2024, *ARA&A*, 62, 333, doi: [10.1146/annurev-astro-071221-053007](https://doi.org/10.1146/annurev-astro-071221-053007)
- Teske, J. K., Cunha, K., Smith, V. V., Schuler, S. C., & Griffith, C. A. 2014, *ApJ*, 788, 39, doi: [10.1088/0004-637X/788/1/39](https://doi.org/10.1088/0004-637X/788/1/39)
- Teske, J. K., Schuler, S. C., Cunha, K., Smith, V. V., & Griffith, C. A. 2013, *ApJL*, 768, L12, doi: [10.1088/2041-8205/768/1/L12](https://doi.org/10.1088/2041-8205/768/1/L12)

- Thiabaud, A., Marboeuf, U., Alibert, Y., Leya, I., & Mezger, K. 2015a, *A&A*, 574, A138, doi: [10.1051/0004-6361/201424868](https://doi.org/10.1051/0004-6361/201424868)
- . 2015b, *A&A*, 580, A30, doi: [10.1051/0004-6361/201525963](https://doi.org/10.1051/0004-6361/201525963)
- Thompson, S. E., Coughlin, J. L., Hoffman, K., et al. 2018, *ApJS*, 235, 38, doi: [10.3847/1538-4365/aab4f9](https://doi.org/10.3847/1538-4365/aab4f9)
- Thygesen, E., Ranshaw, J. A., Rodriguez, J. E., et al. 2023, *AJ*, 165, 155, doi: [10.3847/1538-3881/acaf03](https://doi.org/10.3847/1538-3881/acaf03)
- Torres, G., Winn, J. N., & Holman, M. J. 2008, *ApJ*, 677, 1324, doi: [10.1086/529429](https://doi.org/10.1086/529429)
- Tran, Q. H., Bowler, B. P., Endl, M., et al. 2022, *AJ*, 163, 225, doi: [10.3847/1538-3881/ac5c4f](https://doi.org/10.3847/1538-3881/ac5c4f)
- Triaud, A. H. M. J., Queloz, D., Hellier, C., et al. 2011, *A&A*, 531, A24, doi: [10.1051/0004-6361/201016367](https://doi.org/10.1051/0004-6361/201016367)
- Triaud, A. H. M. J., Neveu-VanMalle, M., Lendl, M., et al. 2017, *MNRAS*, 467, 1714, doi: [10.1093/mnras/stx154](https://doi.org/10.1093/mnras/stx154)
- Turner, O. D., Anderson, D. R., Collier Cameron, A., et al. 2016, *PASP*, 128, 064401, doi: [10.1088/1538-3873/128/964/064401](https://doi.org/10.1088/1538-3873/128/964/064401)
- Turrini, D., Schisano, E., Fonte, S., et al. 2021, *ApJ*, 909, 40, doi: [10.3847/1538-4357/abd6e5](https://doi.org/10.3847/1538-4357/abd6e5)
- Turtelboom, E. V., Weiss, L. M., Dressing, C. D., et al. 2022, *AJ*, 163, 293, doi: [10.3847/1538-3881/ac69e5](https://doi.org/10.3847/1538-3881/ac69e5)
- Udry, S., Mayor, M., Benz, W., et al. 2006, *A&A*, 447, 361, doi: [10.1051/0004-6361:20054084](https://doi.org/10.1051/0004-6361:20054084)
- Ulmer-Moll, S., Lendl, M., Gill, S., et al. 2022, *A&A*, 666, A46, doi: [10.1051/0004-6361/202243583](https://doi.org/10.1051/0004-6361/202243583)
- Ulmer-Moll, S., Osborn, H. P., Tuson, A., et al. 2023, *A&A*, 674, A43, doi: [10.1051/0004-6361/202245478](https://doi.org/10.1051/0004-6361/202245478)
- Vanderburg, A., Latham, D. W., Buchhave, L. A., et al. 2016, *ApJS*, 222, 14, doi: [10.3847/0067-0049/222/1/14](https://doi.org/10.3847/0067-0049/222/1/14)
- Vanderburg, A., Huang, C. X., Rodriguez, J. E., et al. 2019, *ApJL*, 881, L19, doi: [10.3847/2041-8213/ab322d](https://doi.org/10.3847/2041-8213/ab322d)
- Vivien, H. G., Hoyer, S., Deleuil, M., et al. 2024, *A&A*, 688, A192, doi: [10.1051/0004-6361/202348013](https://doi.org/10.1051/0004-6361/202348013)
- Šubjak, J., Gandolfi, D., Goffo, E., et al. 2025, *A&A*, 693, A235, doi: [10.1051/0004-6361/202451057](https://doi.org/10.1051/0004-6361/202451057)
- Wallace, L., Hinkle, K. H., Livingston, W. C., & Davis, S. P. 2011, *ApJS*, 195, 6, doi: [10.1088/0067-0049/195/1/6](https://doi.org/10.1088/0067-0049/195/1/6)
- Wanderley, F., Cunha, K., Souto, D., Smith, V. V., & Daflon, S. 2025, *AJ*, 170, 177, doi: [10.3847/1538-3881/ade112](https://doi.org/10.3847/1538-3881/ade112)
- Wang, J., & Fischer, D. A. 2015, *AJ*, 149, 14, doi: [10.1088/0004-6256/149/1/14](https://doi.org/10.1088/0004-6256/149/1/14)
- Weiner Mansfield, M., Line, M. R., Wardenier, J. P., et al. 2024, *AJ*, 168, 14, doi: [10.3847/1538-3881/ad4a5f](https://doi.org/10.3847/1538-3881/ad4a5f)
- Weiss, L. M., Marcy, G. W., Petigura, E. A., et al. 2018, *AJ*, 155, 48, doi: [10.3847/1538-3881/aa9ff6](https://doi.org/10.3847/1538-3881/aa9ff6)
- Wenger, M., Ochsenbein, F., Egret, D., et al. 2000, *A&AS*, 143, 9, doi: [10.1051/aas:2000332](https://doi.org/10.1051/aas:2000332)
- Wilson, R. F., Teske, J., Majewski, S. R., et al. 2018, *AJ*, 155, 68, doi: [10.3847/1538-3881/aa9f27](https://doi.org/10.3847/1538-3881/aa9f27)
- Wilson, R. F., Cañas, C. I., Majewski, S. R., et al. 2022, *AJ*, 163, 128, doi: [10.3847/1538-3881/ac3a06](https://doi.org/10.3847/1538-3881/ac3a06)
- Woolley, S. E., & Weaver, T. A. 1995, *ApJS*, 101, 181, doi: [10.1086/192237](https://doi.org/10.1086/192237)
- Wright, J., Rice, M., Wang, X.-Y., Hixenbaugh, K., & Wang, S. 2023, *AJ*, 166, 217, doi: [10.3847/1538-3881/ad0131](https://doi.org/10.3847/1538-3881/ad0131)
- Wright, J. T., Upadhyay, S., Marcy, G. W., et al. 2009, *ApJ*, 693, 1084, doi: [10.1088/0004-637X/693/2/1084](https://doi.org/10.1088/0004-637X/693/2/1084)
- Xue, Q., Bean, J. L., Zhang, M., et al. 2024, *ApJL*, 963, L5, doi: [10.3847/2041-8213/ad2682](https://doi.org/10.3847/2041-8213/ad2682)
- Yang, J., Hyder, A., Hu, R., & Lunine, J. I. 2026, *PSJ*, 7, 2, doi: [10.3847/PSJ/ae28d5](https://doi.org/10.3847/PSJ/ae28d5)
- Ye, X., Wu, W., Allende Prieto, C., et al. 2025, *A&A*, 695, A75, doi: [10.1051/0004-6361/202452871](https://doi.org/10.1051/0004-6361/202452871)
- Yee, S. W., Winn, J. N., Hartman, J. D., et al. 2022, *AJ*, 164, 70, doi: [10.3847/1538-3881/ac73ff](https://doi.org/10.3847/1538-3881/ac73ff)
- Yee, S. W., Stefánsson, G., Thorngren, D., et al. 2025, *AJ*, 169, 225, doi: [10.3847/1538-3881/adba5f](https://doi.org/10.3847/1538-3881/adba5f)
- Yu, L., Crossfield, I. J. M., Schlieder, J. E., et al. 2018, *AJ*, 156, 22, doi: [10.3847/1538-3881/aac6e6](https://doi.org/10.3847/1538-3881/aac6e6)
- Zhang, J., Huber, D., Weiss, L. M., et al. 2024, *AJ*, 168, 295, doi: [10.3847/1538-3881/ad86c4](https://doi.org/10.3847/1538-3881/ad86c4)